Matrix elements for the $\overline{\mathrm{B}} \to \mathrm{X_s}\gamma$ decay at NNLO

Dissertation zur Erlangung des
naturwissenschaftlichen Doktorgrades
der Julius-Maximilians-Universität Würzburg

vorgelegt von
Thomas Paul Schutzmeier

Würzburg, 2009

Eingereicht am 17.12.2009
bei der Fakultät für Physik und Astronomie

1. Gutachter: _____

2. Gutachter: _____

3. Gutachter: _____
der Dissertation

1. Prüfer: _____

2. Prüfer: _____

3. Prüfer: _____
im Promotionskolloquium

Tag des Promotionskolloquiums: _____

Abstract

In the context of the indirect search for non-standard physics in the flavour sector of the Standard Model (SM), one of the most interesting processes is the rare inclusive $\overline{B} \to X_s\gamma$ decay. On the one hand, being a flavour-changing neutral current, this B decay is sensitive to new physics, as it is loop-suppressed in the SM. On the other hand, it is only mildly affected by non-perturbative effects, and thus allows for precise theoretical predictions in the framework of renormalization-group improved perturbation theory. Accurate measurements as well as precise theoretical predictions with a good control over both perturbative and non-perturbative contributions have to be provided in order to derive stringent constraints on the parameter space of physics beyond the SM.

On the experimental side, an outstanding accuracy in the measurement of the $\overline{B} \to X_s\gamma$ decay rate has been achieved, which is mainly due the specialized experiments BaBar and Belle at the so-called B factories. To match the small experimental uncertainty, higher order computations within an effective low-energy theory of the SM are mandatory. In fact, next-to-next-to-leading order (NNLO) QCD corrections are required to provide a prediction for the decay rate with the same precision as the measurement.

The NNLO evaluation of the $\overline{B} \to X_s\gamma$ decay rate has been pursued by various groups over the last decade. The project was completed to a large extent and a first estimate at this level of perturbation theory was obtained in 2006. This prediction, however, lacks important contributions from yet unknown matrix elements, that were estimated from results which are only partially known to date. In this work, we provide a framework for the systematic study of the missing matrix elements at the NNLO. As main results of this thesis, we determine fermionic corrections to the charm quark mass dependent matrix elements of four-quark operators in the effective theory at NNLO. For the first time, the full mass dependence was kept. Moreover, we evaluate both bosonic and fermionic corrections to the decay rate in the limit of vanishing charm quark mass. These findings, combined with yet unknown remaining real contributions, will help to reduce the uncertainty of the NNLO branching ratio estimate considerably. Another central topic of the present work is the development of an automatic high-precision computation of multi-loop multi-scale integrals, a crucial ingredient for the here presented results.

Zusammenfassung

Einer der interssantesten Prozesse im Flavour Sektor des Standard Modells (SM) im Kontext der indirekten Suche nach neuer Physik ist der seltene inklusive Zerfall $\overline{B} \to X_s\gamma$. Dieser Zerfallskanal entspricht einem neutralen Strom mit Wechsel des Flavours zwischen Anfangs- und Endzustand. Im SM ist ein solcher Übergang unterdrückt, da er nur über Schleifenbeiträge erfolgen kann, und ist somit sensitiv auf Beiträge neuer Physik. Darüber hinaus sind nichtperturbative Beiträge moderat, was präzise theoretische Vorhersagen im Rahmen einer effektiven Niederenergie Theorie ermöglicht. Sowohl präzise Messungen als auch genaue theoretische Vorhersagen mit einer guten Kontrolle über perturbative und nichtperturbative Effekte sind notwendig, um den Parameterraum von Modellen jenseits des SM einzuschränken.
Experimentell wurde die Zerfallsrate $\overline{B} \to X_s\gamma$ vor Allem mit Hilfe der spezialisierten Experimente BaBar und Belle an den sogenannten B Fabriken mit einer hervorragenden Genauigkeit gemessen. Um diese Präzision auch in der theoretische Vorhersage zu erhalten, sind höhere Ordnungen in der effektiven Störungstheorie essentiell. Tatsächlich führt erst die Berücksichtigung von QCD Korrekturen auf der nächst-zu-nächst-zu höheren Ordnung (NNLO) in Störungstheorie zu einer mit dem Experiment vergleichbaren theoretischen Unsicherheit.
Die Bestimmung des Verzweigungsverhältnisses von $\overline{B} \to X_s\gamma$ auf NNLO wurde innerhalb der letzten zehn Jahre von mehreren Arbeitsgruppen angegangen. Ein Großteil dieses Projekts wurde abgeschlossen und eine erste Abschätzung auf diesem Niveau der Störungstheorie 2006 publiziert. Allerdings standen für diese Vorhersage nicht alle Beiträge von nach wie vor unbekannten Matrixelementen zur Verfügung, die nur aus partiell bekannten Resultaten abgeschätzt werden mussten. In dieser Arbeit bereiten wir einen Rahmen für die systematische Bestimmung der noch nicht verfügbaren Matrixelemente auf NNLO. Ein Hauptergebnis dieser Dissertation ist die Bestimmung von fermionischen Korrekturen zu Matrixelementen von Vier-Quark Operatoren in der effektiven Theorie. Erstmalig wird hierbei die volle Massenabhängigkeit berücksichtigt. Ein weiterer Schwerpunkt liegt auf der Berechnung von fermionischen als auch bosonischen Korrekturen im Grenzwert einer verschwindenden Masse des Charm Quarks. Zusammen mit noch unbekannten reellen Korrekturen werden diese Ergebnisse dazu beitragen, die Unsicherheit der NNLO Vorhersage signifikant zu reduzieren. Ein wesentlicher Bestandteil dieser Arbeit, der die hier durchgeführten Berechnungen erst ermöglichte, ist die Entwicklung einer automatisierten Methode zur hochpräzisen Bestimmung von Vielschleifenintegralen die zwei Massenskalen enthalten.

Contents

1. Introduction

One of the greatest success stories of the last decades in the field of high energy physics was undeniably the establishment of the Standard Model (SM) of interactions between elementary particles. Based on the combination of the theory of unified electromagnetic and weak interactions proposed by Glashow, Salam and Weinberg [1, 2] and Quantum Chromodynamics (QCD) [3, 4, 5, 6], the model of strong interactions, it has proven able to explain phenomena at the smallest scale with astounding accuracy and predictive power. A central ingredient of the SM is the mechanism of electroweak symmetry breaking (EWSB)[7, 8, 9, 10, 11], giving masses to the weak bosons in a minimal way and introducing a scalar particle – the Higgs field. With the discovery of asymptotic freedom [5] shortly after the first formulation of the electroweak model it became apparent that this theory is indeed perturbative at higher energies and also meets the requirement of renormalizability [12, 13]. It was not until the first measurement of the weak current [14, 15, 16] and after the discovery of the $W^{\pm}$ and Z bosons [17, 18, 19, 20], however, that the interest in this model rose and it found general acceptance.

In the following years, the framework of the SM provided a clear picture of the nature of elementary particles and passed an impressive number of experimental tests with increasing precision. In the LEP experiment [21], the electroweak sector was extensively studied, reaching an accuracy at the percent and even the permille level. It is remarkable that predictions in the framework of the SM turned out to be compatible with almost all of these observables within the measured uncertainty bounds [21, 22], thereby probing quantum corrections to the theory. That is, radiative corrections became mandatory to match the high precision measurements. Examples are higher order electroweak and QCD corrections [23, 24, 25, 26, 27] to the ρ parameter, the effective electroweak leptonic mixing angle [28] or the muon decay [29]. Moreover, after the discovery of the until then missing top quark at the Tevatron [30, 31], the predicted fermionic particle content of the SM has been completed. Only the Higgs particle has not been seen directly, although LEP and Tevatron as well as other experiments provide indirect insights into the scalar sector - a fact that has driven the development and launch of the Large Hadron Collider (LHC).

Despite its success, the SM model has to be considered only an effective theory, which however describes the nature of strong and electroweak interactions at low energies, i.e. below the EWSB scale, very well. This fact is indicated by both theoretical and experimental observations. The most obvious open theoretical questions concern the pattern of the quark mass spectrum and the origin of the neutrino masses, not to speak of the lack of gravitational interactions. Moreover, higher order corrections in the Higgs sector lead to the naturalness problem [32, 33], which requires a fine tuning of scales to

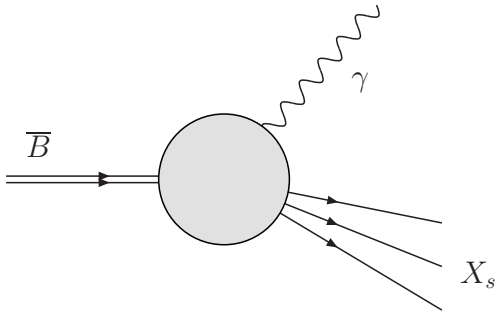

allow for a Higgs mass in the expected EWSB range of ~ 250 GeV. From the experimental point of view, both the observed rotation curves of galaxies [34] and the cosmic microwave background, determined by WMAP [35], point to the existence of non-baryonic neutral matter. The SM does not provide a candidate for this so-called Dark Matter (DM). As a consequence, above the EWSB scale a yet unknown new physics (NP) model is expected to become apparent, which is required to contain the SM in the low energy limit.

So far, no direct evidence for physical effects beyond the SM has been found in collider experiments, which can either be due to the masses of new particles lying above the yet accessible energy range or to their small coupling to the SM fields. Meanwhile, experiments below the EWSB scale became more and more accurate. On the theory side, this precision has to be matched by higher order computations, which in turn open the window for indirect searches of non-standard effects. New particles can virtually contribute in higher orders of perturbation theory, thereby influencing the theoretical prediction. Even if no deviation from the SM is observed in experiment, high accuracy both in measurements and theoretical computations can lead to stringent bounds on masses or parameters of various NP models. An important and strongly investigated ingredient of the SM in this respect is the flavor sector. In the following we will focus on this sector and, more specifically, on the central topic of this work: the radiative hadronic B meson decay $\overline{B} \to X_s\gamma$.

The crucial phenomenon in the flavour sector is the quark mixing which is mediated by the weak interaction and described by the Cabbibo-Kobayashi-Maskawa (CKM) matrix. The elements of this matrix can be thoroughly and completely studied in decays of heavy B mesons, which motivated the construction of B factories at SLAC (BaBar) [36] and KEK (Belle) [37] . In these $e^+\,e^-$ collider experiments, which provide a clean environment due to purely leptonic initial states, $B\overline{B}$ pairs are produced via the $\Upsilon(4S)$ resonance and their decays are studied. Complementary to these measurements is the B program at Tevatron, which operates with a larger hadronic background, but allows for investigations of the whole spectrum of B mesons. An interesting discovery in this respect was the finding of CP violation in B meson decays which can be accounted for in the SM through complex phases in the CKM matrix [38]. On the theory side, these effects require predictions of exclusive quantities, like the predicition of the golden decays

$B \to J/\psi\, K_s$ or $B \to \phi\, K_s$, which are inherently nonperturbative quantities. Although QCD factorization provides a consistent framework here, the resulting uncertainties are rather large. Alltogether, the large amount of data collected for these decay modes allows for a precise determination of quantities in the flavour sector, like CKM matrix elements, heavy quark masses or B meson shape functions. Moreover, only a fraction of the measured observables is needed to fit the input parameters and the flavor sector can be tested with high accuracy.

The most interesting and perturbatively well described observables in B decays are inclusive decay rates or branching ratios. The small experimental uncertainties often require - similar to the aforementioned studies at LEP - higher order computations and careful analysis of nonperturbative effects. An interesting example is the hadronic radiative decay mode $\overline{B} \to X_s\gamma$. Since the first measurement of the $\overline{B} \to K^*\gamma$ decay in 1993 by CLEO [39], which gave an upper bound on the branching ratio of $\overline{B} \to X_s\gamma$, a lot of effort has been put into the precise measurement of the inclusive branching ratio as well as the photon spectrum. The current experimental value for the branching ratio reads [40]

$$\mathcal{B}(\overline{B} \to X_s\gamma)_{E_\gamma \geq 1.6\,\mathrm{GeV}} = (3.52 \pm 0.23 \pm 0.09) \times 10^{-4} \tag{1.1}$$

where the first error includes systematics and statistics and the second is due to the extrapolation of the imposed cut on the photon energy. This result was obtained by the Heavy Flavor Averaging Group [40] and is a combined value from different experiments: CLEO [41], BELLE [42] and BaBar [43, 44, 45]. Although the $\overline{B} \to X_s\gamma$ transition is a rare decay with a branching ratio of only a few tenth of a permille, the experimental uncertainty is at the level of 7%. Future so-called Super$B$ factories are expected to reduce this error even further down to 5% [46].

This excellent achieved accuracy allows for different applications within the SM and beyond. The spectral shape of the $\overline{B} \to X_s\gamma$ decay is, for instance, sensitive to the structure of the $\overline{B}$ meson. Hence, the parameters in the Heavy Quark Effective Theory (HQET) describing the hadronic nature can be fitted. In [47], these findings were used to obtain the CKM matrix element V_{ub} from inclusive $b \to u l^- \nu$ decays. Moreover, comparing the measured branching ratio with SM predictions constitutes a stringent test of the flavor sector and indirectly constraints non-standard effects. Another example is the determination of the bottom quark mass to high orders in perturbation theory including subleading terms of the HQET expansion [48].

In the SM, the weak decay $\overline{B} \to X_s\gamma$ is an outstanding example of a flavour changing neutral current (FCNC) process. This kind of processes are naturally suppressed at tree level by the Glashow-Iliopoulos-Maliani mechanism, which enforces the neutral interactions via photons, gluons and Z^0 bosons to be flavour diagonal. In higher orders of perturbation theory, however, FCNCs are allowed to occur via $W^\pm$ exchange in loop diagrams, cf. fig. 1.1. This makes that process an excellent candidate for the indirect search of new physics effects, as they appear at the same or lower level of perturbation theory and are not suppressed by additional factors of the electroweak coupling. One of the first NP studies in the context of the $\overline{B} \to X_s\gamma$ decay was carried out in the

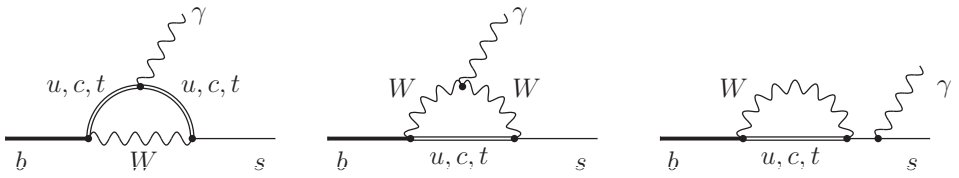

Figure 1.1.: Flavour changing neutral current in the Standard Model.

so-called Type II Two Higgs Doublet Model (THDMII) and extended up to the NLO [49, 50, 51, 52]. There, a charged scalar field, which acquires a vacuum expectation value upon electroweak symmetry breaking, is added to the SM Higgs sector. This theory is particularly interesting, since masses of up- and down-type quarks are generated by Yukawa couplings to the different Higgs fields. Therefore, this theory mimics the Higgs sector of the Minimal Supersymmetric Standard Model (MSSM) and all conclusions drawn from this theory directly apply to the charged Higgs in the MSSM. In addition to the SM contributions, the $\overline{B} \to X_s\gamma$ decay there is mediated by an amplitude containing the virtual charged Higgs as shown in fig. 1.2. The latest comparison of the branching

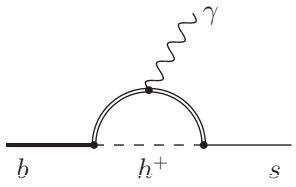

Figure 1.2.: Possible contribution involving a charged Higgs boson.

ratio obtained in this model and its experimental value provides a lower bound on the mass of the charged Higgs in the range of small $\tan\beta$, which is the ratio of the two vacuum expectation values. The exclusion plot is shown in fig. 1.3.
In different other models, like universal extra dimensions, little Higgs or various SUSY scenarios (see [53] and references therein), the $\overline{B} \to X_s\gamma$ decay provides an invaluable input to constrain the parameter space, already at tree level.

To draw level with the small experimental uncertainty and to be able to resolve possible deviations from the SM, however, an elaborate analysis of the $\overline{B} \to X_s\gamma$ branching ratio at higher orders is unavoidable, as will be shown in this work. In fact, next-to-next-to-leading (NNLO) order QCD corrections are required, which, in view of the loop suppression of the decay, amount to difficult three- and even four-loop calculations. Several developments within the last ten to fifteen years, together with the previous establishment of dimensional regularization [54] for a straightforward treatment of UV divergences and the study of general properties of Feynman integrals, made computations of such complexity feasible. One of the milestones was the algorithmic formulation [55] of the so called integration-by-parts reduction [56] of the large number of multi-loop

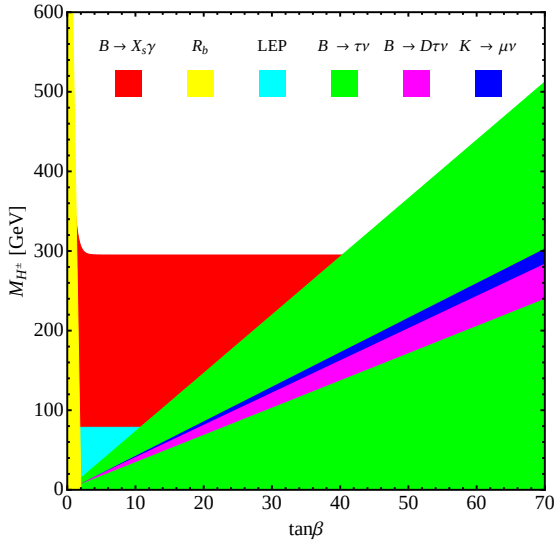

Figure 1.3.: Exclusion plot for the charged Higgs mass in the THDMII against $\tan\beta$, the ratio of vacuum expectation values. The shaded areas depict excluded regions.

integrals encountered in these evaluations to smaller sets. Various techniques for the actual computation of multi-loop integrals, ranging from the Gegenbauer method [57], Mellin-Barnes representations [58, 59], the Sector Decomposition [60], diagrammatic asymptotic expansions [61, 62] to the application of differential equations in kinematic invariants [63, 64], were developed and successfully applied. In the case of perturbative computations for matrix elements of the $\overline{B} \to X_s\gamma$ decay it turns out, however, that one encounters a large number of integrals even after a full reduction, which demands a new automatic approach.

In this thesis, the main focus is on the theoretical prediction of the branching ratio of the $\overline{B} \to X_s\gamma$ decay at the NNLO in the strong coupling. The major issue here are matrix elements of certain operators contributing to the branching ratio, which are not yet fully available at this level of accuracy. Involved three- and four-loop computations are required to fill this gap. We evaluate relevant contributions to these matrix elements, which constitute a cornerstone to finalize the NNLO program for the $\overline{B} \to X_s\gamma$ decay.
One of the main findings of this work are NNLO virtual fermionic corrections to matrix elements of charm quark mass dependent four-quark operators. In this context, we provide a confirmation of previously available results that are crucial in the evaluation of the SM branching ratio. Moreover, we investigate finite mass effects of charm and bottom quarks in virtual contributions, which where neglected so far.
Another important project studied in the course of this work is also related to matrix elements of the four quark operators, where we focus on both fermionic and bosonic NNLO corrections treating the charm quark as massless. We evaluate both purely virtual and involved parts of real radiation corrections to an important matrix element

interference relevant for the $\overline{B} \to X_s\gamma$ decay rate. The results presented here constitute a major contribution and we provide a framework for the yet required pieces. Once our approach is applied to obtain the full real radiation contribution, the remaining perturbative uncertainty of the branching ratio at NNLO can largely be reduced.
A crucial aspect of the successful computations performed in this thesis is the development of a systematic computational approach extending some of the above mentioned techniques. The complexity and number of the required multi-loop integrals demands a mostly automatized technique that provides high-precision numerical results, a goal that was achieved and is thoroughly discussed in the present text.
Finally, we present the evaluation of double-fermionic QCD corrections to the photon propagator at $\mathcal{O}(\alpha\alpha_s^3)$ in the appendix. This contribution is another excellent example of the application of the techniques which were developed in this thesis and provided a test bed for the new methods.

Chapter 2 of this thesis is devoted to the theory of radiative hadronic B decays. Firstly, the effective theory framework required for weak boson induced decays at small energy transfers is discussed in the context of radiative corrections and the main contributions up to the NNLO are presented. Secondly, theoretical predictions of the $\overline{B} \to X_s\gamma$ branching ratio within the SM and their uncertainties are reviewed. The status of the evaluation of matrix elements in the effective theory and, most importantly, the missing pieces are collected in the following. We close this chapter with details on the relation of the theoretically obtained branching ratio with the exclusive experimental observable and estimate of nonperturbative effects.
In chapter 3 we present new results for matrix elements of the important four-quark operators computed in the course of this work. Full fermionic corrections at NNLO, and especially mass effects in these quantities, are presented in section 3.1. In the subsequent section we focus on the reduction of the perturbative uncertainty by providing a major part of four-quark matrix elements in the limit of vanishing charm quark mass.
Technical details about the used, developed and implemented methods are given in chapters 4 and 5. There, also a complicated four-loop scalar integral, is discussed as an example.
Part A of the appendix is devoted to higher order corrections to the photon propagator, their physical relevance and need and the computation of the full double fermionic contribution at the four-loop level. In appendix B we give explicit expressions for all multi-loop integrals needed for the computations performed in this work.

Part I.

The $\overline{B} \to X_s\gamma$ decay at NNLO

2. Theory of radiative hadronic B decays

As will be explained in more detail later, the decay width $\Gamma(\overline{B} \to X_s\gamma)$ is well approximated by the partonic decay rate $\Gamma(b \to s\gamma)$ which can be thoroughly analyzed in the framework of the SM. Unfortunately, due to the hierarchy of the involved scales, QCD corrections introduce logarithms of the form $\alpha_s(m_b)^n \log^m(m_b/M)$ where $M = m_W$ or $M = m_t$. Although the strong coupling at the bottom scale is relatively small, $\alpha_s(m_b) \approx 0.4$, the logarithmic enhancement is around 140%, rendering the perturbation series invalid. To overcome this issue a successful approach is given within the context of operator product expansions yielding effective field theories where in addition renormalization group improvements are taken into account.

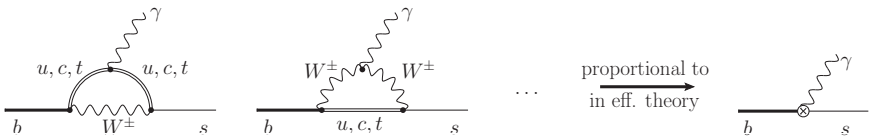

Figure 2.1.: In the effective theory, the sum of diagrams mediating the $\overline{B} \to X_s\gamma$ decay is expressed through only one effective matrix element.

The key idea is that a decaying hadron of mass $\mathcal{O}(m_b)$ is insensitive to physics at some higher scale $m_W \gg m_b$ and can be appropriately described by point-like interactions represented by local effective operators P_i. The general form of the corresponding interaction Lagrangian $\mathcal{L}_{eff}$ reads

$$\mathcal{L}_{eff} = \frac{G_F}{\sqrt{2}} \sum_i V_{kl} V_{nm}^* C_i(\mu) P_i(\mu) \tag{2.1}$$

with the Fermi constant G_F and corresponding CKM matrix elements $V_{ij}^{(*)}$.
The Wilson coefficients $C_i(\mu)$ can be understood as effective couplings. The main point of this procedure is to separate short distance effects into the coefficients $C_i(\mu)$ and long distant effects into the expectation values $\langle P_i \rangle$. Large logarithms then occur only in the Wilson coefficients that are obtained from a comparison of SM and effective theory Green's functions at the scale $\mu = m_W$. Using renormalization group techniques to evolve the effective couplings to the relevant momentum transfer scale $\mu = m_b$ for the B decay, these large logarithms are resummed. Defining (almost) inclusive observables at the bottom scale also, the matrix elements can be computed in perturbation theory up to terms of order $\mathcal{O}(\Lambda^2/m_b^2)$, Λ being the hadronization scale. The $b \to s\gamma$ decay

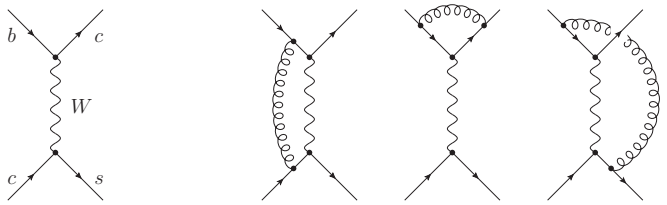

Figure 2.2.: Tree level (a) of and leading QCD corrections (b) to the amplitude $b \to \overline{c}cs$.

at leading order mediated by several diagrams in the SM is proportional to the matrix element of only one operator (cf. fig. 2.1).
QCD corrections induce, however, a richer structure of local operators due to the interplay between electroweak and strong interactions. This fact can easily be visualized in a simple example by comparing the amplitude $b \to c\overline{c}s$ in the limit of large W boson mass at tree and one-loop level. Expanding the leading order diagram of fig. 2.2 (a) in the inverse of the weak boson mass up to leading order, on obtains in a straightforward way

$$\begin{aligned} A^{(0)} \quad &= \quad -\frac{G_F}{\sqrt{2}} V_{bc}^* V_{cs} \frac{m_W^2}{k^2 - m_W^2} (\overline{s}_L^\beta \gamma_\mu c_L^\beta)(\overline{c}_L^\alpha \gamma^\mu b_L^\alpha) \\ &\overset{m_W^2 \gg k^2}{\longrightarrow} \quad -\frac{G_F}{\sqrt{2}} V_{bc}^* V_{cs} (\overline{s}_L^\beta \gamma_\mu c_L^\beta)(\overline{c}_L^\alpha \gamma^\mu b_L^\alpha) + \mathcal{O}\left(\frac{k^2}{m_W^2}\right) \end{aligned} \tag{2.2}$$

where k^μ is the momentum exchange between the two vertices, the index L indicates that only left-handed quarks participate in the decay and α and β are color indices. Eqn. (2.2) can now be understood as the transition amplitude, mediated by a single effective operator

$$P = (\overline{s}_L^\beta \gamma_\mu c_L^\beta)(\overline{c}_L^\alpha \gamma^\mu b_L^\alpha). \tag{2.3}$$

Since the weak interaction is color blind, no color exchange in the effective vertex takes place. This situation changes considerably, once QCD corrections at the one-loop level are turned on. The contributing diagrams are depicted in fig. 2.2 (b) and the amplitude after performing the loop integrals in $d = 4 - 2\epsilon$ dimensions and expanding in the limit of large m_W reads

$$\begin{aligned} A^{(1)} \quad = \quad & -\frac{G_F}{\sqrt{2}} V_{bc}^* V_{cs} \left\{ -\frac{3\alpha_s}{4\pi} \log\left(\frac{m_W^2}{-k^2}\right) P \right. \\ & \left. + \left[1 + \frac{\alpha_s}{4\pi} \left(\frac{2C_F}{\epsilon} + 2C_F \log\left(\frac{\mu^2}{-k^2}\right) + \log\left(\frac{m_W^2}{-k^2}\right) \right) \right] \tilde{P} \right\}. \end{aligned} \tag{2.4}$$

It is sufficient to leave the amplitude unrenormalized here, where μ is the scale dependence introduced through $\alpha_s \to \mu^{2\epsilon} \alpha_s$ and $C_F = 4/3$ is a $\mathrm{SU}(3)_{color}$ invariant. It is apparent that a new effective operator different from eqn. (2.3), given by

$$\tilde{P} = (\overline{s}_L^\beta \gamma_\mu c_L^\alpha)(\overline{c}_L^\alpha \gamma^\mu b_L^\beta), \tag{2.5}$$

contributes to the one-loop amplitude $A^{(1)}$. Its origin lies in the algebra of color generators T^a, which are introduced by the gluon exchange. They satisfy

$$T^a_{\alpha\beta}T^a_{\gamma\delta} = -\frac{1}{6}\delta_{\alpha\beta}\delta_{\gamma\delta} + \frac{1}{2}\delta_{\alpha\delta}\delta_{\beta\gamma} \tag{2.6}$$

in $\mathrm{SU}(3)_{color}$. Computing the same amplitude in the toy effective theory built from the operators P and $\tilde{P}$ and the effective couplings C_P and $C_{\tilde{P}}$ and performing operator renormalization to remove the UV divergences (e.g. in the $\overline{\mathrm{MS}}$ scheme), one obtains the Wilson coefficients $C_P(m_W)$ and $C_{\tilde{P}}(m_w)$. Note that all logarithms of the form $\log(m_W^2/\mu^2)$ are, after correct rearrangement, absorbed in the Wilson coefficients.

Since the first approach to the weak effective theory in [65, 66], the underlying theoretical framework in the presence of QCD corrections has been studied extensively in a systematic way over the last years leading to a complete picture of its structures. In the following, the renormalization group improved weak effective theory approach and the basic steps for computations within this framework are discussed.

2.1. Effective theory framework for the $\overline{B} \to X_s\gamma$ decay

2.1.1. Effective Lagrangian

The relevant effective Lagrangian for weak hadronic decays is given by

$$L_{eff} = L_{QED\times QCD} + \frac{4G_F}{\sqrt{2}}V_{ts}^*V_{tb}\sum_{i=1}^{8} C_i(\mu)\, P_i(\mu). \tag{2.7}$$

Here the first term is the usual QCD-QED Lagrangian for the light SM quarks. In the second term, V_{ij} denotes the elements of the Cabibbo-Kobayashi-Maskawa matrix, G_F is the Fermi coupling constant and $C_i(\mu)$ are the Wilson coefficients of the corresponding operators P_i evaluated at the scale μ. The Lagrangian is obtained by integrating out the W boson and top quark fields at the same scale $\mathcal{O}(m_W)$. Moreover, we neglect terms proportional to $V_{us}^*V_{ub}$ since $|V_{us}^*V_{ub}/V_{ts}^*V_{tb}| \approx 10^{-6}$ [67].

Relevant for the $\overline{B} \to X_s\gamma$ decay is the extended basis of effective operators, which consists of dimension-five quark-photon and quark-gluon interactions (commonly known as dipole and chromomagnetic operators, respectively) and several dimension-six four-quark operators. These dimension-six operators basically differ in color and field structure due to hard gluon exchange, as was shown in the introduction to this chapter.

Adopting the operator definitions of [68], the relevant physical operators read

$$\begin{aligned}
P_1 &= (\bar{s}_L\gamma_\mu T^a c_L)(\bar{c}_L\gamma^\mu T^a b_L),\\
P_2 &= (\bar{s}_L\gamma_\mu c_L)(\bar{c}_L\gamma^\mu b_L),\\
P_3 &= (\bar{s}_L\gamma_\mu b_L)\sum\nolimits_q(\bar{q}\gamma^\mu q),\\
P_4 &= (\bar{s}_L\gamma_\mu T^a b_L)\sum\nolimits_q(\bar{q}\gamma^\mu T^a q),\\
P_5 &= (\bar{s}_L\gamma_\mu\gamma_\nu\gamma_\rho b_L)\sum\nolimits_q(\bar{q}\gamma^\mu\gamma^\nu\gamma^\rho q),\\
P_6 &= (\bar{s}_L\gamma_\mu\gamma_\nu\gamma_\rho T^a b_L)\sum\nolimits_q(\bar{q}\gamma^\mu\gamma^\nu\gamma^\rho T^a q),\\
P_7 &= \frac{e}{16\pi^2}\,\overline{m}_b(\mu)\,(\bar{s}_L\sigma^{\mu\nu}b_R)\,F_{\mu\nu},\\
P_8 &= \frac{g_s}{16\pi^2}\,\overline{m}_b(\mu)\,(\bar{s}_L\sigma^{\mu\nu}T^a b_R)\,G^a_{\mu\nu}.
\end{aligned} \tag{2.8}$$

Here, the sum over q runs over all light quark fields, and e and g_s are the electromagnetic and strong coupling constants respectively. $L(R) = (1 \mp \gamma_5)/2$ is the left(right)-handed projection operator. $F_{\mu\nu}$ is the electromagnetic field strength tensor, and T^a ($a = 1,\ldots,8$) denote the $SU(3)$ color generators.
Upon QCD renormalization, the set of operators (2.8) closes on-shell, apart from non-physical so-called evanescent operators that vanish in four dimensions and are required in higher order computations. Furthermore, the choice of local four-quark operators in the basis (2.8) is made such that at leading order of G_F and at all orders in QCD, no Dirac traces involving γ_5 matrices occur. Hence, one can greatly simplify multi loop calculations by adopting a fully anticommuting γ_5 within dimensional regularization in $d = 4 - 2\epsilon$ dimensions, a regularization scheme that is commonly referred to as naive dimensional regularization (NDR) [69].

2.1.2. Renormalization

Every amplitude between an initial state ψ_i and a final state ψ_f mediated by some operator P_i in the effective theory, is of course required to be finite in every order of perturbation theory which is accomplished by appropriate renormalization. In this case, the bare amplitude is simply given by

$$A^B = C_i^B(\mu)\langle\psi_f|P_i(\mu)|\psi_i\rangle^B. \tag{2.9}$$

On the one hand, the effective operators receive the standard QED and QCD renormalization of wave functions, quark masses and coupling constants:

$$m^B\overline{\psi}\psi = Z_m m^R(\overline{\psi}\psi)^R, \quad \psi^B = \sqrt{Z_\psi}\psi^R, \quad G^{\mu,B} = \sqrt{Z_G}G^{\mu,R}, \quad g^B = Z_g g^R. \tag{2.10}$$

On the other hand, the bare effective couplings are renormalized according to

$$C_i^B(\mu) = Z_{ij}C_j^R(\mu) \tag{2.11}$$

where the renormalization constants are expanded in powers of the coupling α as

$$Z_{ij} = \delta_{ij} + \sum_n \alpha_s^n Z_{ij}^{(n)}. \tag{2.12}$$

In the mass independent $\overline{\text{MS}}$ scheme employed here, the right hand side is entirely expressed by poles in ϵ,

$$Z_{ij}^{(n)} = \sum_{k=1}^{n} \epsilon^{-k} Z_{ij}^{(n,k)}. \tag{2.13}$$

Any renormalized amplitude in the effective theory is therefore given by

$$A^R = Z_{ij} C_j(\mu) \langle \psi_f | P_i | \psi_i \rangle^R \tag{2.14}$$

where $\langle \psi_f | P_i | \psi_i \rangle^R$ represents the matrix element of the bare operator after performing the necessary mass, coupling and wave function renormalization. Requiring the cancellation of UV divergences within amplitudes, the renormalization matrix Z_{ij} can be determined. We refrain from quoting the lengthy counterterm part of the renormalized Lagrangian here and refer the reader to [68, 70, 71, 72, 73] for the renormalization matrix and to appendix B for the QCD renormalization constants up to NNLO in the strong coupling.

It is important to notice that although the operator basis (2.8) for the on-shell Lagrangian is complete for the evaluation of tree-level quantities encountered in hadronic B decays, an additional set of operators is needed to completely provide the renormalization. The existence of these so-called evanescent operators E_i was already realized at the dawn of dimensional regularization [54] and more systematically investigated in the context of B decays in [74]. Algebraically, evanescent operators vanish in $d = 4$ dimensions but have to be taken into account as soon as any of the $\{P_1, \ldots, P_8\}$ are either multiplied with divergent renormalization constants or inserted into sub-loops. In this case, apart from the on-shell operators of eqn. (2.8) the $\mathcal{O}(\epsilon)$ parts of the E_i contribute to both the computation of the anomalous dimension matrix and to finite terms in the renormalization of matrix elements.

In the NDR scheme and following the definitions of [70] the evanescent operators are given up to $\mathcal{O}(\alpha_s^2)$ by

$$\begin{aligned}
P_{25} &= (\overline{s}_L\gamma_\mu\gamma_\nu\gamma_\rho T^a c_L)(\overline{c}_L\gamma^\mu\gamma^\nu\gamma^\rho T^a b_L) - 16P_1 \\
P_{26} &= (\overline{s}_L\gamma_\mu\gamma_\nu\gamma_\rho c_L)(\overline{c}_L\gamma^\mu\gamma^\nu\gamma^\rho b_L) - 16P_2 \\
P_{27} &= (\overline{s}_L\gamma_\mu\gamma_\nu\gamma_\rho\gamma_\sigma\gamma_\tau b_L)\sum_q(\overline{q}\gamma^\mu\gamma^\nu\gamma^\rho\gamma^\sigma\gamma^\tau q) + 64P_3 - 20P_5 \\
P_{28} &= (\overline{s}_L\gamma_\mu\gamma_\nu\gamma_\rho\gamma_\sigma\gamma_\tau T^a b_L)\sum_q(\overline{q}\gamma^\mu\gamma^\nu\gamma^\rho\gamma^\sigma\gamma^\tau T^a q) + 64P_4 - 20P_6 \\
P_{29} &= (\overline{s}_L\gamma_\mu\gamma_\nu\gamma_\rho\gamma_\sigma\gamma_\tau T^a c_L)(\overline{c}_L\gamma^\mu\gamma^\nu\gamma^\rho\gamma^\sigma\gamma^\tau T^a b_L) - 256P_1 - 20P_{25} \\
P_{30} &= (\overline{s}_L\gamma_\mu\gamma_\nu\gamma_\rho\gamma_\sigma\gamma_\tau c_L)(\overline{c}_L\gamma^\mu\gamma^\nu\gamma^\rho\gamma^\sigma\gamma^\tau b_L) - 256P_2 - 20P_{26} \\
P_{31} &= (\overline{s}_L\gamma_\mu\gamma_\nu\gamma_\rho\gamma_\sigma\gamma_\tau\gamma_\omega\gamma_\eta c_L)(\overline{c}_L\gamma^\mu\gamma^\nu\gamma^\rho\gamma^\sigma\gamma^\tau\gamma^\omega\gamma^\eta b_L) + 1280P_3 - 336P_5 \\
P_{32} &= (\overline{s}_L\gamma_\mu\gamma_\nu\gamma_\rho\gamma_\sigma\gamma_\tau\gamma_\omega\gamma_\eta T^a c_L)(\overline{c}_L\gamma^\mu\gamma^\nu\gamma^\rho\gamma^\sigma\gamma^\tau\gamma^\omega\gamma^\eta T^a b_L) - 1280P_4 - 336P_6
\end{aligned} \tag{2.15}$$

where we adopt the naming convention of the full off-shell weak effective Lagrangian that includes also semi-leptonic decays. The choice of these operators is by no means unique. Indeed, on can add arbitrary physical operators to the evanescent operators as long as their contribution also vanishes in $d = 4$ dimensions.
Computations within the effective theory framework are performed in three subsequent steps: the so-called matching, the determination of the renormalization matrix and the renormalization group running of the effective couplings, and finally the computation of the matrix elements of interest. The former two are described in the following, while the latter is the central topic of this work and is discussed in more detail in chapter 2.2.2.

2.1.3. Matching

The first step in the effective theory computation consists of the determination of Wilson coefficients at the electroweak scale μ_W by the requirement of the equality of SM and EFT amplitudes, given by

$$\langle\psi_f|\mathcal{U}|\psi_i\rangle = \frac{4G_F}{\sqrt{2}}V_{ts}^*V_{tb}\langle\psi_f|\sum_{i=1}^{8}C_i(\mu_W)P_i(\mu_W)|\psi_i\rangle \tag{2.16}$$

where $\mathcal{U}$ is the transition operator in the full theory and $\psi_{i,f}$ are states containing photons, gluons and five generations of quarks. It is sufficient to compute off-shell amplitudes in both theories expanded in the external momenta and in the bottom quark mass, which simplifies the computation considerably. Quark mass renormalization can be neglected, since these contributions cancel. To retain gauge invariance in this case at the level of the Standard Model Green's functions, however, it is crucial to choose a background field version of the R_ξ gauge [75]. The relevant one-particle irreducible diagrams in the full theory are shown in fig. 2.3.
After expanding the full amplitude in terms of $1/m_W^2$ and therein identifying the tree level matrix elements $\langle P_i^{(0)}\rangle$ with operators as given in the basis (2.8), one obtains at a given order n of QCD

$$\langle\psi_f|\mathcal{L}_W|\psi_i\rangle = \vec{F}\langle\vec{P}^{(0)}(\mu)\rangle = \sum_{j=0}^{n}\left(\frac{\alpha_s}{4\pi}\right)^j\vec{f}^{(j)}\langle\vec{P}^{(0)}(\mu)\rangle \tag{2.17}$$

while on the effective theory side we define the matrix $\mathbf{S}$ such that

$$\langle\psi_f|\vec{P}(\mu_W)|\psi_i\rangle = \mathbf{S}\langle\psi_f|\vec{P}^{(0)}(\mu_W)|\psi_i\rangle = \sum_{j=0}^{n}\left(\frac{\alpha_s}{4\pi}\right)^j\mathbf{s}^{(j)}\langle\psi_f|\vec{P}^{(0)}(\mu_W)|\psi_i\rangle \tag{2.18}$$

With the perturbative series

$$\vec{C}(\mu) = \sum_{j=1}^{n}\left(\frac{\alpha_s}{4\pi}\right)^j C^{(j)}(\mu), \tag{2.19}$$

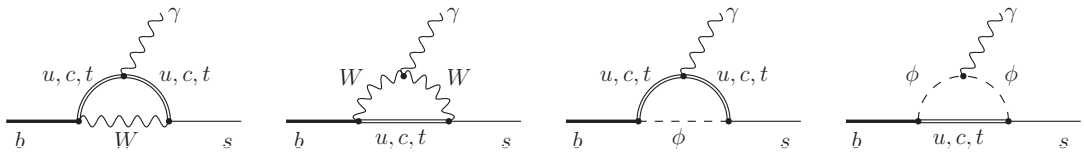

Figure 2.3.: 1PI diagrams in the SM at leading order.

we find a simple form for the matching conditions

$$\vec{F} = \mathbf{S}^T \vec{C}. \tag{2.20}$$

They can be solved order by order in α_s yielding Wilson coefficients $C_i(\mu_W)$ at the electroweak scale.
The SM values for the Wilson coefficients in the leading logarithmic approximation are given by [76, 77]

$$\begin{aligned} C_2^{(0)}(\mu_W) &= 1 \\ C_7^{(0)}(\mu_W) &= -\frac{x(8x^2+5x-7)}{24(x-1)^3} + \frac{3x-2}{4(x-1)^4}x^2\log x \\ C_8^{(0)}(\mu_W) &= -\frac{x(x^2-5x-2)}{8(x-1)^3} - \frac{3}{4(x-1)^4}x^2\log x \end{aligned} \tag{2.21}$$

where $x = \log(m_t^2/\mu_W^2)$ with the top quark mass m_t. All other effective couplings vanish at this level of accuracy.
At NLO of the strong coupling the matching of the dipole operators, which is the most difficult part was performed for the first time already more than a decade ago in [78] and verified in [79]. The NNLO QCD corrections to the matching require a two-loop computation for the four-quark operators $P_1, \ldots, P_6$ and were completed in [76]. At this order of perturbation theory, the matching of the remaining dipole operators O_7 and O_8 was done in [80]. This is more involved, as it occurs at the three-loop level. In essence, all Wilson coefficients at the electroweak scale are therefore known up to the NNLO.

2.1.4. Mixing

As we are eventually interested in matrix elements of the effective Lagrangian for the $\overline{B} \to X_s\gamma$ decay, i.e. at a scale $\mu \ll \mu_W$, the Wilson coefficients have to be evolved from μ_W down to μ using the renormalization group (RG). Defining the anomalous dimension matrix $\gamma(\alpha_s)$, the RG evolution is given by

$$\mu\frac{d}{d\mu}\vec{C} = \gamma(\alpha_s)\vec{C}, \tag{2.22}$$

where the anomalous dimension matrix is obtained from the renormalization matrix Z_{ij},

$$\gamma_{ij} = Z_{ik}\mu\frac{d}{d\mu}Z_{kj}^{-1}. \tag{2.23}$$

Eqn. (2.22) has the general solution

$$\vec{C}(\mu) = U(\mu,\mu_W)C(\mu_W) \quad \text{with} \quad U(\mu,\mu_W) = T\exp\left(\int_{g(\mu_W)}^{g(\mu)} dg' \frac{\gamma(g'^2)}{\beta(g')}\right). \tag{2.24}$$

Here, $\beta(g)$ is the QCD beta function [5, 6] T is an ordering operator for the values of $g(\mu)$, sorting the integration bounds, analogously to the time ordering in the time evolution operator. The initial values in the solution (2.24) are given by the matching procedure. With the anomalous dimension matrix being non-diagonal, the RG evolution mixes different effective operators under QCD renormalization. It is obvious that $C_i(\mu)\langle P_i(\mu)\rangle$ is a physical quantity and therefore the renormalization scale dependence between the effective couplings and the matrix elements has to cancel up to higher order effects . However, in the case of radiative B decays a puzzle, unsolved for several years, was the fact that matrix elements mediating the $b \to s\gamma$ decay at leading order appear to be regularization scheme dependent. In particular, in the NDR scheme, the tree level matrix elements necessary for the $\overline{B} \to X_s\gamma$ decay are governed by the $P_1,\ldots,P_7$ operators, while in the t'Hooft-Veltman scheme (HV) [54] the only contribution stems from the dipole operator P_7. The reason for this a priori unexpected effect is that the mixing between the four-quark operators and the magnetic operators vanishes at one-loop level. Effectively, what would be a NLO effect in the strong coupling, now becomes only a leading one.
One can account for this scheme-dependence by observing that matrix elements of $P_1,\ldots,P_6$ are actually proportional to the tree level matrix element of P_7 on the mass-shell,

$$\langle P_i\rangle = y_i\langle P_7\rangle. \tag{2.25}$$

In fact, we can define effective Wilson coefficients

$$C_i^{eff}(\mu) = C_i(\mu), \qquad i = 1,\ldots,6 \tag{2.26}$$

$$C_7^{eff}(\mu) = C_7(\mu) + \sum_{i=1}^{6} y_i C_i(\mu), \tag{2.27}$$

$$C_8^{eff}(\mu) = C_8(\mu) + \sum_{i=1}^{6} z_i C_i(\mu). \tag{2.28}$$

with $\vec{y} = (0,0,-\frac{1}{3},-\frac{4}{9},-\frac{20}{3},-\frac{80}{9})$ and $\vec{z} = (0,0,1,-\frac{1}{6},20,-\frac{10}{3})$ in the NDR scheme and the operator basis defined in (2.8). In the leading logarithmic approximation the effective Wilson coefficient of the dipole operator P_7 at the low energy scale reads

$$C_7^{(0),eff}(\mu_b) = \eta^{\frac{16}{23}} C_7^{(0)}(\mu_W) + \frac{8}{3}\left(\eta^{\frac{14}{23}} - \eta^{\frac{16}{23}}\right) C_8^{(0)}(\mu_W) + C_2^{(0)}(\mu_W)\sum_{i=1}^{8} h_i \eta^{a_i} \tag{2.29}$$

with the ratio of strong couplings at different scales $\eta = \alpha_s(\mu_W)/\alpha_s(\mu_b)$. The effective couplings at the electroweak scale were given in the previous chapter and the constants are

$$
\begin{aligned}
h_i &= \left(\frac{626126}{272277}, -\frac{56281}{51730}, -\frac{3}{7}, -\frac{1}{14}, -0.6494, -0.0380, -0.0185, -0.0057\right), \\
a_i &= \left(\frac{14}{23}, \frac{16}{23}, \frac{6}{23}, -\frac{12}{23}, 0.4086, -0.4230, -0.8994, 0.1456\right). \qquad (2.30)
\end{aligned}
$$

Now the leading order $b \to s\gamma$ amplitude can be written as

$$\langle s\gamma|\mathcal{L}|b\rangle = -V_{tb}V_{ts}^{*}\frac{G_F}{\sqrt{2}}C_7^{(0),eff}(\mu_b)\langle P_7\rangle. \qquad (2.31)$$

The cancellations of the scheme dependent parts between the tree level amplitude and the anomalous dimension matrix were verified first in [81, 82] . Consequently, C_7^{eff} is a scheme independent quantity. Therefore, the anomalous dimension matrix γ^{eff} of the effective Wilson coefficients is also independent of the choice of regularization scheme. In general, this matrix after expansion in the strong coupling

$$\gamma^{eff} = \sum_{n\geq 0}\alpha_s^{n+1}\gamma_n^{eff} \qquad (2.32)$$

takes the form

$$\gamma_n^{eff} = \begin{pmatrix} A_n^{6\times 6} & B_n^{6\times 2} \\ 0^{2\times 6} & C_n^{2\times 2} \end{pmatrix}. \qquad (2.33)$$

The vanishing sub-matrix indicates the fact that the dipole operators, being of mass-dimension five, do not induce any divergences in four quark operator amplitudes. At a given loop order n, the mixing within the sectors $\{P_1, \ldots, P_6\}$ and $\{P_7, P_8\}$ is determined from renormalization constants at the $(n+1)$ loop level. In general more problematic is the mixing between sectors in the sub-matrices B_n, that require $(n+2)$-loop renormalization.

Up to NLO, the results for the anomalous dimension matrix can be found in ,[68], while the mixing between dimension five and dimension six operators was independently confirmed in [70]. At NNLO the three loop renormalization for A_2 and C_2 was found in [71] and [72], respectively. A formidable and difficult task, tackled in [73], was the evaluation of the four-loop mixing leading to B_2 thereby completing the anomalous dimension matrix at this level of accuracy.

2.2. Branching ratio

2.2.1. Standard Model predictions and estimates

As already mentioned, the effective theory approach separates short and long distance effects into the Wilson coefficients and matrix elements, respectively. From that follows directly that matrix elements are, in general, nonperturbative quantities. In the case of the $\overline{B} \to X_s\gamma$ decay, however, the branching ratio is a mostly inclusive observable, apart

from effects due to the requirement of a lower cut E_{cut} in the photon energy E_γ. We will discuss these effects, their determination and application to the current predictions in chapter 2.2.3 and neglect them for now. Moreover, the $\overline{B}$ meson, being dominated by the dynamics of the heavy bottom quark, is sufficiently well described by heavy-quark effective field theory (HQET), where nonperturbative corrections are suppressed by the bottom quark mass. Parameters specific to the B meson, like the bottom quark mass or the QCD equivalent of the Fermi motion of the bottom quark within the hadron, can be determined from a variety of measurements and used as input parameters in the HQET. Altogether, the inclusive hadronic decay rate of $\overline{B} \to X_s\gamma$ can be very well approximated within the quark model and thus we have

$$\Gamma(\overline{B} \to X_s\gamma) \sim \Gamma(b \to X_s^{parton}\gamma) + \mathcal{O}\left(\frac{\Lambda^2}{m_b^2}\right). \tag{2.34}$$

with the inclusive partonic decay rate containing all possible final states with strangeness quantum number $S = -1$

$$\begin{aligned} \Gamma(b \to X_s^{parton}\gamma) &= \Gamma(b \to s\gamma) + \Gamma(b \to sg\gamma) + \ldots & (2.35)\\ &= -\frac{G_F^2}{32\pi^4}\alpha_{em} m_b^5 |V_{ts}^* V_{tb}|^2 \sum_{ij} C_i^{eff} C_j^{eff} G_{ij}(\mu). & (2.36) \end{aligned}$$

Here, the second line gives the perturbative decay rate in the weak effective theory with the interference G_{ij} of matrix elements of the operators P_i and P_j. In the phenomenological analysis of the theoretical determination it is customary to express the branching ratio $\mathcal{B}(\overline{B} \to X_s\gamma)$ in terms of different observables, obtained theoretically or by experiment:

$$\mathcal{B}(\overline{B} \to X_s\gamma)_{E_\gamma > E_{cut}} = \mathcal{B}(\overline{B} \to X_c e\overline{\nu})_{exp} \left|\frac{V_{ts}^* V_{tb}}{V_{cb}}\right|^2 \frac{6\alpha_{em}}{\pi C}(P(E_{cut}) + N(E_{cut})) \tag{2.37}$$

where $\alpha_{em} = \alpha_{em}^{OS}$ and a photon cut $E_\gamma > E_{cut}$ is imposed . $N(E_{cut})$ are nonperturbative corrections and the charm quark mass dependence in $B(\overline{B} \to X_c e\overline{\nu})$ is corrected for with the so-called nonperturbative semi leptonic phase-space factor

$$C = \left|\frac{V_{ub}}{V_{cb}}\right|^2 \frac{\Gamma(\overline{B} \to X_c e\overline{\nu})}{\Gamma(\overline{B} \to X_u e\overline{\nu})}. \tag{2.38}$$

The perturbative ratio $P(E_{cut})$ is then given by

$$\frac{\Gamma(b \to X_s^{parton}\gamma)_{E_\gamma > E_{cut}}}{|V_{cb}/V_{ub}|^2 \Gamma(b \to X_u^{parton} e\overline{\nu})} = \left|\frac{V_{ts}^* V_{tb}}{V_{cb}}\right|^2 \frac{6\alpha_{em}}{\pi C} P(E_{cut}). \tag{2.39}$$

This type of normalization has the benefit that uncertainties in the CKM angles and the bottom quark mass cancel due to the correlation of different theory predictions and experimental measurements. Moreover, the quantity C is well known theoretically up

to NNLO [83, 48] and a fit of this prediction to the measured inclusive decay $\overline{B} \to X_c e \overline{\nu}$ determines both C and the charm quark mass m_c with high precision [84].
Up to NNLO in QCD corrections, the right hand side of eqn. (2.37) receives the following contributions

$$P(E_{cut}) + N(E_{cut}) = P(E_{cut})^{(0)} \times \Big[1 + \mathcal{O}(\alpha_{em}) + O(\alpha_s) + \mathcal{O}(\alpha_s^2) + \mathcal{O}\left(\frac{\Lambda^2}{m_b^2}\right) + \mathcal{O}\left(\frac{\Lambda^2}{m_c^2}\right) + \mathcal{O}\left(\alpha_s \frac{\Lambda}{m_b}\right)\Big] \quad (2.40)$$

where $P(E_{cut})^{(0)}$ is the leading order branching ratio, the first line denotes perturbative and the second line nonperturbative effects stemming from higher order corrections in HQET. A more detailed discussion of nonperturbative effects is postponed to chapter 2.2.4 while we focus on the influence of higher order perturbative effects on the branching ratio and their determination in the following.
The impact of electroweak corrections at the NLO in the weak coupling is expected to be of significance only if large logarithms enhance some of those contributions in the same manner as in QCD corrections. The potential dangerous terms originating in electroweak corrections are of the form $\log(m_b^2/m_e^2)$ and $\log(m_W^2/m_b^2)$. The former have been shown to be absent if the on-shell electroweak coupling is used [85] and the latter indeed is present but turns out to be negligible in explicit calculations [85, 86]. All relevant contributions were evaluated in [87] and the numerical impact on the branching ratio is only about 2%. Higher order contributions in this sector are further suppressed by the electroweak coupling and are therefore negligible at the currently desired accuracy.
QCD corrections, on the other hand, dominate the $\overline{B} \to X_s \gamma$ decay and are sizeable at the next-to-leading order in the strong coupling. The first full prediction of the branching ratio at this level of precision was given in [88] and reads

$$\mathcal{B}(\overline{B} \to X_s \gamma)^{\text{NLO}}_{E_\gamma > 1.6\text{GeV}} = (3.57 \pm 0.30) \times 10^{-4} \quad (2.41)$$

Although this result includes all effects at NLO and the leading nonperturbative contributions, these findings are unsatisfactory in different aspects. Firstly, the perturbative series in the strong coupling is only slowly convergent, as the NLO QCD corrections amount to about 25% of the tree level branching ratio. Moreover, as can be seen in fig. 2.5, the residual scale dependence in the scale μ_c is strong, as it remains due to the cut-off of higher loop effects in the charm quark mass. Furthermore, the obtained branching ratio is strongly dependent on the renormalization scheme employed for the charm quark mass. An accurate study of the dependence of the branching ratio on the chosen mass scheme was done at the NLO in [89]. Until then, it was generally assumed that the charm and bottom quark masses are to be taken in the pole mass scheme. In [89] this choice was questioned, arguing that quarks appearing in loops are best described by short-distance masses while the external bottom masses should be treated in a HQET motivated manner. Therefore, the factor m_b^5 in eqn. (2.36) is modified to read $\overline{m}_b(\mu)^2 (m_b^{1S})^3$, where $\overline{m}_b(\mu)$ is the bottom quark $\overline{\text{MS}}$ mass originating from the $P_{7,8}$-operators and m_b^{1S} is the mass in the so-called $1S$ scheme [90] resulting from the

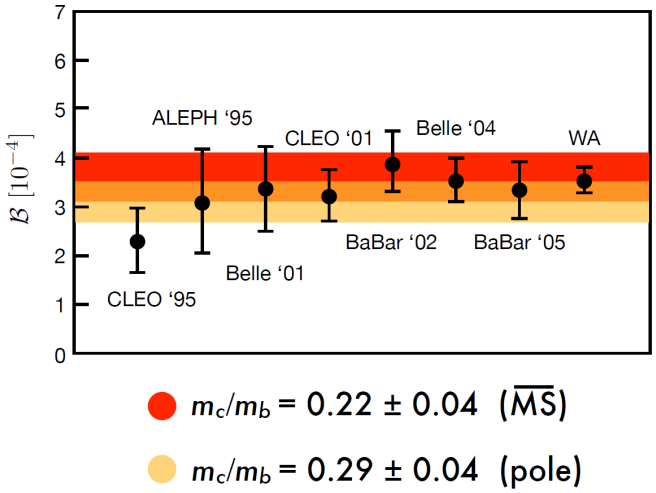

Figure 2.4.: Comparison of the results for the NLO branching ratio of eqn. (2.41) in the pole mass scheme (light region) and in the $\overline{\text{MS}}$ scheme (dark region) with different experimentally obtained values and the current HFAG average. The intermediate shaded region is the overlap between the two theory predictions.

definition of the branching ratio. Furthermore, the charm quark mass appearing in loop propagators is also taken as $\overline{m}_c(\mu)$. It was shown, that the branching ratio at NLO is in principle not sensitive on the choice of bottom mass scheme, but the change $m_c^{pole} \to \overline{m}_c$ results in a sizeable 11% increase in the overall prediction. Fig. 2.4 depicts the branching ratio for the different schemes in comparison to the experimental observed values.
The origin of this scheme dependence is easily understood from the structure of the effective Lagrangian. The only source of charm quark mass dependence in the decay rate are charm quark propagators originating from four quark operators. These operators contribute for the first time at NLO and the charm quark is for the first time renormalized at this level of perturbation theory. At the same time, relations between different mass schemes are NLO effects themselves, therefore the choice of quark mass scheme is only resolved at NNLO.

With these findings at NLO at hand it is obvious that NNLO corrections, which are themselves expected to be of the same size as the current experimental uncertainty, have to be included to reliably match the excellent experimental precision. The central challenge is the reduction of the scheme ambiguity of the charm quark mass. After the efforts of different groups, including the aforementioned matching and mixing as well as the yet to be discussed matrix elements, eventually a first NNLO estimate was published [91]. It is given by

$$\mathcal{B}(\overline{B} \to X_s\gamma)^{\text{NNLO}}_{E_\gamma > 1.6\text{GeV}} = (3.15 \pm 0.23) \times 10^{-4} \tag{2.42}$$

with a photon cut $E_\gamma > 1.6$ GeV in the $\overline{B}$ meson rest frame. Compared to the NLO decay rate, the central value is shifted to smaller values and the overall uncertainty is reduced considerably, being now at the level of the experimental error. The main uncertain-

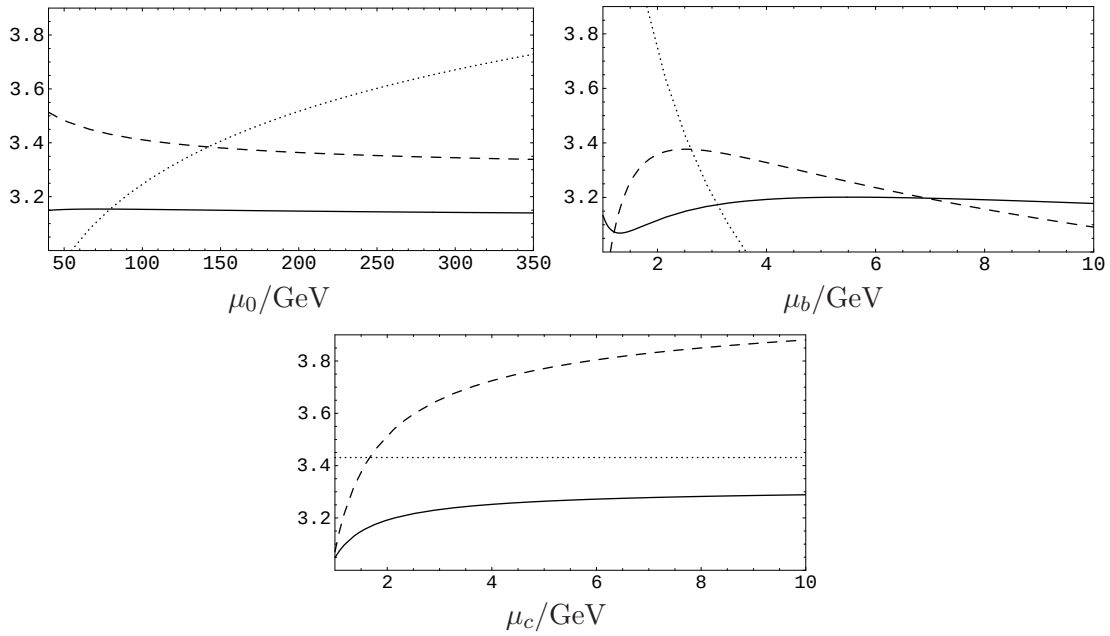

Figure 2.5.: Renormalization scale dependencies of the branching ratio. The dotted, dashed and solid lines indicate the residual scale dependence at LO, NLO and NNLO, respectively.

ties are nonperturbative effects (5%), errors in the input parameters (3%), higher-order contributions (3%) and the so-called charm quark mass interpolation ambiguity (3%). Furthermore, the charm quark mass scale dependence is flattened in comparison to the NLO prediction.
It is not without reason, however, that the value of eqn. (2.42) is called an estimate rather than a prediction. The main source of uncertainty that is of perturbative origin at NNLO arises from only a limited knowledge of charm quark mass dependent matrix elements. In addition, some amplitudes that are rigorously needed in the NNLO estimate are not known at all yet. The so induced error is assumed to be contained in the aforementioned extrapolation ambiguity. In order to give a clearer picture of the available and yet to be computed results, the source of the remaining perturbative uncertainty and its possible resolution, the current status of matrix elements for the $\overline{B} \to X_s\gamma$ decay is summarized in the next chapter.

2.2.2. Matrix elements

In principle, given the operators of eqn. (2.8), the computation of matrix elements contributing to the $b \to s\gamma$ amplitude is a challenging but straightforward quantum field theoretical task. In practice, the structure of the effective field theory complicates matters for higher order QCD corrections to this process considerably, however. On the one hand, as was shown in [89] and is also demonstrated to some extent in the new results of this work in chapter 3, the charm quark mass is not negligible at the relevant

momentum transfer scale $\mu^2 = m_b^2$. Consequently, one has to deal with two-scale multi-loop diagrams with at least three external legs that depend on the charm and bottom quark masses. On the other hand, four quark operators in the amplitude increment the necessary loop level by one, leading to $(n+1)$ loop amplitudes at order α_s^n. At NNLO of the strong coupling, the decay is therefore mediated by at most three-loop two-scale diagrams that have to be evaluated on-shell, which requires state-of-the art techniques. To gain more insight in the general structure of the contributions up to NNLO, the perturbative quantity $P(E_{cut})$ can be expressed as

$$P(E_{cut}) = \sum_{i,j=1}^{8} C_i^{eff}(\mu_b) C_j^{eff}(\mu_b) G_{ij}(E_{cut}, \mu_b). \tag{2.43}$$

and after expanding the effective Wilson coefficients and the corresponding amplitudes in orders of the strong coupling

$$C_i^{eff}(\mu) = \sum_k \alpha_s^k(\mu) C_i^{eff,(k)}(\mu) \tag{2.44}$$

$$G_{ij} = \delta_{i7}\delta_{j7} + \alpha_s(\mu_b) G_{ij}^{(1)} + \alpha_s^2 G_{ij}^{(2)} + \mathcal{O}(\alpha_s^3) \tag{2.45}$$

the perturbative part can be divided into different parts

$$\begin{aligned} P(E_{cut}) &= P^{(0)} + \alpha_s(\mu_b)\left(P_1^{(1)}(\mu_b) + P_2^{(1)}(E_{cut}\mu_b)\right) \\ &\quad + \alpha_s^2(\mu_b)\left(P_1^{(2)}(\mu_b) + P_2^{(2)}(E_{cut}, \mu_b) + P_3^{(2)}(E_{cut}, \mu_b)\right). \end{aligned} \tag{2.46}$$

The amplitude is split in such a way, that the terms $P^{(0)}$ and $P_1^{(n)}$ are generated by tree-level matrix elements of P_7, i.e. the α_s dependence stems from products of the expanded Wilson coefficients only. $P_2^{(2)}$ is proportional to products of the form $C_i^{eff,(0)} C_j^{eff,(1)}$ and the corresponding matrix elements are $G_{ij}^{(0)}$ and of NLO in the QCD coupling. The most interesting term is $P_3^{(2)}$, which depends on only the LO effective couplings and contains the most complicated matrix elements $G_{ij}^{(2)}$.

The complexity of these calculations for the $\overline{B} \to X_s\gamma$ decay can be inferred from the history of publications leading to the NLO prediction of the branching ratio. Even though the NLO programme was initiated in 1993 with [92], only eight years later the full amplitude became available. A complete list of references to the evaluation of NLO matrix elements can be found e.g. in [93].

At NNLO, although a lot of effort has been put into the evaluation of matrix elements by various groups, this task is not completed yet. It is important to note, that due to the smallness of the Wilson coefficients $C_3, \ldots, C_6$, the numerically relevant contributions stem from $G_{i,j}$ with $i, j \in \{1, 2, 7, 8\}$. So far, only the contribution G_{77} is fully available up to $\mathcal{O}(\alpha_s^2)$. This constitutes the two-loop matrix elements of the dipole operator P_7 and the corresponding bremsstrahlung [94, 95], a result that was confirmed [96] and subsequently extended to include the full charm quark mass dependence in [97].

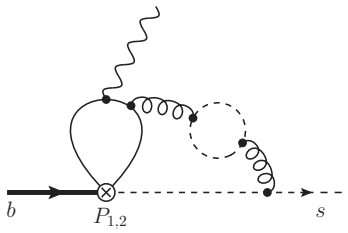

Figure 2.6.: Example diagram contributing to massless fermionic corrections of $P_{1,2}$ matrix elements at NNLO.

Of particular importance for the $b \to s\gamma$ decay rate are the matrix elements $G_{1i}^{(2)}$ and $G_{2i}^{(2)}$ which are charm quark mass dependent and therefore quite challenging. A comparatively simple subset of these contributions is given by diagrams generated from those at NLO by dressing the gluon lines with fermionic loops of mass m_l (fig. 2.6). These fermionic corrections are then of $\mathcal{O}(n_f \alpha_s^2)$, where n_f is the number of active flavours, and purely massless correction with $m_l = 0$ to the matrix elements of the $P_{1,2}$ as well as the dipole operators $P_{7,8}$ were determined in [98] in terms of expansions in the mass ratio m_c^2/m_b^2. It is important to notice that the charm quark mass dependence in these results is generated solely from charm loops originating from the P_1 and P_2 operators.
Having the fermionic corrections at hand, it is tempting to apply the so-called naive non-abelianization (NNA) [99] to estimate the missing bosonic corrections in $G_{ij}^{(2)}$. The basic idea behind NNA is the observation, that the leading term of the β-function of QCD,

$$\beta_0 = 11 - 2/3\, n_f, \tag{2.47}$$

is comparatively large and the replacement $n_f \to -3/2\beta_0$ might lead to a good approximation of the full NNLO corrections. Indeed, in many physical observables like the inclusive cross-section in electron positron annihilation to hadrons [100, 101] or the semi-leptonic decay $b \to c l \nu_l$ [102] the hypothesis of NNA provides an excellent estimate of the full two-loop contributions.
Splitting $G_{ij}^{(2)}$ into the known fermionic corrections F_{ij} and the yet unknown bosonic contributions B_{ij},

$$G_{ij}^{(2)} = n_f F_{ij} + B_{ij}, \tag{2.48}$$

the application of the NNA leads to

$$G_{ij}^{(2)} = G_{ij}^{(2)\beta_0} + G_{ij}^{(2),rem} \tag{2.49}$$

with

$$G_{ij}^{(2)\beta_0} = -\frac{3}{2}\beta_0 F_{ij} \tag{2.50}$$

$$G_{ij}^{(2),rem} = \frac{33}{2} F_{ij} + B_{ij} \tag{2.51}$$

As the findings of [98] for the $m_l = 0$ fermionic corrections to the matrix elements $G_{17}^{(2)}$ and $G_{27}^{(2)}$ are important for this work, let us quote the results with applied NNA explicitly

$$\begin{aligned} G_{27}^{(2)\beta_0}(m_l=0) &= \beta_0 \mathrm{Re}\left[-\frac{3}{2}r_2^{(2)}(z) + 2\left(a(z)+b(z)-\frac{290}{81}\right)\text{Ł}_b - \frac{100}{81}\text{Ł}_b^2\right] + 2\phi_{27}^{(2)\beta_0}(\delta) \\ G_{17}^{(2)\beta_0}(m_l=0) &= -\frac{1}{6}G_{27}^{(2)\beta_0} \end{aligned} \tag{2.52}$$

where $z = m_c^2/m_b^2$ and $L_b = \log(m_b^2/\mu_b^2)$. $\phi_{27}^{(2)\beta_0}(\delta)$ with $\delta = 1 - 2E_{cut}/m_b$ is responsible for the implementation of the cut in the photon energy and expected to be negligible [103]. The functions $a(z)$ and $b(z)$ are known exactly in terms of their integral representations [88] which in the small m_c limit are given by

$$\begin{aligned} a(z) &= \frac{16}{9}\left\{\left[\frac{5}{2}-\frac{\pi^2}{3}-3\zeta_3+\left(\frac{5}{2}-\frac{3\pi^2}{4}\right)L_z+\frac{1}{4}L_z^2+\frac{1}{12}L_z^3\right]z+\left(\frac{7}{4}+\frac{2\pi^2}{3}-\frac{\pi^2}{2}L_z\right.\right. \\ &\quad \left.-\frac{1}{4}L_z^2+\frac{1}{12}L_z^3\right)z^2+\left[-\frac{7}{6}-\frac{\pi^2}{4}+2L_z-\frac{3}{4}L_z^2\right]z^3+\left(\frac{457}{216}-\frac{5\pi^2}{18}-\frac{1}{72}L_z\right. \\ &\quad \left.-\frac{5}{6}L_z^2\right)z^4 i\pi\left[\left(4-\frac{\pi^2}{3}+L_z+L_z^2\right)\frac{z}{2}+\left(\frac{1}{2}-\frac{\pi^2}{6}-L_z+\frac{1}{2}L_z^2\right)z^2\right. \\ &\quad \left.\left.+z^3+\frac{5}{9}z^4\right]\right\}+\mathcal{O}(z^5L_z^2), \end{aligned} \tag{2.53}$$

$$\begin{aligned} b(z) &= -\frac{8}{9}\left\{\left(-3+\frac{\pi^2}{6}-L_z\right)z-\frac{2\pi^2}{3}z^{3/2}+\left(\frac{1}{2}+\pi^2-2L_z-\frac{1}{2}L_z^2\right)z^2\right. \\ &\quad +\left(-\frac{25}{12}-\frac{1}{9}\pi^2-\frac{19}{18}L_z+2L_z^2\right)z^3+\left(-\frac{1376}{225}+\frac{137}{30}L_z+2L_z^2+\frac{2\pi^2}{3}\right)z^4 \\ &\quad \left.+i\pi\left[-z+(1-2L_z)z^2+\left(-\frac{10}{9}+\frac{4}{3}L_z\right)z^3+z^4\right]\right\}+\mathcal{O}(z^5L_z^2), \end{aligned} \tag{2.54}$$

with $L_z = \log z$. The quantity $r_2^{(2)}$ is known only in the small m_c limit and reads

$$\begin{aligned} \mathrm{Re}\, r_2^{(2)}(z) &= \frac{67454}{6561}-\frac{124\pi^2}{729}-\frac{4}{1215}\left(11280-1520\pi^2-171\pi^4-5760\zeta_3+6840L_z\right. \\ &- \left.1440\pi^2L_z-2520\zeta_3L_z+120L_z^2+100L_z^3-30L_z^4\right)z \\ &- \frac{64\pi^2}{243}\left(43-12\ln 2-3L_z\right)z^{3/2}-\frac{2}{1215}\left(11475-380\pi^2+96\pi^4+7200\zeta_3\right. \\ &- \left.1110L_z-1560\pi^2L_z+1440\zeta_3L_z+990L_z^2+260L_z^3-60L_z^4\right)z^2 \\ &+ \frac{2240\pi^2}{243}z^{5/2}-\frac{2}{2187}\left(62471-2424\pi^2-33264\zeta_3-19494L_z-504\pi^2L_z\right. \\ &- \left.5184L_z^2+2160L_z^3\right)z^3-\frac{2464}{6075}\pi^2z^{7/2}+\left(-\frac{15103841}{546750}+\frac{7912}{3645}\pi^2+\frac{2368}{81}\zeta_3\right. \\ &+ \left.\frac{147038}{6075}L_z+\frac{352}{243}\pi^2L_z+\frac{88}{243}L_z^2-\frac{512}{243}L_z^3\right)z^4+\mathcal{O}(z^{9/2}L_z^4). \end{aligned} \tag{2.55}$$

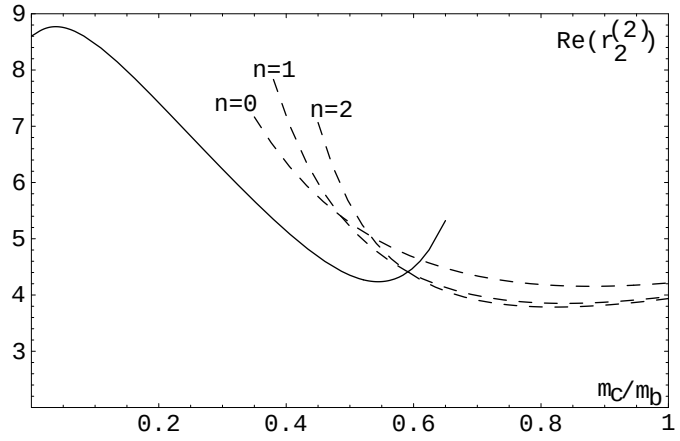

Figure 2.7.: Plot of the quantities $r_2^{(2)}$, $a(z)$ and $b(z)$ needed in $G_{i7}^{(2)\beta_0}$ as functions of the mass ratio $z = m_c/m_b$. The solid lines represent the small m_c expansion of [98] and the dashed lines show the nth terms in the large m_c limit from [103].

Finally, an important contribution was made in [103], where, apart from G_{78} and G_{88}, the full NNLO corrections to the matrix elements where evaluated, albeit in the artificial limit $m_c^2 \gg m_b^2$. These results for the first time provided the large-m_c expansion of $a(z)$, $b(z)$ and $r_2^{(2)}(z)$ and thereby $G_{17}^{(2)\beta_0}$ and $G_{27}^{(2)\beta_0}$ up to $\mathcal{O}(z^{-2})$ as well as the leading term of the full bosonic corrections, $P_3^{(2)rem}$ in this limit. Interestingly, already the few available terms for $m_c < m_b/2$ of eqn. (2.55) and the new results for the fermionic contributions in the domain $m_c > m_b/2$ were shown to match nicely at around $z = 0.6$ (compare fig. 2.7). Motivated by this observation, the authors of [103] then used the newly obtained large-m_c expansion of $P_3^{(2)rem}$ to estimate this quantity in the physical quark mass ratio at $m_c < m_b/2$. Since $P_3^{(2)rem}$ is yet unknown for small charm quark masses, different assumptions about both the value at $m_c = 0$ and the functional dependence of the missing matrix elements in this domain have to be made. We refer the reader to the original paper for further details and show in fig. 2.8 only the resulting plot of the employed extrapolation.

As can be seen, the different assumptions at $m_c = 0$ lead to an uncertainty in the indicated physical mass ratio, that amounts to the aforementioned extrapolation uncertainty of about 3% in the NNLO branching ratio. It has again to be stressed, that in this analysis contributions in the large-m_c limit of G_{78} and G_{88} as well as the fermionic corrections of G_{18} and G_{28} were not included.

Altogether, it is obvious that the performed extrapolation is a powerful tool to obtain an approximation of the missing matrix elements and only this evaluation has made a reliable estimate of the decay rate at $\mathcal{O}(\alpha_s^2)$ possible. However, as the induced error is of purely perturbative origin at the same level of accuracy, a full evaluation is desirable, especially of matrix elements of the $P_{1,2}$ operators . On the one hand, these matrix elements have sizeable effective couplings and therefore are numerically important. On

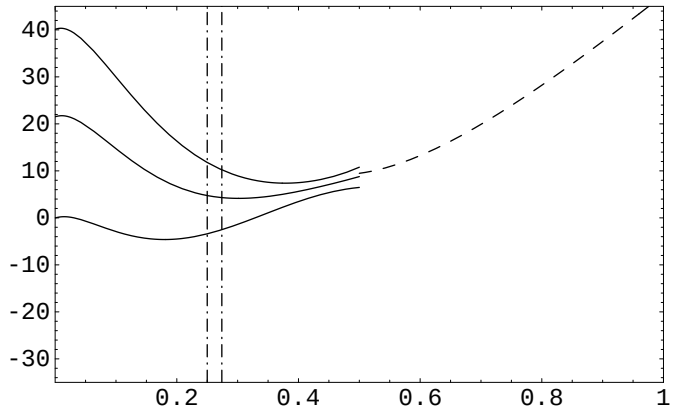

Figure 2.8.: Plot of the extrapolation employed for $G_{ij}^{(2),rem}$. The dashed line represents the leading term in the large m_c of the remaining contributions, while the solid lines depict the three different ansätze used for the extrapolation. The vertical dash-dotted lines indicate the uncertainty bounds for the quark mass ratio m_b/m_c.

the other hand they dominate the charm quark mass dependence of the branching ratio. Therefore, reducing or even eliminating the uncertainty of the extrapolation is possible in two different ways. On the one hand, computing the matrix elements of $P_{1,2}$ at the physical mass scale, i.e. with both charm and bottom quark masses finite would make the extrapolation obsolete and remove the so induced uncertainty. On the other hand, a knowledge of G_{17} and G_{27} for only $m_c = 0$ already would have a big impact, as it could uniquely fix the major contribution to the extrapolation limit.
Finally, it has to be noted that even after completion of this task, some missing parts remain, namely the full NNLO QCD corrections to G_{78} and G_{88}, a computation that is currently under way [104, 105] as well as the extremely challenging two-loop times two-loop contribution of G_{12}, G_{21} and G_{22}.

2.2.3. Photon spectrum and inclusiveness

Let us now turn to the requirement of a cut on the photon energy in the $\overline{B} \to X_s\gamma$ decay and its influence on the validity of theoretical predictions and their comparison with measurements.
From the experimental point of view, an inclusive measurement of the $\overline{B} \to X_s\gamma$ branching ratio is plagued by a large background, that interferes with the clean signal of the pure $\overline{B} \to X_s\gamma$ transition. The main source of background is contamination with the transitions $b \to c\gamma$ and $b \to d\gamma$, but also events with photon production through annihilation of intermediate resonances like π^0 or η are removed as background. These uninteresting events occur predominantly below a photon energy of around $E_{cut}^{exp} \sim 1.8$ GeV in the B meson rest-frame and are discarded in the analysis of the decay rate and hence the branching ratio. A recent plot of the measured photon spectrum is depicted in fig. 2.9.

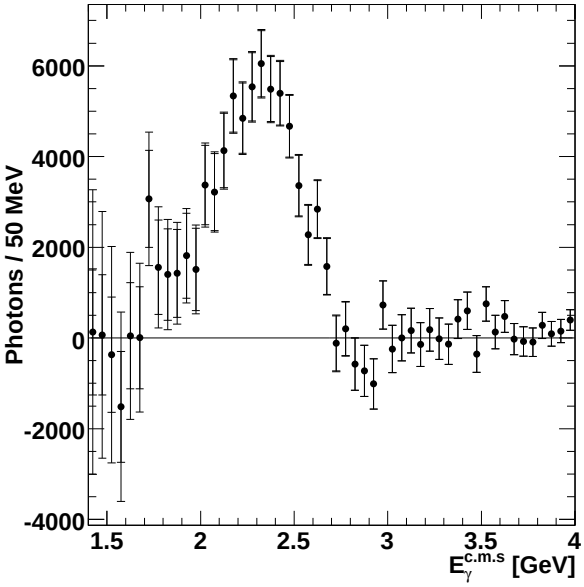

Figure 2.9.: Photon spectrum in the $\overline{B} \to X_s\gamma$ decay as measured by Belle. The used signal region for the branching ratio determination in this experiment is $E_\gamma = [1.8, 2.7]$ GeV.

The relevant signal region lies between 1.7 and ∼2.7 GeV. The shape of the spectrum reflects the basic expectation from the simple two-body decay, that the photon energy has to lie in the interval $0 < E_\gamma < m_B/2$, where m_B is the mass of the decaying B meson.

Notice however, that the current world average of the branching ratio is published with $E_\gamma > E_{cut} = 1.6$ GeV, outside a region where the two most precise experiments having $E_{cut}^{exp} = 2.0$ GeV and $E_{cut}^{exp} = 1.8$ GeV are actually performed. Here, nonperturbative theory input for the shape function is needed [106] to extrapolate the measured branching ratio down to E_{cut}. A recent refined analysis [107] of the required function could further improve the HFAG averages.

On the theory side, in the absence of QCD, the two body decay in the parton model $b \to s\gamma$ would lead to a δ-distribution of the photon spectrum. Hard QCD exchange of partons at higher orders of the perturbative series, then leads to a washed out spectrum, with the kinematical endpoint of the spectrum lying in $E_\gamma = m_b/2$. In reality, however, the shape is considerably broadened due to the confinement of both the initial and final partonic states in hadrons. The characteristic width of this decay is of the order of $\Lambda = m_B - m_{X_s}$, where m_{X_s} is the invariant mass of the accessible hadronic final states. The endpoint of the spectrum is measured to lie around $E_\gamma = m_B/2$, but extends to even higher energies with the characteristic width of Λ. Imposing a cut in the photon energy on the theoretical prediction in the parton model, thereby discarding the events

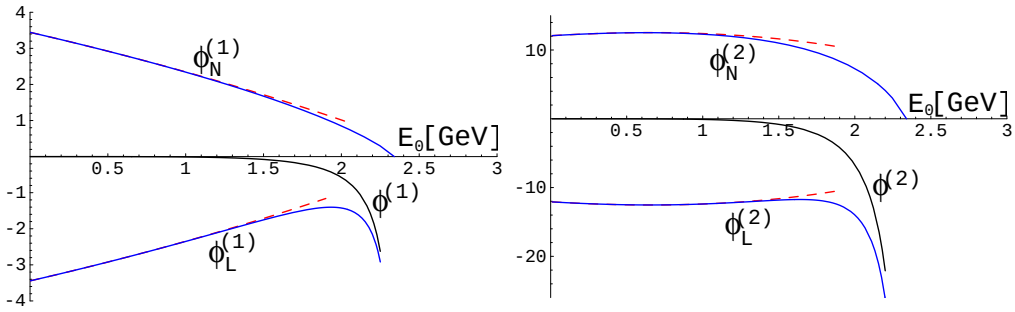

Figure 2.10.: Dependence of the perturbative prediction of the photon spectrum at NLO (a) and NNLO (b), split into logarithmic ϕ_L and finite parts ϕ_N together with their sum.

below the cut, requires a good knowledge of the photon spectrum. It seems obvious, that a proper subtraction has to be done a priori in a nonperturbative picture. As it turns out, however, fixed-order perturbation theory approximates the problem at hand particularly well for $E_{cut} \leq 1.6$ GeV.
In eqn. (2.37) the perturbative quantity $P(E_{cut})$ depends on the imposed cutoff that can be parametrized as

$$\delta = 1 - \frac{2E_{cut}}{m_b}. \tag{2.56}$$

In the region $\delta \sim 1$, on the one hand the theoretical quantity $\Gamma(b \to s\gamma)$ would give an excellent estimate of the fully inclusive $\overline{B} \to X_s\gamma$ decay, which is unfortunately not observable as mentioned above. On the other hand, a perturbative calculation of the photon spectrum, carried out up to $\mathcal{O}(\alpha_s^2)$ in [94] approximates the true spectrum considerably well. However, close to the endpoint region, that is for small values of δ, the fixed order perturbative expansion expectedly breaks down as the corrections behave as polynomials in $\log \delta$.
The main contribution to the photon spectrum sufficiently far away from the endpoint can be assumed to be mediated by the dipole operator P_7 and neglecting all other operators, the α_s expansions of the cutoff dependence becomes

$$\frac{P(E_{cut})}{P(0)} = 1 + \alpha_s\phi^{(1)}(\delta) + \alpha_s^2\phi^{(2)}(\delta) + O(\alpha_s^3) \tag{2.57}$$

where $\phi^{(1)}$ and $\phi^{(2)}$ where determined in [108] and [104], respectively. To analyze the influence of potentially dangerous logarithms, one can split the functions $\phi^{(n)}$ according to

$$\phi^{(n)} = \phi_L^{(n)} + \phi_N^{(n)} \tag{2.58}$$

where the large logarithms for $\delta \to 0$ are absorbed in $\phi_L^{(n)}$ while $\phi_N^{(n)}$ vanishes in this limit. Fig. 2.10 shows the terms on the right hand side of (2.58) independently and their sum for $n = 1$ and $n = 2$. As expected, the perturbative description breaks down at around $E_{cut} = 2$ GeV. It is remarkable however, that huge cancellations between

the logarithmic part occur below this point and it can be argued, that the perturbation theory prediction of the photon spectrum is very well valid up to $E_{cut} = 1.6$ GeV.
With the results of [94] the NNLO branching ratio can be determined for lower cutoffs with the numerical fit [91]

$$\left(\frac{\mathcal{B}(\overline{B} \to X_s\gamma)_{E_\gamma > E_0)}}{\mathcal{B}(\overline{B} \to X_s\gamma)_{E_\gamma > 1.6\,\mathrm{GeV}}} \right) \approx 1 + 0.15\,x - 0.14\,x^2 \tag{2.59}$$

with $x = 1 - E_0/(1.6\,\mathrm{GeV})$.
Let us here also mention that an alternative $\overline{B} \to X_s\gamma$ branching ratio estimate at the level of NNLO exists. First, the fixed order computation of the photon spectrum was extended to include a resummation of the large logarithms [109, 110, 111] and subsequently these findings were used to extrapolate the photon energy cut on the theoretical branching ratio from $E_{cut} = 1.0$ GeV, a result that was also obtained in [91]. Due to the aforementioned cancellations in the region $E_{cut} \in [1.0, 1.6]\,\mathrm{GeV}$, however, a resummation of logarithms overestimates the fixed order calculation in this domain by a factor of two in the worst case. Eventually, this leads to a considerably smaller value for the branching ratio, which, with the arguments above, should be considered unreliable.

2.2.4. Nonperturbative effects

The study of nonperturbative effects in the context of radiative hadronic B meson decays reveals a rich structure of different components, that can - to some extent - be assessed within the context of HQET. The interesting quantity for inclusive B meson decays in this respect is the discontinuity of the forward scattering amplitude,

$$T = i \int dx\, \langle B|T P_7^\dagger(x) P_7(0)|B\rangle. \tag{2.60}$$

In the limit of large bottom quark mass that sets the scale for the B decay, one can apply the operator product expansion (OPE) on the time ordered product in eqn. (2.60). Employing the picture of HQET, where the bottom quark mass is taken to be infinitely heavy and therefore acts as a static on-shell source of color, the fraction of decay rate due to P_7 has the general structure

$$\Gamma(\overline{B} \to X_s\gamma)_{P_7} = \frac{G_F^2}{(2\pi)^4} \alpha_{em} m_b^5 |V_{tb}V_{ts}^*|^2 |C_7^{eff}(m_b)|^2 \left[1 + \frac{1}{m_b} f_1 + \left(\frac{1}{m_b}\right)^2 f_2 + \dots \right]. \tag{2.61}$$

Let's assume for now that the $\overline{B} \to X_s\gamma$ decay is mediated by the dipole operator P_7 only and that QCD corrections are negligible. In this setup, the radiation of a photon from the hard process of the bottom quark decay can be reliably computed through the inclusion of the first subleading terms in the $1/m_b$ expansion. The resulting coefficients f_i were obtained in [112, 113] and read

$$f_1 = 0, \quad f_2 = \lambda_1 - 9\lambda_2 \tag{2.62}$$

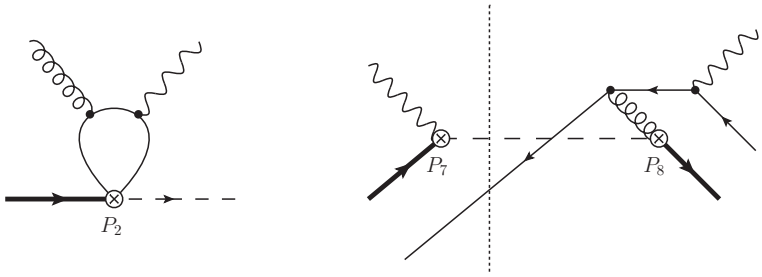

Figure 2.11.: (a) Diagram contributing to charm-dependent non-perturbative corrections (b) Interference of P_7 and P_8 described by a non-local operator in HQET.

Here, the λ_i are HQET parameters for the B meson, which are not specific to a certain decay channel and can be extracted from different measurements. The first subleading contribution in this scenario is formally suppressed by $\mathcal{O}(\Lambda^2/m_b^2)$ and, provided that the cut on the photon energy is not too close to the kinematical endpoint, it is quite small with around -3%. In fact, in the normalization of the branching ratio in eqn. (2.37), this effects cancel with the corresponding nonperturbative part in the semi-leptonic decay and the remainder is only of $\mathcal{O}(\Lambda^3/m_b^3)$.
Another possible source of nonperturbative effects originates from the application of the photon energy cut, that introduces an additional intermediate scale $\mu_I = m_b - 2E_{cut}$. A careful investigation [114] of these contributions shows that they are of $\mathcal{O}(\Lambda^2/\mu_I^2)$ and are only small. The combination of the residual $\mathcal{O}(\Lambda^3/m_b^3)$ and $\mathcal{O}(\Lambda^2/\mu_I^2)$ parts affects the NNLO branching ratio by only -0.7%.
Relaxing the above assumption and allowing for other operators than P_7, the discussion of nonperturbative effects becomes much more complex. Now, the photon may couple to light quarks at a space-time point separation larger than $1/\Lambda$ and, as was noted in [115], in general the OPE breaks down. In a series of publications [116, 115, 117, 118, 119], it was shown that nonperturbative contributions, where the photon is emitted from charm quarks in a process involving the $P_{1,2}$ operators together with soft gluons from the remnants of the B-meson (compare fig. 2.11 (a)), can only be expressed by matrix elements involving an infinite sum of operators. The corresponding terms are then of the order of

$$\Gamma(\overline{B} \to X_s\gamma) \sim \frac{\Lambda^2}{m_c^2} \sum_{n=0}^{\infty} b_n \left(\frac{\Lambda m_b}{m_c^2}\right)^n \tag{2.63}$$

where the coefficients b_n decrease rapidly with increasing n. It is assumed that the leading order term,

$$b_0 = -\frac{\lambda_2}{9} \frac{C_2(m_b)}{C_7^{eff}(m_b)} \tag{2.64}$$

approximates the sum in eqn. (2.63) satisfactory. The overall impact amounts to around 3.1% of the NNLO branching ratio.
A further process that has to be taken into account is the collinear radiation of a photon

in the process of hadronization, which is accompanied by gluon or $q\overline{q}$ emission and therefore suppressed by α_s but not necessarily by the bottom quark mass. On general grounds, these contributions are additionally suppressed by ratios of Wilson coefficients and more importantly by the imposed photon energy cutoff [104]. An interesting example with this respect is a contribution where the b quark decays via the chromomagnetic operator P_8 and the photon is emitted from the light quark. In this case, the photon radiation can be estimated in terms of fragmentation functions and turns out to be important only for photon energies below 1 GeV [120]. Hence, the influence on the NNLO branching ratio is numerically very small (-0.2%).
Quite recently [121], a new class of nonperturbative corrections was identified that can be described as parton-to-photon conversion. In this process, the b quark decays via hard momentum exchange into quarks and gluons. A subsequent soft scattering in the QCD medium, i.e. with the spectator cloud of the B meson, leads to the photon emission. A characteristic diagram for this scattering is shown in fig. 2.11 (b). This contribution is expected to be of the order of $\alpha_s\Lambda/m_b$, where the ratio originates from the dilution of the soft-scattering target and the strong coupling from the scattering itself. This transition is mostly relevant at the endpoint of the photon spectrum that is best accessible in measurements and can not be removed by kinematical cuts. In terms of forward scattering amplitudes of the B meson, the decay rate in this case can only be expressed with a nonlocal operator and the actual evaluation is rather challenging. Although the authors of [121] were able to give an estimate of these effects, only few parts contributing to the scattering amplitude were taken into account. Among others, a particularly interesting transition involving intermediate $c\overline{c}$ states was left out. Altogether, the suggested estimate for the so induced nonperturbative effect was given to be around 5%.
Summing all aforementioned nonperturbative effects, the relative contribution amounts to

$$\Gamma_{NP} = 3.1\% - 1.5\% - 0.2\% - 0.7\% + 5\% = 4.3\%. \tag{2.65}$$

As the evaluation of nonperturbative effects is often dependent of crude approximations leading to a strong uncertainty and moreover not all contributions are available yet, a conservative error estimate $\delta_{NP} = 5\%$ for the NNLO branching ratio as given below eqn. (2.42) is assumed.

3. Charm dependent matrix elements at NNLO

3.1. Full fermionic corrections at NNLO

As already mentioned in chapter 2.2.2, massless fermionic corrections to the matrix elements of the operators P_1 and P_2 at NNLO, where only the internal charm quark loop from the four-quark operator and the external bottom quark are considered massive were determined in [98]. In this chapter, we focus on the independent evaluation of this contribution and moreover extend our study to include mass induced effects.
Performing an independent cross-check of the findings of [98] for the massless corrections is important, as they are used as a direct input in the current NNLO estimate of the branching ratio. In fact, in [103], the massless corrections make up a major part in the ansatz for the estimation of yet unknown bosonic contributions (compare section 2.2.2). Prior to the publication of the work presented here [122], such a cross-check has not been provided. Moreover, these results are known only as an expansion in the mass ratio $z = m_c^2/m_b^2$. Although they are expected to give a very good approximation at the physical z, an exact result is desirable. In addition, from a technical point of view, these matrix elements serve as an excellent testing ground of the methods employed here , since a direct comparison can be performed.
In the SM estimate of the $\overline{B} \to X_s\gamma$ branching ratio at NNLO, as only massless results were available at $\mathcal{O}(\alpha_s^2 n_f)$, all matrix elements are treated in a five-flavour scheme neglecting the charm and bottom mass in quark loops inserted in gluon propagators, thereby assuming that heavy contributions are reasonably well described in the massless limit. Due to the fact that the charm and bottom quarks are heavy relative to the three light flavours, it is important to study the size of their effect on the matrix elements as massive particles and allow for further analysis of their impact on the branching ratio.
In this part, we provide the exact results for both massless and massive fermionic corrections to the matrix elements of $P_{1,2}$ as well as confirm the computation of [98].

3.1.1. Matrix elements

All matrix elements contributing at $\mathcal{O}(\alpha_s^2 n_f)$ are given by three loop vertex diagrams, which are generated through fermion loop insertions into gluon propagators of NLO diagrams. Example diagrams are depicted in fig. 3.1. The external bottom quark is held on mass-shell, $p^2 = m_b^2$, and charm quark loops stemming from the four-fermion operators are kept massive. Depending on the flavour in the subloop, three different fermion masses have to be taken into account: up-, down- and strange-quarks are treated

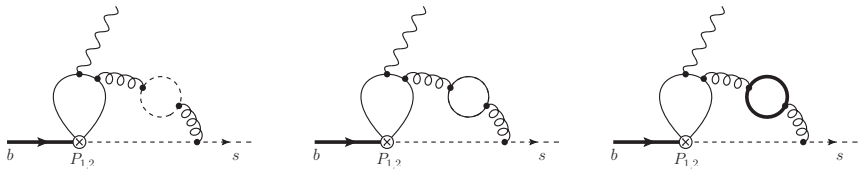

Figure 3.1.: Example diagrams contributing to the fermionic corrections of NNLO matrix elements.

massless while the charm- and bottom-masses are kept at their physical values in the $\overline{\text{MS}}$ scheme. For convenience, we split the calculation according to the fermionic subloop mass into three different parts, each requiring slightly different approaches.
In the following, we concentrate on the derivation of matrix elements of the operator P_2. The result for P_1 insertions at $\mathcal{O}(\alpha_s^2 n_f)$ can be determined from

$$\langle s\gamma|P_1|b\rangle = -\frac{1}{2N_c}\langle s\gamma|P_2|b\rangle. \tag{3.1}$$

This relation is valid at NLO and holds also for fermionic corrections at NNLO. Fermion loop insertions in gluon propagators do not change the color structure of the vertex diagrams, as can be seen in figure 3.1. In case of bosonic corrections, however, the color structure is changed and eqn. (3.1) is not applicable. A simple example is given in fig. 3.2, where the color algebra for this particular diagram with P_1 and P_2 insertions leads to the following color coefficients:

$$P_1: \quad C_A\, C_F\, N_c - 2C_F^2\, N_c, \tag{3.2}$$
$$P_2: \quad C_A^2\, C_F\, N_c + C_A\, C_F^2\, N_c - 2C_F^3 N_c. \tag{3.3}$$

As far as the renormalization of ultraviolet divergences is concerned, matrix elements up to NLO for the operators P_1, P_2, P_4 and P_7 of eqn. (2.8) and, in addition, of the evanescent operator

$$P_{25} = (\overline{s}_L\gamma_\mu\gamma_\nu\gamma_\rho T^a c_L)(\overline{c}_L\gamma^\mu\gamma^\nu\gamma^\rho T^a b_L) - 16P_1 \tag{3.4}$$

have to be evaluated. Here one follows the general prescription given in eqn. (2.14), but other operators are not needed, because they either do not mix at the NNLO level or their matrix elements vanish. The strong coupling α_s and the charm-quark mass m_c

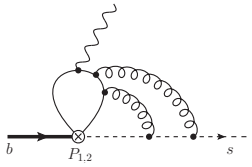

Figure 3.2.: Example diagram of bosonic corrections.

are renormalized in the $\overline{\text{MS}}$ scheme. A renormalization of the bottom quark mass is not needed and therefore the 1S-mass scheme, as motivated in chapter 2.2, is directly applied. As the $\overline{\text{MS}}$ scheme is mass independent, the counterterms needed for the massless and massive fermionic corrections are equal. More details can be found in [98].

3.1.2. Computation

After generating all diagrams with the package `DiaGen` [123], the Dirac and color structures are simplified using the respective algebras and the amplitude can be cast into the following form:

$$\langle s\gamma|P_{1,2}|b\rangle_{\mathcal{O}(\alpha_s^2 n_f)} = \left(\frac{\alpha_s}{4\pi}\right)^2 m_b\, n_f\, \langle s\gamma|P_{1,2}|b\rangle_{n_f}^{(2),M} \overline{u}_s\, P_R \not{\epsilon}\not{q} u_b \tag{3.5}$$

The photon polarization and momentum are given by ϵ and q, respectively, m_b is the pole bottom quark mass and n_f is the number of active flavours. The results are given for each mass $M = \{0, m_c, m_b\}$ of the inserted fermion subloop separately, while the superscript (2) denotes the order in α_s.
The quantity $\langle s\gamma|P_{1,2}|b\rangle_{n_f}^{(2),M}$ is a linear combination of a large number of three-loop scalar integrals multiplied by invariants of the color gauge group and depends on the ratio $z = m_c^2/m_b^2$ and the renormalization scale μ. Upon reducing these integrals with the help of integration-by-parts identities, one is left with a smaller number of master integrals. In the $M = 0$ case, 18 master integrals appear while the massive cases lead to 47 and 38 master integrals for the $M = m_b$ and $M = m_c$ loop insertions, respectively.
The master integrals are then obtained with the method of asymptotic expansions and numerical evaluation from differential equations. To compute a starting point for the numerical integration, here we choose the artificial limit $m_c^2 \gg m_b^2$. This way, the external legs can all be fixed on-shell and differential equations are effectively only derived with respect to the charm quark mass, which is now required to be a free variable. This continuation to arbitrary values of the charm quark mass, however, requires an extended integration by parts reduction leading to a larger number of master integrals, where the original master integrals are contained as subsets.
In addition, master integrals appearing in the massless case were obtained with a second approach utilizing Mellin-Barnes (MB) integral representations of multi-loop integrals [58, 59]. For this task, MB representations were obtained with an automatized software [124] and analytically continued with help of the `MB` package . Here it was also possible to evaluate the asymptotic limit $m_b^2 \gg m_c^2$, which is not directly accessible with the method of differential equations. One ends up with infinite series over residues that can be summed up with `XSummer` [125]. Moreover, numerical evaluations over the whole interesting domain of z were also possible using `MB`. All integrals obtained numerically are in perfect agreement with those determined with the method of differential equations.

3.1.3. Results

After evaluation of the master integrals for a discrete set of points in z, all fermionic corrections to the matrix elements are obtained numerically. To account for future shifts

Input parameter	experimental value
m_b^{1S}	(4.68 ± 0.03) GeV [83]
$m_c(m_c)$	$(1.224 \pm 0.017 \pm 0.054)$ GeV [48]

Table 3.1.: Experimental inputs relevant for the present calculation .

in the mean values and uncertainties of quark masses, the range of z was chosen to allow for a 3σ variation of both m_c and m_b^{1S}. This leads to $Z = z \in [0.017, 0.155]$ for the current input as given in tab. 3.1, with a central value of $z = 0.068$. To facilitate the evaluation for different values of z, the final results are given in terms of fitting formulae that are valid in the range of variation of z chosen here. The ansatz for the fit, that includes terms up to z^2 as well as a logarithm of the form $z \log z$ is motivated by the structure found in the expressions of the small z expansion, which leads to a significant improvement of the obtained fitting functions.

For massless quark loop insertions, the result reads

$$\begin{aligned} \mathrm{Re}\langle s\gamma|Q_2|b\rangle_{n_f}^{(2),0} &= 9.080 - 0.7624\,z - 5.069\,z^2 + 12.61\,z\,\ln z \\ &+ (-9.679 + 5.157\,z + 1.726\,z^2 - 16.18\,z\,\ln z)\ln(m_b/\mu) \\ &+ \frac{800}{243}\ln^2(m_b/\mu). \end{aligned} \tag{3.6}$$

Fig. 3.3 shows the plot of the computed data points together with the obtained fitting function. The fit reproduces all data points with a relative precision of at least 10^{-4} and lies atop the previously obtained result of [98] in the range Z.

In the case of massive bottom quark and massive charm quark loop insertions, the results are given by the fitting formulae,

$$\begin{aligned} \mathrm{Re}\langle s\gamma|Q_2|b\rangle_{n_f}^{(2),m_b} &= -1.836 + 2.608\,z + 0.8271\,z^2 - 2.441\,z\,\ln z \\ &+ (-9.595 + 5.157\,z + 1.726\,z^2 - 16.18\,z\,\ln z)\ln(m_b/\mu) \\ &+ \frac{800}{243}\ln^2(m_b/\mu), \end{aligned} \tag{3.7}$$

$$\begin{aligned} \mathrm{Re}\langle s\gamma|Q_2|b\rangle_{n_f}^{(2),m_c} &= 9.099 + 13.20\,z - 19.68\,z^2 + 25.71\,z\,\ln z \\ &+ (-9.679 + 13.62\,z - 13.94\,z^2 - 12.98\,z\,\ln z)\ln(m_b/\mu) \\ &+ \frac{800}{243}\ln^2(m_b/\mu). \end{aligned} \tag{3.8}$$

again with 10^{-4} relative precision compared to the data points. The numerical results and fits are plotted in fig. 3.4.

For completeness, we also give the first two terms of the matrix elements in the limit $m_b^2 \gg m_c^2$, which are obtained with help of MB representations. While we completely

agree with the massless result of [98], for the two massive cases we find, setting $\mu = m_b$:

$$\begin{aligned}\langle s\gamma|Q_2|b\rangle_{n_f}^{(2),m_b} &= 4.25648 + 0.503085\ \ln z + 0.888889\ \ln^2 z \\ &+ \frac{1}{z}\left(-0.725053 - 1.80916\ \ln z + 0.0938272\ \ln^2 z\right) \\ &+ \frac{1}{z^2}\left(-1.39486 - 0.968501\ \ln z - 0.147443\ \ln^2 z\right) + \mathcal{O}\left(\frac{1}{z^3}\right),\end{aligned} \tag{3.9}$$

$$\begin{aligned}\langle s\gamma|Q_2|b\rangle_{n_f}^{(2),m_c} &= 1.67932 + 0.526749\ \ln z + 0.823045\ \ln^2 z \\ &+ \frac{1}{z}\left(0.20839 + 0.11775\ \ln z + 0.128395\ \ln^2 z\right) \\ &+ \frac{1}{z^2}\left(-0.0360638 - 0.0470166\ \ln z + 0.0324515\ \ln^2 z\right) + \mathcal{O}\left(\frac{1}{z^3}\right).\end{aligned} \tag{3.10}$$

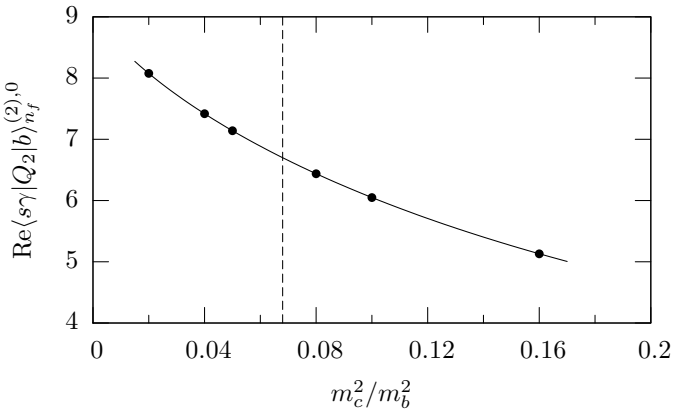

Figure 3.3.: Plot of $\mathrm{Re}\langle s\gamma|Q_2|b\rangle_{n_f}^{(2),0}$ for one massless flavor and $\mu_b = m_b$. The dashed vertical line corresponds to the central value $m_c^2/m_b^2 = 0.068$.

As a last result, here we also plot the renormalization scale dependence μ_b in fig. 3.5 for the fermionic NNLO corrections to the P_2 matrix elements compared to the NLO contribution in two different values of z. μ_b is varied between $m_b^{1S}/2$ and $2m_b^{1S}$. Depending on the scale, we find the massive contribution to be in the several per cent range for $\mu_b \sim m_b$ but ranges up to 40% on the low energy end at $\mu_b = 2.5$ GeV. It has to be noted, however, that these results are strongly dependent on the input in the running of $\alpha_s(\mu)$. Here we have used the renormalization group with five active flavours and the β-function up to three loop accuracy, computed with `RunDec` [126]. Currently, the correct choice of the number of flavours and the loop precision of the running is rather controversial in the context of $\overline{B} \to X_s\gamma$ decays and therefore a further discussion is beyond the scope of this work.

Apart from consistency requirements during the evaluation of master integrals, the resulting matrix elements have to fulfill certain requirements. Firstly, the fermionic corrections form a gauge invariant subset of the full matrix elements and therefore renormalize independently of bosonic corrections. Secondly, the amplitude has to be infrared finite

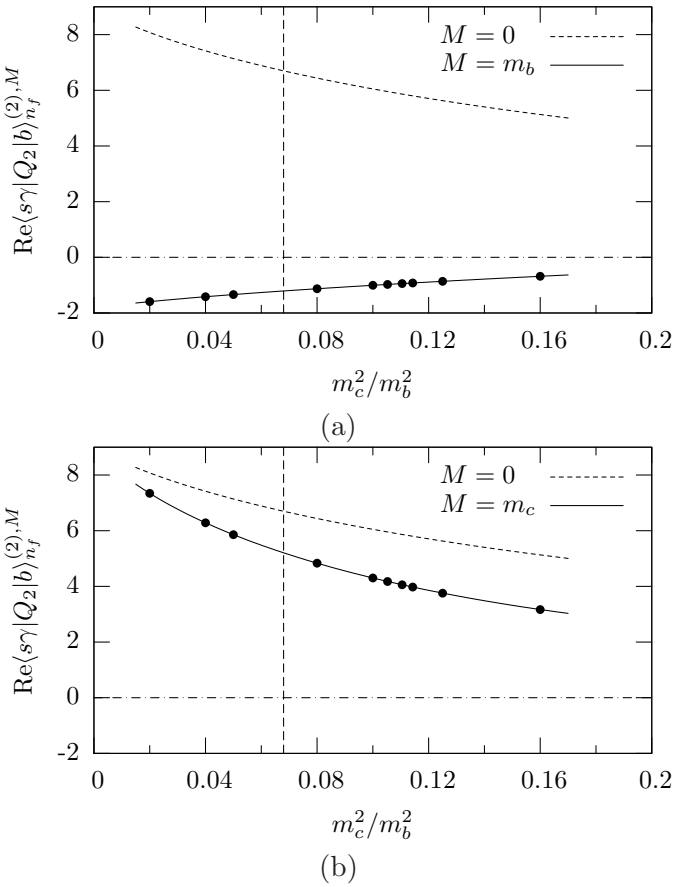

Figure 3.4.: Plots of $\mathrm{Re}\langle s\gamma|Q_2|b\rangle_{n_f}^{(2),M}$ as function of m_c^2/m_b^2 with $M = m_b$ (a) and $M = m_c$ (b) and $\mu_b = m_b$. For comparison, we also show the $M = 0$ case.

as was shown in the massless case. Taking non-vanishing quark masses into account, the infrared behaviour is not affected. Both criteria are clearly satisfied. Moreover, the contribution of massive charm quark loop insertions should coincide with massless insertions for small z. Although the method employed here doesn't allow for a direct evaluation at $z = 0$, the trend can be seen in fig 3.4. As a last cross check, the μ-dependent parts in the matrix elements can also be obtained from renormalization group equations. In the case of massless loop insertions the exact expression for the coefficient of $\log(m_b/\mu)$ is

$$\frac{8}{3}\left(\Re(a(z) + b(z)) - \frac{290}{81}\right) \tag{3.11}$$

where $a(z)$ and $b(z)$ are known from the NLO calculation and are given explicitly in chapter 2.2.2.
For eqn. (3.10) the renormalization group equations lead for the same coefficient to

$$\frac{8}{3}\left(\Re(a(z) + b(z) + b(1)) - \frac{290}{81}\right) \tag{3.12}$$

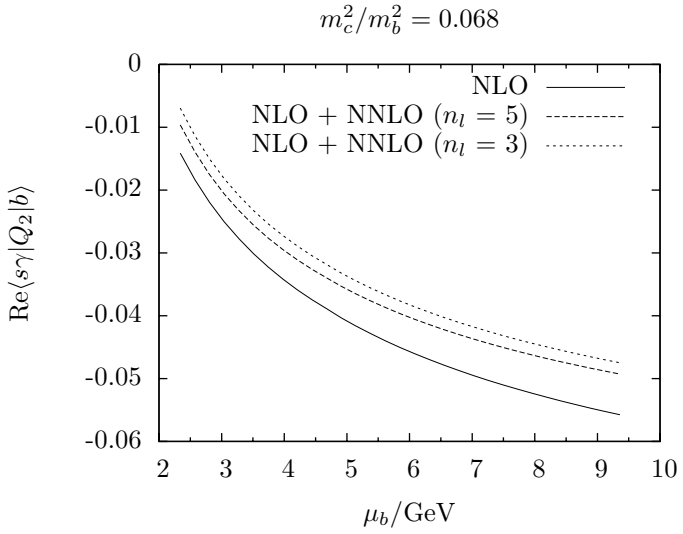

Figure 3.5.: Renormalization scale dependence of the complete NNLO fermionic corrections to the matrix element $\langle s\gamma|Q_2|b\rangle$. The case $n_l = 5$ corresponds to purely massless corrections while $n_l = 3$ takes the charm and bottom quark masses into account.

and similarly for eqn. (3.10)

$$\frac{8}{3}\left(\Re(a(z) + 2b(z)) - \frac{290}{81}\right). \tag{3.13}$$

Our results fully reproduce these coefficients.

3.1.4. Discussion

As far as the evaluation of fermionic contributions stemming form massless loop insertions is concerned, the work presented here is the first verification of the findings of [98]. While this is already an important result as itself, it also proves the applicability of the methods and approaches, that were developed in the course of this work.
Taking mass effects into account for the first time, we find moderate and sizeable deviations from the massless approximation for charm quark and bottom quark loop insertions, respectively. For the current NNLO branching ratio estimate of $\overline{B} \to X_s\gamma$ it is assumed, that charm and bottom quark insertions are well approximated by massless quarks. While this assumption is still more or less justified in the charm quark case, it is strongly violated for heavy bottom quarks. In fact, the absolute contribution from heavy bottom quarks is close to vanishing and neglecting the mass overestimates the true contribution by a factor of six. Indeed, this result points to a decoupling-like effect for the bottom quark, which can be understood as the relevant scale for the decay rate is given by m_b. Hence, using the massless approximation, a four-quark flavour scheme is more appropriate. Altogether, the mass-induced impact on the branching ratio is not sizeable, since it appears in only one flavour, but is still noticeable. In an estimate

[104], the approximate effect of the mass inclusions to the branching ratio amounts to about +1.6%. It has to be noted, that although this correction is in nice agreement with the extrapolation uncertainty as discussed in chapter 2.2.2, the yet missing bosonic contribution can change matters in any direction.

3.2. Interference of P_2 and P_7 at $m_c = 0$

One of the main sources of uncertainty in the current NNLO branching ratio estimate of the $\overline{B} \to X_s\gamma$ decay given by eqn. (2.42) originates from the only approximate knowledge of bosonic corrections to the matrix elements at this level of accuracy. Here we focus on the reduction of this uncertainty through the evaluation of the missing bosonic parts in the limit of vanishing charm quark mass. Even in this limit, no complete evaluation for this quantity is known to date, although they constitute an important input to fix the endpoint of the employed charm quark mass extrapolation (compare chapter 2.2.2). Providing these results, the extrapolation induced error in the physical quark mass ratio can be largely decreased and hence the residual uncertainty would be dominated by the chosen functional dependence in the intermediate region.
The most important contribution in this context stems from charm quark mass dependent matrix elements, i.e. the interference G_{27} of the four-quark operator P_2 and P_7. This is, again, both due to the sizeable Wilson coefficients of this operator and its explicit charm quark dependence.
In the case where the charm quark is treated as massless, the only particle with a non-zero mass is the bottom quark, which appears both in internal propagators and as an external field, which is kept on-shell. Therefore, as the majority of lines is of zero mass in each diagram, purely virtual NNLO corrections to the matrix elements in this limit are expected to be infrared divergent. As usual, these divergences have to cancel with real soft radiation at the same level of perturbation theory and therefore real corrections are mandatory to obtain physically meaningful results. The standard approach in this respect consists in separate computations of virtual and real parts at the amplitude level. Only the final interference of the amplitudes and the evaluation of phase-space integrals yields an observable like a cross section or decay rate that is infrared safe. Here, however, we follow a different strategy that is based on the well-known optical theorem and Cutkosky's rules. Thereby, real and virtual corrections are treated at the same level. In the following, we focus on the evaluation of contributions stemming from two and three particle intermediate states in G_{27} at NNLO, present the basic approach to the evaluation and discuss the found results.

3.2.1. Prerequisites

At NNLO in the strong coupling and leading order in both the Fermi constant and the electromagnetic coupling, the quantity we are interested in is the interference of P_2 with the dipole operator P_7, and reads

$$\begin{aligned} G_{2,7}^{NNLO} &= \sum_n \int d\Pi_n \left(\langle b|P_7|n\rangle\right)^* \langle n|P_2|b\rangle = \sum_n \int d\Pi_n M_7^* M_2 \\ &= \sum_n \int d\Pi_n \left[\left(M_7^{\mathrm{NNLO}}\right)^* M_2^{\mathrm{LO}} + \left(M_7^{\mathrm{NLO}}\right)^* M_2^{\mathrm{NLO}} + \left(M_7^{\mathrm{LO}}\right)^* M_2^{\mathrm{NNLO}}\right] \end{aligned} \tag{3.14}$$

where the sum runs over all states $|n\rangle$ that contain at least one photon and one strange

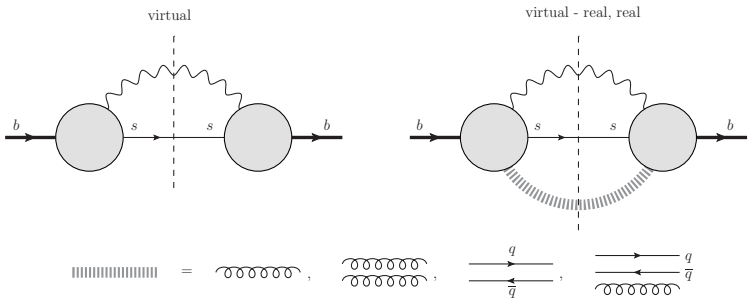

Figure 3.6.: Diagrammatic representation of eqn. (3.14), for purely virtual, virtual-real and purely real contributions to the operator interference. The vertical dashed line represents the cut, while the thick grey line stands for possible propagator insertions to generate the states in (3.15).

.

quark and $d\Pi_n$ is the infinitesimal element of the corresponding n-particle phase-space. The states $|n\rangle$ contributing to the $\overline{B} \to X_s\gamma$ decay are at this order of perturbation theory are

$$|s\,\gamma\rangle,\ |g\,s\,\gamma\rangle,\ |g\,g\,s\,\gamma\rangle,\ |q\,\overline{q}\,s\,\gamma\rangle \text{ and } |g\,q\,\overline{q}\,s\,\gamma\rangle, \tag{3.15}$$

where q denotes the light quarks u,d,s and c. To ensure the full cancellation of infrared divergences, it is important to take states including $c\overline{c}$ into account, as the charm quark is now treated massless and contributes in the soft radiation. Experimentally, however, these states are excluded from the measurement of the $\overline{B} \to X_s\gamma$ decay by imposing certain cuts. Hence, in a full analysis of the branching ratio, a subtraction of these parts is needed [103].
G_{17}^{NNLO} can be represented diagrammatically as shown in fig. 3.6. The vertical dashed lines indicate cuts, i.e. all particles that are crossed by this line are assumed to be on the mass shell and an integration over their phase space is implied. Examples of diagrams appearing in our calculation are shown in fig. 3.7 .
The renormalization can directly be derived from the prescription in chapter 2.1.2, where two operators have to be taken into account. The generating formula for the renormalized interference reads

$$\begin{aligned}(\langle P_7\rangle^*\,\langle P_2\rangle)^R \;=\;& Z_\psi^2\,[Z_m\,Z_{77}\langle P_7\rangle^*] \\ & \times\left[Z_\psi\left(\sum_{k=1}^{6} Z_{2k}\langle P_k\rangle + \sum_{k=25}^{32} Z_{2k}^E\langle P_k\rangle\right)\right. \\ & \left. + Z_m(Z_{27}\langle P_7\rangle + Z_g\sqrt{Z_G}Z_{28}\langle P_8\rangle)\right]\end{aligned} \tag{3.16}$$

where the integration over the corresponding n-particle phase spaces is understood. Moreover, we have already taken into account, that P_7 only mixes with itself, while the four-quark operators receive Counterterm contributions from various physical and evanescent operators.

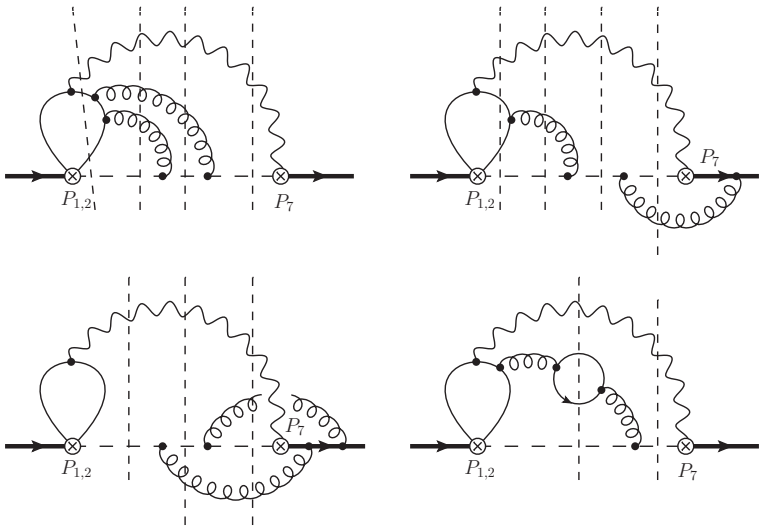

Figure 3.7.: Example diagrams for the interference of P_2 and P_7 at NNLO. Thick lines represent bottom quark propagators, thin lines charm quark propagators and dashed ones strange quark propagators. The vertical dashed lines indicate cuts. In the first diagram, not all possible 5-particle cuts are shown.

Expanding eqn. (3.16) in the strong coupling leads to a large expression, so we refrain from quoting it here explicitly. Let us just mention the separate contributions generated by physical operators needed for the renormalization. The relevant operator combinations lead to diagrams of up to two loops in the matrix elements $\langle P_k \rangle$ of eqn. (3.16) and are summarized in tab. 3.2. Example diagrams at the highest needed order in perturbation theory are depicted in fig. 3.8.

Interference	max. loop order
$P_7\, P_7$	2 loops / $\mathcal{O}(\alpha_s^1)$
$P_8\, P_7$	2 loops / $\mathcal{O}(\alpha_s^1)$
$P_k\, P_7$	3 loops / $\mathcal{O}(\alpha_s^1)$

Table 3.2.: Needed interference diagrams for renormalization, where $k = 1, \ldots, 6, 25, \ldots, 32$. The loop levels and orders of α_s before multiplication with renormalization constants are also given.

3.2.2. Computation

As shown by Cutkosky [127] in his study of analytical properties of Feynman integrals, the on-shell condition of internal particles can also be enforced by the replacement

$$2\pi i \delta(q^2 - m^2) \to \frac{1}{q^2 - m^2 + i\epsilon} - \frac{1}{q^2 - m^2 - i\epsilon}. \tag{3.17}$$

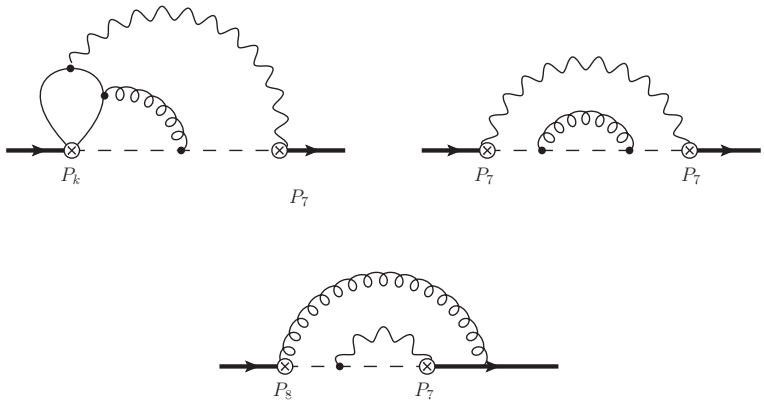

Figure 3.8.: Example diagrams with the highest loop level needed for each operator combination required in the renormalization of the NNLO interference of P_2 and P_7.

Applying this relation to the diagrammatic representation of fig. 3.6 is equivalent to a forward scattering amplitude computation. As a result, the interference of matrix elements is converted into multi-loop integrals with a modified prescription for cut propagators. The huge benefit of this idea lies in the fact, that the resulting multi-loop diagrams can be treated with standard methods like the IBP reduction or the method of differential equations.

Concerning the reduction to master integrals, a slight modification of the applied method is necessary to handle cut integrals. In the standard form (that is explained in more detail in appendix A) scalar products of external and internal momenta in the numerator of the resulting IBP relations are completed to quadratic forms and all possible cancellations with the integral's propagators are performed. All resulting sub-integrals are retained in the reduction. Here, however, we discard those children that do not possess the same number of cut propagators as the original integral after elimination. As can easily be seen from eqn. (3.17), these integrals do not contribute to the desired phase-space and intermediate n-particle state. This fact can also be understood from a different perspective. Let's assume for now, that we are dealing with standard higher order integrals with one external leg. The relations between Feynman diagrams, that stem from their hypergeometric structure, ensure the relations to be valid both in the real and imaginary part. In fact, the optical theorem relates the imaginary part of the full forward-scattering amplitude to the cross-section of the external particle decaying into all theoretically allowed states at a given order of perturbation theory. If we are, however, interested in only one or several particular decay channels, the irrelevant contributions have to be subtracted from this quantity. Discarding diagrams in the IBP reduction is similar to this subtraction. Another detail is the non-standard prescription for the infinitesimal imaginary shift in the propagators. On the one hand, this does not affect the differentiation in the IBP relations. On the other hand, however, this would require two different types of propagators, differing in the used analytical continuation. Fortunately,

one is only interested in the real part of the interference. So, neglecting the second term on the right hand side of eqn. 3.17 has an effect on the imaginary part of cut integrals only.
In this work, the basic objects in the computation of the interference (3.14) are four-loop Feynman diagrams containing cuts in the sense of the right hand side of (3.17). In short we refer to them as cut diagrams with a given number of cuts, indicating the intermediate states $|n\rangle$. All Feynman diagrams required for the interference of the P_2 operators with P_7 are generated with help of the package `DiaGen` [123]. The efficient implementation of graph-theoretical algorithms for the topological analysis and treatment of Feynman diagrams in this software was used to implement a generator of arbitrary propagator-type multi-loop integrals containing cuts. At the center of this approach lies the identification of the correct fields in the cut, the validity of the resulting subparts left and right of the cut and finally the generation of scalar multiloop integrals for the integration-by-parts reduction with `IdSolver` [128].
Altogether, 1256 four-loop on-shell Feynman diagrams are generated resulting in 185 master integrals after performing the IBP reduction. Since the $\overline{B} \to X_s\gamma$ decay rate is an inclusive observable, we sum over all color and spin states of the external particles. More specifically, as I_P is equal to a fermion propagator, the spin summation is equivalent to a simple projection. Expressing I_P through the amputated NNLO contributions Π, the projector P_s is derived from

$$I_P = \sum_s \overline{u}_b \Pi u_b = \mathrm{tr}\left(\Pi \sum_s \overline{u}_b u_b\right) = \mathrm{tr}\left(\Pi \frac{\not{p}_b + m_b}{2m_b}\right) = P_s \Pi \tag{3.18}$$

where the sum runs over all spins s and p_b and m_b are the momentum and mass of the bottom quark, respectively. In the subsequent step, the Dirac algebra is performed and one ends up with a linear combination of scalar cut four-loop integrals multiplied with color factors and couplings.
The final step in the computation consists in the evaluation of the master integrals. Here we follow two different strategies. Purely massless diagrams are evaluated using a Mellin Barnes motivated approach and for integrals containing massive bottom lines the method of differential equations as described in the appendix is utilized. While the external bottom quark is kept on-shell in the IBP reduction of integrals needed for the interference to reduce the computation time, the evaluation of massive master integrals with the help of differential equations requires an off-shell external momentum, which implies a separate IBP reduction for the masters only. Tab. 3.3 gives an overview over the number of generated diagrams, scalar integrals and master integrals both for the on-shell and off-shell cases, for each number of particles in the cut separately.
The discussion concerning the evaluation of massive propagator-type integrals in appendix B is equally applicable to cut diagrams. This is due to the fact that the scaling property leading to differential equations in the standard case is not altered. Moreover, as all particles in the cuts are massless, derivatives in the mass do not lead to any problems. The full computation follows the program presented in appendix B. Boundary integrals are products of massive tadpoles and massless cut propagators. While the

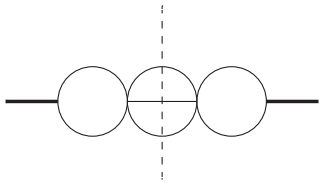

Figure 3.9.: Massless master integral obtained from the imaginary part of a massless propagator-type integral.

former are known in literature, the latter are determined with the technique described below. Appendix C lists explicit expressions for the required input. For the continuation of the off-shell integrals to the threshold, in addition to the large mass expansion a threshold expansion and matching with the numerical integration is needed, as the differential equations are, in general, singular in the on-shell point. About 10% of the masters are logarithmically divergent in $p_b^2 = m_b^2$ and have to be regularized prior to the evaluation.

Massless master and boundary integrals are treated differently. Some cases like the one depicted in fig. 3.9 can be directly determined from the imaginary part of known massless propagators. For more complicated cases the integrals are transformed to Mellin Barnes representations and the resulting loop and phase space integrations are carried out explicitly in a numerical form. As most of the here required masters can be determined in a rather automatized way with existing packages , the approach is discussed only briefly in the following.

In a first step, all loop propagators are replaced by the Mellin Barnes transformation using the package `MBrepresentation` [129]

$$\frac{1}{(q^2-m^2)^n} = -\frac{i}{2\pi}\int_{\beta-i\infty}^{\beta+i\infty} dz \left(\frac{m^2}{q^{2n}}\right)^z \frac{\Gamma(n+z)\Gamma(-z)}{\Gamma(n)} \tag{3.19}$$

where q is a sum of external and loop momenta. The resulting structure for a l-loop propagator type integral, $I_{p^2,l,n,c}$, with external momentum p, n propagators with momenta q_i and c massless cut propagators with momenta r_i reads

$$I_{p^2,l,n,c} \sim \prod_{i=1}^{l} d^d k_i \prod_{j=1}^{n} \int_{\beta_j-i\infty}^{\beta_j+i\infty} dz_j \prod_{k=1}^{c} \delta(r_k^2) F(q_1,\ldots,q_p,z_1,...,z_p). \tag{3.20}$$

The quantity $F(q_1,\ldots,q_p,z_1,...,z_p)$ is a product of momenta and masses, raised to some powers proportional to the z_i and propagator exponents, and Γ-functions. After shifting the momenta r_i^μ, such that they are composed of p^μ and a set of $c-1$ loop momenta $k_c = \{k_{i_1}^\mu,...,k_{i_{c-1}}^\mu\}$, the loop integrations in k_c can be performed, effectively carrying out the c-particle phase space integration. The remaining evaluation in the z_is, which consists of a proper analytical continuation of the integrand, thereby determining valid values of β_i, and the final numerical integration parallel to the imaginary axis is done with help of `MB` [124].

	n_D	n_M^{OS}	n_M^{contd}
2-particle cuts	292	98	144
3-particle cuts	306	63	113
4-particle cuts	418	24	
5-particle cuts	240	21	

Table 3.3.: Number of diagrams n_D, number of on-shell master integrals n_M^{OS} and number of continued, effectively computed master integrals n_M^{contd}.

In the context of this thesis the interference of the P_2 and P_7 operator including two- and three-particle cuts was evaluated. Various cross-checks at different steps of the computations assure the correctness of the obtained results. All NLO matrix elements contributing to the renormalization were compared and verified with the existing literature, where possible [88]. Consistency checks as described in appendix A ensure the numerical correctness in the evaluation of master integrals. Some relatively simple massive masters that are feasible with Mellin Barnes representations at least in the asymptotic limit of large masses, were independently checked in addition with this method. Apart from the cut integral method, all massive two-particle cut masters were also obtained with the well-tested method utilized in the preceding chapter. For this task, the two-particle cut integrals were represented as massive vertices and differential equations were derived in the mass only. Multiplying the resulting expressions with the massless two-particle phase space, the cut diagrams can be obtained. Moreover, these results can be used to evaluate the full P_2 matrix elements at the amplitude level in the limit of vanishing charm quark masses and opens the possibility to confront them with the known fermionic corrections [98].

3.2.3. Results

In the following we present the results for the matrix elements of the P_2 operators and their respective interferences up to three particles in the final state for vanishing charm quark mass.

The purely virtual NNLO corrections to the renormalized matrix elements in this limit

read

$$\begin{aligned}\langle s\gamma|Q_2|b\rangle^{(2)}_{m_c=0} &= \frac{1}{\epsilon^2}(0.08922333 - 0.05709100\,i) + \frac{1}{\epsilon}(1.504833 + 0.9689700\,i) \\ &\quad (-38.78967 + 18.15080\,i) + (9.029121 + 5.8138211\,i)\,\ln\left(\frac{m_b}{\mu}\right) \\ &\quad +(1.606020 - 1.0276382\,i)\,\ln^2\left(\frac{m_b}{\mu}\right) \\ &\quad +n_l\left[(8.602274 + 8.532721\,i) - (9.547325 + 4.550784\,i)\,\ln\left(\frac{m_b}{\mu}\right)\right. \\ &\quad \left.+3.292181\,\ln\left(\frac{m_b}{\mu}\right)^2\right] \qquad (3.21)\end{aligned}$$

where $d = 4-2\epsilon$ and the amplitude is defined as in eqn. (3.5). The fermionic contribution that is proportional to n_l is in full agreement with the results of the previous chapter. The remaining poles in the limit $\epsilon \to 0$ stem from bosonic corrections, are of infrared origin and have to cancel with real radiation.
The renormalized interference of P_2 with the dipole operator P_7 in the limit of a massless charm quark is given by

$$\begin{aligned}\frac{\mathrm{Re}\,G^{(2),2P}_{27,m_c=0}}{\Pi_2} &= \frac{1}{\epsilon^2}\,0.08922333 + \frac{1}{\epsilon}\,1.003222 - 46.82248 - 27.68839\,\ln\left(\frac{m_b}{\mu}\right) \\ &\quad +6.732510\,\ln^2\left(\frac{m_b}{\mu}\right) \\ &\quad +n_l\left[8.602274 - 9.547325\,\ln\left(\frac{m_b}{\mu}\right) + 3.292181\,\ln\left(\frac{m_b}{\mu}\right)^2\right] \qquad (3.22)\end{aligned}$$

$$\frac{\mathrm{Re}\,G^{(2),3P}_{27,m_c=0}}{\Pi_3} = -\frac{1}{\epsilon^2}\,0.08922333 - \frac{1}{\epsilon}\,2.575527 + 20.80984. \qquad (3.23)$$

Here, the result is split into two and three particles in the final state and normalized to the corresponding phase space. The separate contributions are denoted by the superscripts $2P$ and $3P$.
Finally, for the sum of the two and three particle cut interferences of P_2 with P_7 we obtain

$$\begin{aligned}\mathrm{Re}\,G^{(2),2P+3P}_{27,m_c=0} &= -\frac{1}{\epsilon}\,5.877315 - 122.0772 - 86.98529\,\ln\left(\frac{m_b}{\mu}\right) + 21.15080\,\ln^2\left(\frac{m_b}{\mu}\right) \\ &\quad +n_l\left[27.02484 + 14.99690\,\ln\left(\frac{m_b}{\mu}\right) + 2.585673\,\ln^2\left(\frac{m_b}{\mu}\right)\right]. \qquad (3.24)\end{aligned}$$

As can be seen from this result, the infrared pole proportional to ϵ^{-2} cancels in the sum.

Part II.

Applied techniques

4. Integration-by-parts Identities

A crucial part in any computation of higher order corrections in quantum field theories is the evaluation of the resulting multi-loop scalar integrals. A Feynman integral of l loops with loop momenta k_i, $i \in \{1, \ldots, l\}$, n_e external vertices with external momenta p_i, $i \in \{1, \ldots, n_e - 1\}$ and n_i internal propagators with momenta q_i and mass m_i, $i \in \{1, \ldots, n_i\}$ takes in $d = 4 - 2\epsilon$ dimensions the general form

$$\int \prod_{k=n}^{l} \frac{d^d k_n}{\pi^{d/2}} \frac{\prod_{i \geq j, j=1}^{l} (k_i\, k_j)^{\nu_{i,j}^{kk}} \prod_{i=1}^{l} \prod_{j=1}^{n_e - 1} (k_i p_j)^{\nu_{i,j}^{kp}}}{\prod_{i=1}^{n_i} (q_i^2 - m_i^2)^{\delta_i}}, . \tag{4.1}$$

$\{\delta_i\}$ and $\{\nu_{ij}^{kk}\}, \{\nu_{ij}^{kp}\}$ are the number of propagators and scalar products in the numerator, respectively. A priori, the numerator is composed of all possible scalar products of external and loop momenta. However, completing the products $p_i k_j$ to propagators with the appropriate mass, one can cancel denominators. Using this procedure successively, one ends up with a smaller set of scalar products in the numerator that cannot be further reduced.

As the number of loops, external legs and involved scales increases, one is confronted with an exponentially growing number of integrals, reaching up to hundreds of thousands within the calculations performed in this work. Obviously, a direct integral by integral evaluation of this amount is not feasible.

Within dimensional regularization, however, it is possible to obtain relations between Feynman integrals using integration-by-parts (IBP) identities. This idea is based on the assumption that Feynman integrals are well defined in d dimensions and hence surface terms in integration by parts identities

$$\int \prod_{l=1}^{n} d^d k \, \frac{\partial}{\partial k_i^\mu} k_j^\mu V = 0 \tag{4.2}$$

vanish.

Taking the derivative in (4.2) explicitly, multiplying by loop momenta and internal momenta and using the basic algebraic relations described above to cancel denominators in the integrand V, it turns out that the relation will lead to a linear combination of the original integrand and integrands with propagators missing from V. In other words, the IBP relations connect a given topology, e.g. the ordered graph representing the Feynman integral with propagators raised to different powers and numerators consisting of scalar products of momenta, to itself and topologies with a reduced number of propagators.

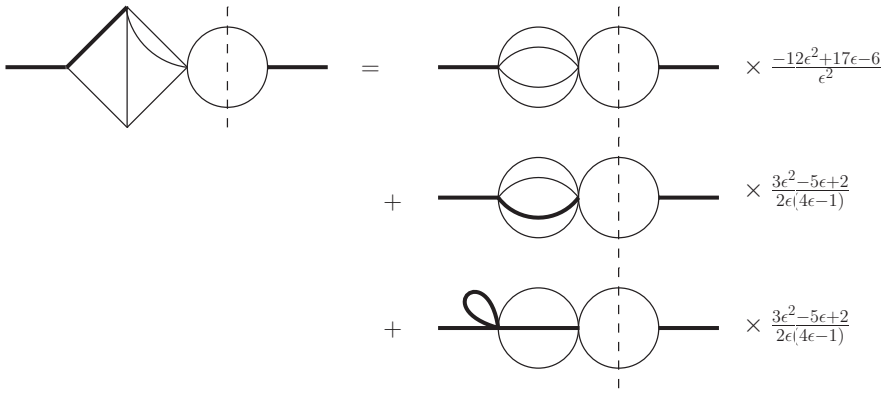

Figure 4.1.: Example for an IBP reduction of a cut propagator.

A recursive application of the resulting relations allows to express any Feynman integral $I(\epsilon, \{p_i^2\}, \{m_i^2\})$ in terms of a set $\{M_i\}$ of so-called master integrals (MI),

$$I(\epsilon, \{p_i^2\}, \{m_i^2\}) = \sum c_i(\epsilon, \{p_i^2\}, \{m_i^2\})\ M_i(\epsilon, \{p_i^2\}, \{m_i^2\}) \tag{4.3}$$

Since the derivative is applied to Feynman integrals containing only polynomials in the momenta, the coefficients $c_i(\epsilon, \{p_i^2\}, \{m_i^2\})$ are rational functions in ϵ and the kinematical invariants.

As an example consider the IBP reduction of the integral depicted in fig. 4.1.

To reduce a large number of integrals effectively, a powerful algorithmic approach was developed by Laporta [55]. It has the large benefit compared to previous works, that by applying a specific ordering and carefully choosing the integrals to be input in eqn. (4.2), a minimal set of master integrals can be automatically determined. In general, this number of yet to be computed MIs is (much) smaller than the initial number of unknowns, thereby reducing the problem of actually computing the integrals.

It has to be noted, that the choice of master integrals is not unique and can be altered by use of the IBP equations. Typically, this is done to obtain an epsilon finite basis [130], which is free of so-called spurious poles. These removable poles manifest themselves as ϵ^{-n} terms in the coefficients c_i of the IBP reduction and are transferred into the higher order amplitude or cross-section. Requiring the amplitude to be valid up to a certain order $\mathcal{O}(\epsilon^k)$, the master integrals have to be provided to even higher powers in ϵ to compensate for the divergences in c_i. Here, we do not apply the algorithm of [130] to get rid of spurious poles, which leads to master integrals having both propagators of non-unity powers and irreducible scalar products. Instead, we require all master integrals to have propagators raised to power one $\delta_i = 1$ in eqn. (4.2) for all i and arbitrary scalar products in the numerator. The basis is changed only in the case of logarithmic divergences in the interesting kinematical region (see chapter 5.3) which introduces additional factors in the numerators only.

Throughout this work, the software package `IdSolver` [128], an efficient application and extension of Laporta's algorithm, was used to perform all the needed IBP reductions.

5. Evaluation of master integrals

In general, providing closed analytical expression for master integrals is difficult or even impossible but for the simplest cases. Only for the massless and the single-scale case a basis of functions is known to date, which is moreover limited to certain threshold structures.
Fortunately, a powerful technique for massive integrals exists that can be used to obtain at least high-precision expansions around certain kinematical limits and exact numerical evaluations in the whole parameter space. The basic idea is to exploit differential equations in kinematical invariants and masses of the integrals in question. The advantage of this approach is that it is fully automated and therefore allows for the computation of a large number of MIs at once. Moreover, the input consists of only a small set of boundary integrals (BI) that can be derived from the MIs.
In the following, the technique of differential equations for MIs, its automatization and the determination of BIs is discussed.

5.1. Differential equations for master integrals

5.1.1. Basics

Let $\mathbf{M} = (\mathbf{I}_{n_1}, \mathbf{I}_{n_2}, \dots)$ with $n_i < n_{i+1}$ be an vector composed of sets $\mathbf{I}_n(\{m_i\}, \{p_i\})$ of scalar master integrals with n internal propagators depending on the external momenta p_i and the internal masses m_i. Application of a differential operator $\mathcal{D}(\partial/\partial p_i^\mu, \partial/\partial m_i)$ on $\mathbf{M}$ leads to integrals that can again be reexpressed with the help of the IBP reduction such that one obtains a system of coupled differential equations

$$\mathcal{D}\mathbf{M} = \hat{A}\mathbf{M}, \quad \text{with} \quad \hat{A} = a_{ij} \quad \text{block-triangular.} \tag{5.1}$$

Due to the ordering of IBP relations in the Laporta algorithm, the Jacobian $\hat{A}$ is block-triangular. Moreover, coupled differential equations only appear within the same topology. Hence, the general form of a system of differential equations for k master integrals belonging to the same topology $\mathbf{T}_n^i = (I_n^{i,1}, \dots, I_n^{i,k})$ with n internal lines reads

$$\mathcal{D}\mathbf{T}_n^i = \hat{B}\mathbf{T}_n^i + \mathbf{L}_n^i \tag{5.2}$$

where the inhomogeneity $\mathbf{L}$ is a vector of integrals not belonging to the topology T_n^i with $n-1$ propagators or less.
In the scope of this work, all massive master integrals can be obtained from differential equations in a single variable z. Altogether, three different kinds of integrals appear:

- on-shell integrals $I_{\text{on}}(m_l^2, m_h^2)$ with massless, light (mass m_l) and heavy (mass m_h) internal propagators and external momenta $p_i^2 = \{0, \ldots, 0, m_h^2\}$. These integrals can be described through the variable $z = m_h^2/m_l^2$.
- off-shell propagator-type integrals $I_{\text{off}}(p^2, m^2)$ with massless and massive (m) internal lines. These integrals may contain cuts through only massless propagators. In this case, $z = p^2/m^2$.
- partially off-shell vertex integrals, with external momenta $p_i^2 = \{0, 0, p^2\}$ and internal massless and massive (mass m) lines. In this case again, $z = p^2/m^2$, and we therefore refer to them as $I_{\text{off}}(p^2, m^2)$, too.

The differential operators used in these cases read

$$\mathcal{D}_{\text{on}} I_{\text{on}} = m_l^2 \frac{\partial}{\partial m_l^2} I_{\text{on}} \tag{5.3}$$

$$\mathcal{D}_{\text{off}} I_{\text{off}} = d_I I_{\text{off}} - m^2 \frac{\partial}{\partial m^2} I_{\text{off}} \tag{5.4}$$

where, using the definitions in eqn. (4.1),

$$d_I = l\,\frac{d}{2} + \sum_{i=1}^{l} \left(\sum_{j=1}^{l} \nu_{ij}^{kk} + \sum_{j=1}^{n_e-1} \nu_{ij}^{pk} \right) - \sum_{i=1}^{l} \delta_i \tag{5.5}$$

is the mass dimension of the integral in question. $\mathcal{D}_{\text{off}}$ can easily be obtained from the invariance of I_{off} under the scaling $(m^2, p^2) \to (\lambda m^2, \lambda p^2)$.
The action of the derivative $\partial/\partial m^2$ increments the power of massive propagators by one

$$m^2 \frac{\partial}{\partial m^2} \frac{1}{(q_i^2 - m^2)^{\delta_i}} = -\frac{m^2\,\delta_i}{(q_i^2 - m^2)^{\delta_i+1}} \tag{5.6}$$

Using the IBP relations on the right hand side leads to the desired differential equation. Since all cut lines are massless in our case, this operator is also applicable on $I_{\text{off}}^{\text{cut}}$.
After applying the differential operators and reexpressing the appearing integrals in terms of master integrals, one makes the ansatz

$$I_n = \sum_{k=-2l}^{N_n} I_{n,k} \epsilon^k. \tag{5.7}$$

The upper limit N_n has to be chosen carefully, since, as already discussed, spurious poles in ϵ are generated in the IBP reduction. On the one hand, these poles show up in the computed amplitude and analyzing its coefficient structure leads to a set $\{N_n^{ampl}\}$ of powers of ϵ necessary for each master integral I_n. On the other hand, spurious poles also occur in the differential equations and thus require ansätze with even higher orders in ϵ. These powers have to be obtained recursively from the generated differential equations

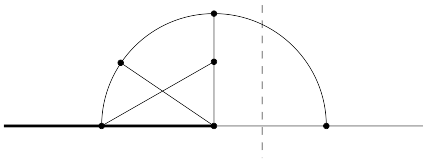

Figure 5.1.: Example master integral occurring in the computation of the interference of the O_2 and O_7 operators of the $b \to s\gamma$ decay at NNLO. Thin lines denote massless, thick lines massive propagators. The cut is indicated by the dashed line.

in the order the system is to be solved and are required to fulfill at least $\{N_n^{ampl}\}$ for each I_n. After applying (5.7), the system of differential equations is generated order by order in ϵ.
In principle, provided that boundary conditions are known in some kinematical point, $z = z_0$, the system of differential equations is directly solvable numerically with standard methods. Differential equations of Feynman integrals, however, in general possess singular points, i.e. submatrices of the Jacobian $\hat{A}$ are singular at specific values of z. This comes as no surprise since the MIs can indeed have removable or true singularities stemming from pseudo thresholds and thresholds, respectively. In most cases this problem can be circumvented by contour deformation (see section 5.1.3), but can not be avoided if the start or end point of numerical integration coincides with a singular point. Therefore, obtaining the master integrals in an arbitrary z is in general more complicated and requires a four step approach:

1. **Boundary integrals**
   The master integrals are evaluated at a value of kinematical invariants, which is accessible by a different technique. This fixes the starting point input at $z = z_0$ for the system of differential equations. In this work, mostly diagrammatic large-mass expansions have been performed that provide the first few terms of the integrals in the limit $p^2/m^2 \to 0$ or $m_h^2/m_l^2 \to 0$. Further details are given in section 5.2.

2. **High order asymptotic expansion**
   The system of differential equations is solved in the limit of large masses with a power logarithmic ansatz using the precalculated boundary conditions.

3. **Numerical integration**
   The differential equation system is solved numerically with high precision boundary conditions values evaluated with help of the high order asymptotic expansion.

4. **Avoiding singular points**
   In case the endpoint of the numerical integration is a singular point of the system of differential equations, a high precision expansion around the endpoint is performed. The unknowns appearing in this expansion are then matched with the numerical integration results offset from the endpoint.

As an example, the above methods are applied to the cut integral $\tilde{\Gamma}$ depicted in fig. 5.1 throughout this chapter. The normalization is chosen as

$$\tilde{\Gamma} = \left(i\pi^{(2-\epsilon)}\right)^4 e^{4\epsilon\gamma_E}\,\Pi_2\,\Gamma \tag{5.8}$$

with the two particle phase space

$$\Pi_2 = \pi^2\Gamma(1+\epsilon)\left(\frac{p^2}{\mu^2}\right)^{-\epsilon} \tag{5.9}$$

5.1.2. High precision asymptotic expansions

In general, multi-loop integrals depending on two scales can be expanded in kinematical invariants or masses z around any point z_0 away from thresholds into asymptotic series. This statement has been proven in the context of diagrammatic asymptotic expansions and although no proof exists for thresholds, it is generally assumed that the following ansatz holds:

$$I_n = \sum_{k=-2l}^{N_n} I_{n,k}\,\epsilon^k, \quad I_{n,k} = \sum_{n=n_0}^{N_z}\sum_{m=0}^{N_l} c_{n,m}\,z^{\frac{n}{k}}\log^m z, \tag{5.10}$$

$$\text{where} \quad \tilde{z} = z - z_0, \quad k = 1,2,3,\ldots, \quad N_{l,k} = l + k\,\Theta(k). \tag{5.11}$$

It is understood that all UV divergences are regularized dimensionally. $\Theta(x)$ is the standard Heaviside function. In the large-mass or the large-momentum limit, $k = 1$ (see 5.2) whereas expansions around arbitrary points may lead to roots with $k \neq 1$. Explicit calculations showed that $k = 1$ for every expansion employed in our case.
Plugging the ansatz (5.11) into the system of differential equations, the derivative can be applied directly and a comparison of coefficients of $x^n \log^m x$ terms leads to a system of ordinary equations. In general, this system consists of a large number of equations and its size scales with the number of master integrals, number of loops, required ϵ orders for the amplitude and the expansion depth N_z. To be able to obtain a solution of this system for large N_z and therefore high precision values for the master integrals around z_0, properties of the system of differential equations and the general structure of solutions have to be used. For this, an efficient method has been developed and implemented in `Mathematica` and `FORM` in the course of this work.
Using the fact that the coefficient matrix in eqn. (5.1) has a block-triangular structure, the system of equations can be solved recursively starting with the integrals with the least number of internal lines. Solving for an integral with n internal lines, according to eqn. (5.2) the inhomogeneous parts of the equations will only depend on already obtained integrals with $n-1$ propagators or less. Therefore, coupled systems occur only among integrals belonging to the same topology and the huge system of equations is effectively split into many small systems.
Derived from differential equations, one particular coefficient, $c_{\tilde{n},\tilde{m}}$, in the ansatz (5.11) represents the boundary condition at each order of ϵ of any master integral and has to

be determined with another technique. An important aspect of the method used in this work is the fact that values of boundary conditions have not to be specified a priori in the ansatz (5.11). Therefore, the system of equations is under constrained, i.e. the number of unknown variables is larger than the number of available equations. Although all values of $(\tilde{n}, \tilde{m})$ have to give the same results eventually, only some choices, restricted by the alternative method to determine the boundary conditions, allow for a solution of the system. In particular, diagrammatic large mass expansions only provide very few powers of the expansion, therefore only small values of $\tilde{n}$ are preferred. Moreover, we require non-logarithmic boundary coefficients, $\tilde{m} = 0$.
A crucial input to solve the system of differential equations are therefore the boundary powers of $\tilde{n}$ that should remain unknown during the recursive solution. For a single differential equation, these values can be obtained as follows.
Consider the general solution of a first order inhomogeneous differential equation

$$\frac{d}{dz} I(z) = A(z)\, I(z) + B(z) \quad \leftrightarrow \quad I(z) = \exp\left(\int dz\, A(z)\right) + p(z) \tag{5.12}$$

where $p(z)$ is one particular solution to the inhomogeneous differential equation. $B(z)$ is completely determined from the evaluation of previous equations and moreover has no influence on the minimal power needed in the expansion ansatz. It is therefore sufficient to analyze only the homogeneous part of the differential equation and neglect the particular solution $p(z)$. In our case, the coefficient A is determined from IBP relations and is therefore a rational function in z (and ϵ). Expanding A around small z in a Laurant series leads to

$$\begin{aligned} I(z) &= \exp\left(\int dz\, (\cdots + a_{-2} z^{-2} + a_{-1} z^{-1} + a_0 + a_1 z + \dots)\right) && (5.13) \\ &= z^{a_{-1}} \exp\left(\cdots - a_{-2} z^{-1} + a_0 z + \dots\right). && (5.14) \end{aligned}$$

Requiring that I should be expandable in a power logarithmic series immediately leads to $a_n = 0$ for $n < -1$. With this, we obtain

$$I = z^{a_{-1}}(1 + \tilde{a}_0 z + \tilde{a}_1 z^2 + \dots), \quad \tilde{a}_n = \tilde{a}_n(a_0, a_1, \dots). \tag{5.15}$$

Hence, a_{-1} is the smallest power of z in the expansion of I. For our solution we therefore require the boundary coefficient in the ansatz (5.11) for each master integral to be $c_{a_{-1},0}$. In the case that a_{-1} is rational, we have checked that an expansion using an ansatz of square roots leads in our case to results, where rational powers of z drop out. To speed up the evaluation to high orders, the value of a_{-1} is rounded down.
To solve the system of equations in an efficient way, the applied algorithm tries to minimize the number of required substitutions of already solved coefficients as far as possible. In a first step, the system of master integrals is ordered according to the number of internal lines, starting with the least. Each master integral's equations are then arranged order by order in ϵ starting from the highest pole and are sorted for increasing powers of z. With that ordering, each equation can be solved independently

of others, provided that the boundary coefficient powers $(\tilde{n}, \tilde{m})$ and the variable to be solved for are specified. The former is obtained as described above, the latter is determined from a rule motivated by the IBP reductions. In each equation containing the coefficient variables $c_{\{i\},\{j\}}$ with some sets $\{i\}$ and $\{j\}$ and the required boundary condition $c_{\tilde{n},0}$, the variable to be solved for is given by the $c_{n,m}$ with

$$n = \max(|\{i\} - \tilde{n}|) \quad \wedge \quad m = \max(|\{j\}|). \tag{5.16}$$

Given that the expansion is performed up to the N_zth term in the small quantity z, the relative accuracy $\Delta_{\text{exp}}^{n,k}$ for a coefficient $I_{n,k}$ can be roughly estimated from the cut-off of eqn. (5.11) for a given value z_0

$$\Delta_{\text{exp}}^{n,k} \approx z_0^{(N_z+1)} \log^{N_l}(z_0). \tag{5.17}$$

when N_z and N_l are the highest powers of z and l in the expansion, respectively.
In this work, the aforementioned technique has been used to determine high order expansions of all occurring master integrals around either the large-mass limit or the large-momentum limit. The validity of the obtained series has been cross checked in two different ways. On the one hand, plugging the expansions into both sides of the respective differential equations has to give a true answer for all obtained orders in z. On the other hand, all terms obtained from diagrammatic asymptotic expansions have to agree with the high precision series.
For the example master integral Γ depicted in fig. 5.1, the large mass expansion in $z = p^2/m^2$ for this particular integral up to $\mathcal{O}(\epsilon^0)$ and $\mathcal{O}(z^5)$ reads

$$\begin{aligned}
\Gamma \overset{z\to 0}{=}\quad & \frac{1}{\epsilon^3}\left(\frac{1}{3}z + \frac{1}{6}z^2 + \frac{11}{108}z^3 + \frac{5}{72}z^4 + \frac{137}{2700}z^5\right) \\
& + \frac{1}{\epsilon^2}\left[z\left(L_z + \frac{2}{3}\right) + z^2\left(\frac{L_z}{2} + \frac{13}{12}\right) + z^3\left(\frac{11L_z}{36} + \frac{197}{216}\right)\right. \\
& \quad \left. + z^4\left(\frac{5L_z}{24} + \frac{71}{96}\right) + z^5\left(\frac{137L_z}{900} + \frac{6137}{10125}\right)\right] \\
& + \frac{1}{\epsilon}\left[z\left(\frac{3L_z^2}{2} + 2L_z + \frac{5\zeta_2}{2} - \frac{1}{3}\right) + z^2\left(\frac{3L_z^2}{4} + \frac{13L_z}{4} + \frac{5\zeta_2}{4} + \frac{53}{24}\right)\right. \\
& \quad + z^3\left(\frac{11L_z^2}{24} + \frac{197L_z}{72} + \frac{55\zeta_2}{72} + \frac{12257}{3888}\right) + z^4\left(\frac{5L_z^2}{16} + \frac{71L_z}{32} + \frac{25\zeta_2}{48} + \frac{33845}{10368}\right) \\
& \quad \left. + z^5\left(\frac{137L_z^2}{600} + \frac{6137L_z}{3375} + \frac{137\zeta_2}{360} + \frac{1890493}{607500}\right)\right] \\
& + z\left(\frac{3L_z^3}{2} + 3L_z^2 + \left(\frac{15\zeta_2}{2} - 1\right)L_z + 5\zeta_2 - \frac{23\zeta_3}{3} + \frac{4}{3}\right) \\
& + z^2\left(\frac{3L_z^3}{4} + \frac{39L_z^2}{8} + \left(\frac{15\zeta_2}{4} + \frac{53}{8}\right)L_z + \frac{65\zeta_2}{8} - \frac{23\zeta_3}{6} + \frac{101}{48}\right) \\
& + z^3\left(\frac{11L_z^3}{24} + \frac{197L_z^2}{48} + \left(\frac{55\zeta_2}{24} + \frac{12257}{1296}\right)L_z + \frac{985\zeta_2}{144} - \frac{253\zeta_3}{108} + \frac{45221}{7776}\right)
\end{aligned}$$

$$
\begin{aligned}
&+z^4\left(\frac{5L_z^3}{16}+\frac{213L_z^2}{64}+\left(\frac{25\zeta_2}{16}+\frac{33845}{3456}\right)L_z+\frac{355\zeta_2}{64}-\frac{115\zeta_3}{72}+\frac{112919}{13824}\right)\\
&+z^5\left(\frac{137L_z^3}{600}+\frac{6137L_z^2}{2250}+\left(\frac{137\zeta_2}{120}+\frac{1890493}{202500}\right)L_z+\frac{6137\zeta_2}{1350}-\frac{3151\zeta_3}{2700}\right.\\
&\quad\left.+\frac{340754653}{36450000}\right).
\end{aligned}
\tag{5.18}
$$

where $L_z = \log z$ and ζ_i are the Riemann zeta numbers.

5.1.3. Numerical evaluation

The ϵ-expanded system of master differential equations can in principle also be used to compute exact values of one scale master integrals numerically for arbitrary values of the kinematical variable. To accomplish this, standard numerical techniques like the Runge-Kutta method and improvements are applicable.
Problematic, though, is the fact, that the generated differential equations in general contain singular points that lead to numerical instabilities along the path of integration. Moreover, only the asymptotic limits $z \to 0$ or $1/z \to 0$ of the master integrals occurring in this work are accessible in an automatized fashion and coincidentally the differential equations are singular in this limit in general. Hence, a numerical integration starting from $z = 0$ or $1/z = 0$ is not feasible.
To avoid these points of numerical instability, the following strategy is applied. Using the high order expansion described in the previous chapter, the master integrals are computed at a point z_i slightly apart from the singular point, e.g. at $z_i = 0.05$. These values then function as starting point for the numerical integration. Singular points on the integration contour are circumvented by shifting the path into the complex plane of z. Here we use an elliptical path with the endpoint lying on the real axis at the desired value z_e (compare fig. 5.1.3). Note, that this is only feasible if z_e is not a singular point of the differential equations. In this particular case, this technique has to be extended as described in section 5.1.4.

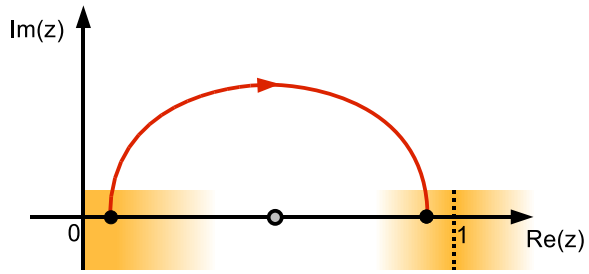

Figure 5.2.: Integration contours used for numerical integration with `ODEPACK`.

During the course of this work, the numerical evaluation has been implemented using the `FORTRAN` package `ODEPACK` utilizing double and quadruple precision to allow for high accuracy values. The error in each endpoint is estimated in two ways. On the one hand, the evaluation by `ODEPACK` leads to a relative error of

$$\Delta_{\text{num}}^{\text{glob}} \approx n\, \Delta_{\text{num}}^{\text{loc}} \tag{5.19}$$

where n is the number of needed steps to achieve the local relative numerical precision $\Delta_{\text{num}}^{\text{loc}}$. On the other hand, the error is estimated from three integrations along elliptical paths with different diameters δ_z. The so obtained precision estimate was always compatible with the expected relative error from eqn. (5.19). In addition, the integration is verified by comparison with the high precision expansions at a small value of z, e.g. $z = 0.1$.

For illustration of the mean global error estimates, a low precision run with $\Delta_{\text{num}}^{\text{loc}} = 10^{-13}$ for the whole set of master integrals of chapter 3.2 is shown in fig. 5.3, using both double and quadruple precision. It is remarkable, that although requiring the same $\Delta_{\text{num}}^{\text{loc}}$, for some points the error gets overall considerably larger when using double precision. Moreover, this effect is more pronounced for kinematical invariants further away from the integration start point. In contrast, in quadruple precision the error distribution is flat. The reason for this is the uncertainty introduced in the numerical evaluation due to roundoff error when numerical cancellations occur. These random roundoff errors are more severe in double precision and lead to the error requirement in the numerical evaluation not being satisfied. In consequence, the algorithm reduces the step size until eventually the error criterion is met. Therefore, the needed number of steps gets larger (by one order of magnitude in some cases) and the global error is increased.

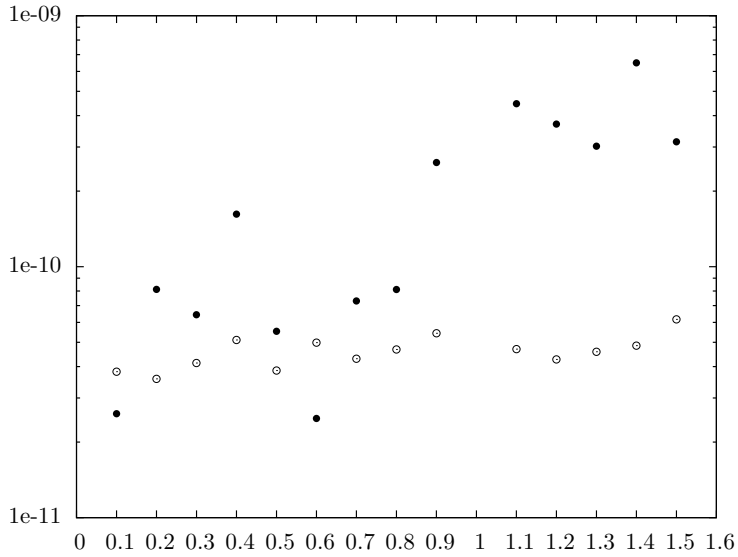

Figure 5.3.: Mean global error estimate of all master integrals occurring in the computation of chapter 3.2 for different values of $z = p^2/m^2$. Dots and circles represent the uncertainty obtained in double and quadruple precision, respectively. The local error was chosen as 10^{-13}.

For the integral of fig. 5.1, numerical results in the range $z = p^2/m^2 \in [0.1, 1.5]$ with $\Delta_{\text{num}}^{\text{loc}} = 10^{-14}$, resulting in a global error of about 10^{-11}, are given in tab. 5.1 up to $\mathcal{O}(\epsilon^0)$. The finite term is plotted in fig. 5.4. As expected, for $x > 1$ the integral being above threshold consequently acquires a non-vanishing imaginary part.

p^2/m^2	$\mathcal{O}(\epsilon^{-3})$	$\mathcal{O}(\epsilon^{-2})$	$\mathcal{O}(\epsilon^{-1})$	$\mathcal{O}(\epsilon^{0})$
0.1	0.03510934595	-0.1640341610	0.7208575034	-2.835873193
0.2	0.07427845763	-0.1732604783	0.9404490874	-3.267047141
0.3	0.1184731056	-0.0978319179	1.262942075	-3.211620425
0.4	0.1690505740	0.06195470506	1.832453446	-2.418896404
0.5	0.2280093463	0.3230080470	2.812457535	-0.3301029926
0.6	0.2984822706	0.7212312184	4.467773222	4.145041101
0.7	0.3858397714	1.327275573	7.309707601	13.35684118
0.8	0.5006722005	2.296256721	12.52991661	33.39329252
0.9	0.6701098853	4.077669229	23.98972356	86.76464548
1.1	1.169584058 $+i\,0.6380283502\,i$	6.948158691 $+11.24351212\,i$	8.885572071 $+91.87263030\,i$	-211.4730704 $+437.5925512\,i$
1.2	1.015039953 $+0.9436531891\,i$	2.226244951 $+13.07040811\,i$	-31.15656628 $+78.58539750\,i$	-351.1401381 $+222.7886955\,i$
1.3	0.8462287736 $+1.131400910\,i$	-1.221525639 $+13.20965908\,i$	-51.26632952 $+61.40965310\,i$	-371.1773196 $+76.04580368\,i$
1.4	0.6860471960 $+1.253012896\,i$	-3.795335526 $+12.71395633\,i$	-61.98381747 $+45.61622073\,i$	-354.3785861 $-24.31704827\,i$
1.5	0.5396911371 $+1.333112156\,i$	-5.757526722 $+11.95505827\,i$	-67.60652924 $+31.94738793\,i$	-325.0003599 $-94.56210722\,i$

Table 5.1.: Table of values for the finite part of the integral of fig. 5.1 with 10 digits accuracy obtained from a low precision numerical integration in quadruple precision.

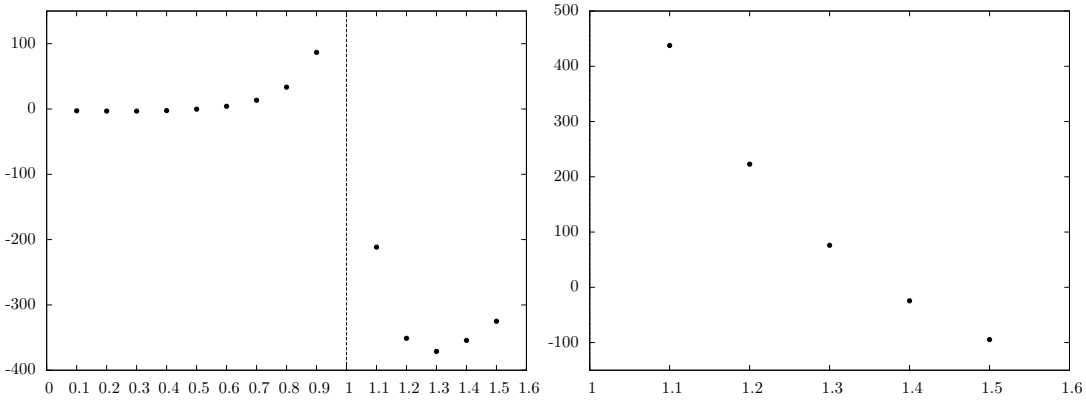

Figure 5.4.: Plot of the real and imaginary parts of the finite term of the integral of fig. 5.1. Below threshold, the imaginary part vanishes.

5.1.4. Accessing singular points

If the endpoint of integration z_e coincides with a singular point of the differential equations, the aforementioned strategy has to be modified. Of course, the integral itself has to be a smooth function in the vicinity of z_e, otherwise a regularization is needed (see chapter 5.3). In this case, a separate high precision asymptotic expansion around

$\tilde{z} = z - z_e$ is performed using the method of chapter 5.1.2. Solving the system of differential equations numerically up to a stable point z_m close to z_e, the remaining unknowns in the expansion can be fixed by comparison of the series with the numerical results at z_m. The master integrals in z_e are then eventually given by the first term of the asymptotic expansion, assuming that the series is well-defined in the limit $\tilde{z} \to 0$.
Since the expansion is calculated analytically, the so introduced error Δ_{match} is entirely determined by the obtained precision $\Delta_{\text{num}}^{\text{glob}}$ from numerical integration and the depth N of the series. In general, for a given ϵ order k of a master integral I_n,

$$\Delta_{\text{match}} = \max(\Delta_{\text{num}}^{\text{glob}}, \Delta_{\text{exp}}^{N,k}) \tag{5.20}$$

The quality and validity of this matching procedure can be verified by different means. Firstly, small variations of the matching point z_m have to lead to consistent values in the range of (5.20). Secondly, the matching has to give the same results when performed at different points, e.g. $z_m < z_e$ and $\tilde{z}_m > z_e$. As a last cross check, the series around z_e has to agree at some other close value $z \approx z_e$ with the numerical integration.
For the example integral, the differential equations are singular at the on-shell condition $z_e = p^2/m^2 = 1$. Therefore, the asymptotic expansion is performed about the value $\tilde{z} = z - 1$ up to $\tilde{z}^{18}$, matched with the numerical evaluation at $z_m = 0.9$ and, as a cross-check, at $z_m = 1.1$. The first five terms of the expansion read (truncated to 10 digits of precision for brevity)

$$\begin{aligned}
\Gamma \overset{z\to 1}{=} \ & \tfrac{1}{\epsilon^3} && (1.096622711 + z(-0.6666666666 + 0.6666666666\, L_z - 0.3333333333\, L_z^2) \\
& && +z^2(-0.166666667 + 0.333333333\, L_z) - z^3(0.07407407407 + 0.1111111111\, L_z) \\
& && +z^4(0.06944444444 + 0.05555555555\, L_z) - z^5(0.05444444444 + 0.03333333333\, L_z)) \\
+ \ & \tfrac{1}{\epsilon p^2} && (11.51444921 + z(-2.693871838 + 13.91306960\, L_z - 3.666666667\, L_z^2 + 1.222222222\, L_z^3) \\
& && +z^2(-10.12320147 + 4.333333333\, L_z - 1.666666667\, L_z^2) \\
& && +z^3(2.275635057 - 0.7037037037\, L_z + 0.5555555556\, L_z^2) \\
& && +z^4(-0.9912125902 + 0.2037037037\, L_z - 0.2777777778\, L_z^2) \\
& && +z^5(0.5475979245 - 0.07222222222\, L_z + 0.1666666667\, L_z^2)) \\
+ \ & \tfrac{1}{\epsilon p} && (105.1354089 \\
& && +z(-55.61798348 + 90.61310137\, L_z - 56.92643408\, L_z^2 + 10.11111111\, L_z^3 - 2.527777778\, L_z^4) \\
& && +z^2(-46.95418161 + 63.13656595\, L_z - 17.50000000\, L_z^2 + 4.444444444\, L_z^3) \\
& && +z^3(-1.283300553 - 12.24613927\, L_z + 3.009259259\, L_z^2 - 1.481481481\, L_z^3) \\
& && +z^4(2.897277615 + 5.077544942\, L_z - 0.94907407412\, L_z^2 + 0.7407407407\, L_z^3) \\
& && +z^5(-2.451999253 - 2.773332521\, L_z + 0.3847222222\, L_z^2 - 0.4444444444\, L_z^3)) \\
+ \ & && (783.9249173 \\
& && +z(-131.5206722 + 945.8051338\, L_z - 328.1418344\, L_z^2 + 139.1649103\, L_z^3 \\
& && \quad -18.63888889\, L_z^4 + 3.727777778\, L_z^5) \\
& && +z^2(-742.1859225 + 450.1905750\, L_z - 228.2008157\, L_z^2 + 42.50000000\, L_z^3 - 8.055555556\, L_z^4) \\
& && +z^3(123.0862200 - 38.93082993\, L_z + 44.79070379\, L_z^2 - 7.515432099\, L_z^3 + 2.685185185\, L_z^4) + \\
& && +z^4(-50.80203592 + 6.095250390\, L_z - 18.66116980\, L_z^2 + 2.461419753\, L_z^3 - 1.342592593\, L_z^4) \\
& && +z^5(27.33757594 + 0.2500970586\, L_z + 10.21890095\, L_z^2 - 1.049537037\, L_z^3 + 0.805555556\, L_z^4))
\end{aligned} \tag{5.21}$$

The numerical on-shell result at $z = 1$, with all digits given as obtained from the uncertainty analysis, reads

$$\begin{aligned}\Gamma \overset{z=1}{=} \quad & 1.096622711227418\ \epsilon^{-3} \\ + \quad & 11.51444920525186\ \epsilon^{-2} \\ + \quad & 105.1354089210443\ \epsilon^{-1} \\ + \quad & 783.9249173219096. \end{aligned} \tag{5.22}$$

Fig. 5.5 shows a plot of the expansion for different depths along with the numerical values of table 5.1.

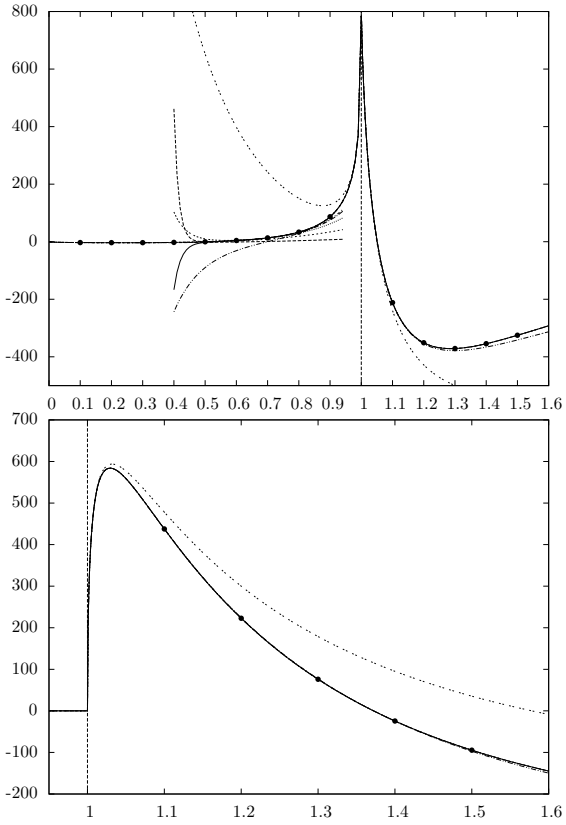

Figure 5.5.: Plots of the imaginary and real parts of the integral depicted in fig. 5.1. Here, the numerical values, together with the first 2,5,10,15 and 20 terms of the large mass ($z \to 0$) and the threshold expansion ($z \to 1$) are shown.

5.2. Diagrammatic asymptotic expansions

Multi-loop integrals containing a variety of different scales pose a serious challenge in higher order quantum field theory calculations. If however the scales λ_i of the diagram, which can be internal masses or invariant kinematics, form a clear hierarchy where at least $\lambda_1 \gg \lambda_2, \lambda_3, \ldots$, it has been shown [61, 62] that a well defined method exists to compute asymptotic expansions in the limit $1/\lambda_1 \to 0$.
When expanding Feynman integrals in a small parameter one has to be very careful as taking the limit in the integrand does not resemble the behaviour of the integral in this limit in general. Instead, a so called expansion by regions has to be performed, where expansions in different scales are valid only over certain subspaces of the integration domain. In the case of the above hierarchy of scales, the approach applied to an integral I_Ω of topology Ω can be expressed as

$$I_\Omega = \sum_\omega I_{\Omega/\omega} \mathcal{T} I_\omega. \tag{5.23}$$

In the above formula, the sum runs over certain sub topologies ω, which are extracted from I_Ω and are represented by the integral I_ω. The prescription of how to extract ω depends on the type of large scale limit one is interested in. The operator $\mathcal{T}$ expands each sub topology in all small parameters, whereas $I_{\Omega/\omega}$ is the remnant of the integral after all propagators of ω have been extracted.
As eqn. (5.23) gives a prescription for asymptotic expansions of multi-loop integrals in terms of sub topologies, it is perfectly suited for automatization. The procedure consists of the following steps:

- The package `DiaGen` [123] providing powerful routines for the handling and analysis of topological information for multi-loop diagrams is used. All sub-topologies $I_{\Omega/\omega}$ and I_ω that fulfill the above requirements are determined.
- $\mathcal{T} I_\omega$ is computed and the full asymptotic expansion is composed with the help of `FORM`
- The resulting different sets of integrals are expressed through a smaller set of new master integrals utilizing separate IBP reductions.

This way, usually only a few integrals remain and have to be provided as input. A complete list of these integrals needed in this work is provided in appendix B. One drawback of this method in practice is, however, that only the first several terms of the asymptotic series are accessible with this approach. The reason for this is that expanding the sub-topologies in small parameters produces integrals with a growing number of products of external and loop momenta in the numerators proportional to the expansion depth. On the one hand, simplification of these terms leads to very large intermediate expressions that slow down the computation considerably. On the other hand, one is limited by the IBP reduction which has a computational complexity that also scales strongly with the number of irreducible scalar products in the numerators.

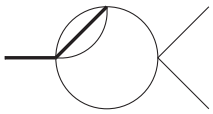

Figure 5.6.: Vertex integral I_{lm}, with massless (thin) and massive (thick) lines and external momentum p^2.

In the following we are interested in the so called large-mass and large-momentum limits of multi-loop integrals, that contain massless, light (mass m_l) and very massive propagators of mass m_h and some external momenta p_i.

Large mass expansion In the so called large mass limit, where one internal mass is taken much larger than all other scales, the sum in eqn. (5.23) runs over all sub-topologies ω of Ω with the requirement [61], that

- ω contains all propagators of heavy mass m_h of Ω and
- ω is one particle irreducible with respect to massless lines.

The obtained integrals I_ω are expanded in all small scales, resulting in one-scale vacuum integrals containing massless and heavy lines. The remaining integral $I_{\Omega/\omega}$ is obtained by shrinking the extracted sub-topology to a vertex and is composed of only massless or light lines. Only this separation of scales makes this whole approach feasible, as it effectively reduces the number of scales in the resulting integrals by one.
It is important to note that this technique is not only applicable to ordinary Feynman integrals but works also with cut integrals occurring in the computations of this work, as long as the cut goes only through massless lines. In this case, cut lines are not included in the sub topologies ω since vacuum integrals with cut lines vanish per definition and the whole cut structure is contained in the $I_{\Omega/\omega}$'s.
As an example for the large mass expansion, consider the vertex integral of fig. 5.6 with massless propagators except for one heavy line. Following the above rules, the integral can be represented diagrammatically in the large mass limit, e.g. when the internal mass is much larger than the kinematical invariant, $m^2 \gg p^2$ as

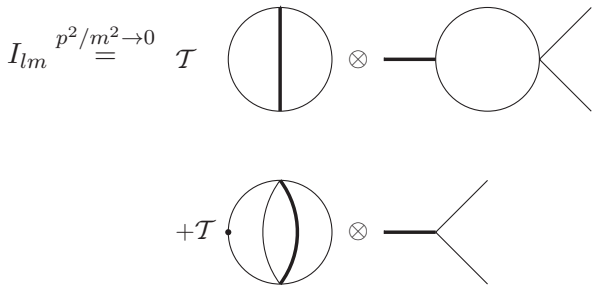

The dot on the line indicates that the corresponding propagator power is incremented.

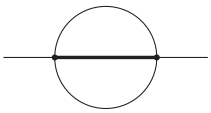

Figure 5.7.: Propagator-type integral I_{lp}, with massless (thin) and massive (thick) lines and external momentum p^2.

Using different IBP reductions for the massless and massive diagrams, respectively, we can express integrals with raised propagators and irreducible products in the numerator through master integrals. Taking into account that the boundary integrals are evaluated at the corresponding mass scale, the result, valid up to $\mathcal{O}(z^1 = (p^2/m^2)^1)$ and to all powers in ϵ if expanded, is then given by

$$I_{lm} \overset{p^2/m^2\to 0}{=}$$

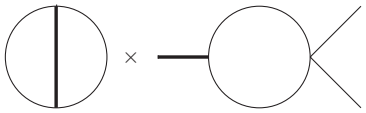

$$\times \left(z^{2\epsilon-1}\right)$$

$$+$$

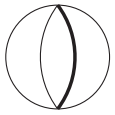

$$\times z^{3\epsilon-1} f(\epsilon, z) + \mathcal{O}(z^2)$$

with

$$f(\epsilon,z) = \frac{(2-7\epsilon+6\epsilon^2)}{\epsilon(12+8\epsilon-7\epsilon^2-2\epsilon^3+\epsilon^4)} \left(12+8\epsilon-\epsilon^2(7+6z)-\epsilon^3(2-17z+z^2)\right.$$
$$\left. +\epsilon^4(1+4z)+\epsilon^5 z(-3+7z)+6\epsilon^6 z^2\right). \quad (5.24)$$

Note that $f(\epsilon, z)$ is entirely determined from the IBP reduction as all sub topologies are invariant under $\mathcal{T}$.

Large momentum expansion Considering the large-momentum limit, i.e. the case when one external momentum p^2 is much larger than any other scale, $p^2 \gg m_l^2$ or $p^2 \gg m_h^2$, equation (5.23) has to be interpreted in such a way that the sum runs over all sub topologies ω of Ω that fulfill

- ω contains all vertices connected to external lines of large inflowing momentum and
- ω is one particle irreducible after connecting these vertices with an additional line

After expanding I_ω, one ends up with massless diagrams containing at least the external lines of large momentum while the remnant diagrams contain massive lines.
As this procedure requires the evaluation of a larger number of sub topologies in most cases, the large momentum expansion is illustrated on the simpler 2-loop example in fig. 5.7.

Applying the prescription leads to the diagrammatic representation for $m^2/p^2 \to 0$

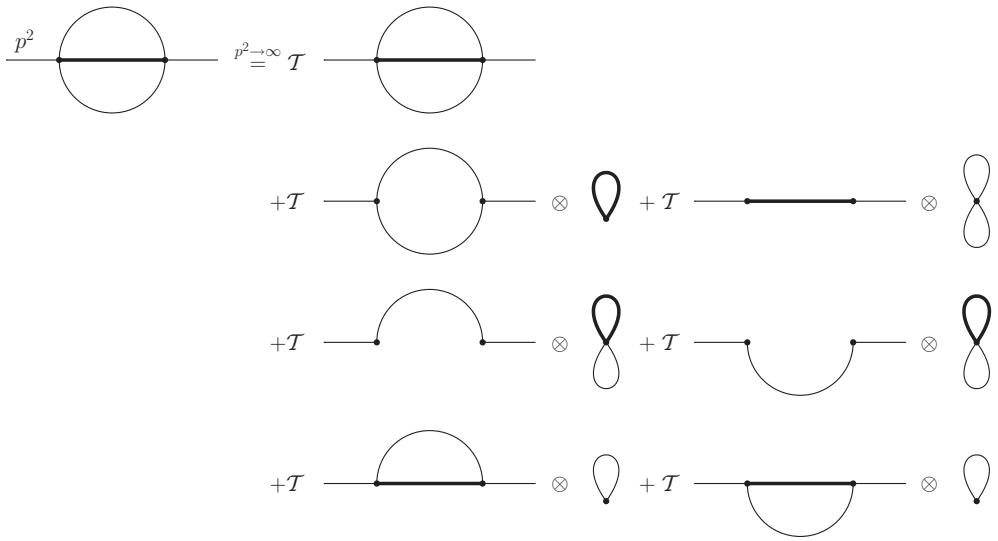

Since all vacuum integrals with scaleless one particle irreducible subgraphs vanish by definition, only the first two diagrams that are invariant under the operator $\mathcal{T}$ in the above expression contribute in the large momentum limit. All occurring integrals in this example are master integrals given in appendix B and the dependence on p^2 is directly determined from their mass dimensions.

5.3. Continuation from off-shell to on-shell integrals

An issue encountered in the evaluation of master integral is related to logarithmic divergences appearing in the threshold limit of off-shell integrals. In the context of this work, this kind of divergence can appear in the evaluation of master integrals with the help of differential equations in the on-shell limit, if it coincides with a threshold. Fortunately, in this case it is possible to replace on-shell divergent integrals in the masters basis with regularized ones.
This behaviour of off-shell integrals can already be shown for a simple example

$$\Gamma^{off}(p^2, m^2) = \int d^d k \, \frac{1}{((p+k)^2 - m^2)^2 k^2} \tag{5.25}$$

depicted in fig. 5.8. With the method of Feynman parameters, this integral can easily be computed and yields

$$\Gamma(q^2, m^2) = \frac{i\pi^2}{p^2} \log\left(1 - \frac{p^2}{m^2}\right). \tag{5.26}$$

Eqn. (5.26) is clearly UV finite but divergent at the threshold $p^2 \to m^2$. One can understand this behaviour better by directly evaluating the diagram on the threshold,

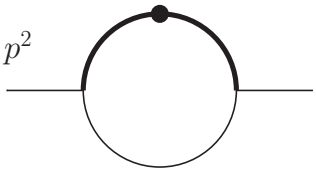

Figure 5.8.: Simple example for a diagram with a logarithmic singularity at threshold. The dot indicates a propagator's power incremented by one.

i.e. by setting $p^2 = m^2$ in the integrand:

$$\begin{aligned}\Gamma^{thr}(p^2 = m^2) &= \int d^dk \, \frac{1}{((p+k)^2 - m^2)k^4} \\ &= \int d^dk \, \frac{1}{(k^2+2pk)^2 k^2}. \end{aligned} \tag{5.27}$$

For small loop momentum k the integral behaves as $d^dk/((pk)^2\, k^2)$ and is therefore, exactly as observed above, logarithmically divergent in $d = 4$ dimensions. Up to $\mathcal{O}(\epsilon^0)$ it explicitly reads

$$\Gamma^{thr}(p^2 = m^2) = \frac{i\pi^{d/2} e^{-\epsilon\gamma_E}}{2m^2} \left[\frac{1}{\epsilon} - \log\left(\frac{m^2}{\mu^2}\right)\right] \tag{5.28}$$

Now let us assume, that Γ^{off} is a master integral to be evaluated with the method of differential equations, hence the limit $p^2 \to m^2$ cannot be accessed directly and eqn. (5.28) is not known. The idea now is to perform two separate IBP reductions, both off-shell and on-shell. The former reduction is then used to obtain a result for Γ^{off} in terms of another, regularized master integral $\tilde{\Gamma}^{off}$

$$\tilde{\Gamma}^{off}(p^2, m^2) = \int d^dk \, \frac{pk}{((p+k)^2 - m^2)^2 k^2}. \tag{5.29}$$

This integral behaves like $d^dk/(pk\, k^2)$ for $p^2 \to m^2$ and is therefore finite in $d = 4$ dimensions. So it can be computed off-shell with differential equations. On-shell, one obtains relations between Γ^{on} and the corresponding regularized $\tilde{\Gamma}^{on}$ with the scalar product pk in the numerator of the integrand in the following way

$$\begin{aligned}\tilde{\Gamma}^{on} &= \int d^dk \, \frac{kp}{(k^2+2pk)^2 k^2} \\ &= \int d^dk \, \frac{1/2(k^2+2kp) - 1/2k^2}{(k^2+2pk)^2 k^2} \\ &= \frac{1}{2}\int d^dk \, \frac{1}{(k^2+2pk)k^2} - \frac{1}{2}\int d^dk \, \frac{1}{(k^2+2pk)^2}. \end{aligned} \tag{5.30}$$

Using the second IBP reduction, the integrals on the right-hand side can now again be expressed through master integrals and, more specifically, Γ^{on}. As these relations were

obtained on-shell, all appearing divergences are directly parametrized by poles in ϵ, and we get

$$\tilde{\Gamma}^{on} \propto \epsilon\, \Gamma^{on} + \text{finite}. \tag{5.31}$$

Obviously, both $\tilde{\Gamma}^{off}$ and $\tilde{\Gamma}^{on}$ are regular and have to give the same result on-shell. Hence, providing the numerical value of $\tilde{\Gamma}^{off}$ at threshold allows eventually for a evaluation of Γ^{on}.
It is interesting to note, that with this method logarithmic divergences can be converted into divergences in ϵ.

Part III.

Conclusions and outlook

6. Conclusions and outlook

In this thesis we discuss the various perturbative and non-perturbative contributions to and the resulting branching ratio estimate of the inclusive radiative $\overline{B} \to X_s\gamma$ decay up to the NNLO of QCD corrections. In particular, we have presented the current status of the NNLO programme and provide important parts of yet missing contributions involving matrix elements of four-quark operators at this level of accuracy. The main goal of this work is to contribute to the reduction of the extrapolation uncertainty of about 3 % in the branching ratio.

Sizeable contributions to the branching ratio of the $\overline{B} \to X_s\gamma$ decay arise from fermionic and bosonic corrections of charm quark mass dependent matrix elements at $\mathcal{O}(\alpha_s^2)$ and therefore the current NNLO estimate depends crucially on these quantities. We have evaluated fermionic corrections in both the massless and, for the first time, the massive case where the charm and bottom quark masses are kept at their physical values. The former result is an important input in the SM branching ratio estimate and our independent evaluation confirms the findings of [98]. Our new results for massive fermionic corrections revealed a strong deviation from the massless approximation in the bottom quark case, while the charm quark contribution is well estimated in this limit. This leads to the conclusion, that a four-flavour scheme for radiative corrections is preferred over the usually assumed five active flavours in the branching ratio estimate determination. Taking our newly obtained mass effects into account, the $\overline{B} \to X_s\gamma$ branching ratio at NNLO is affected by +1.6 % [104]. Allowing for massive fermionic corrections, we have taken the first step on the way to an evaluation of charm quark mass dependent matrix elements at the physical mass scales, which would complete the NNLO programme and remove the remaining perturbative uncertainty at this order of perturbation theory. This is a very challenging task as it involves higher loop vertex integrals containing two mass scales. In this work, we have developed techniques for the computation of this type of multi-loop integrals in a systematic and automatized approach. One bottle-neck in the evaluation of fully massive bosonic corrections to charm dependent matrix elements turns out to be the necessary IBP reduction of multi-loop integrals. Once this reduction is available, our methods can be applied, thereby finalizing the NNLO determination of the missing four-quark matrix elements.

Another topic discussed in the present thesis is the possibility to reduce the extrapolation uncertainty in the easier, but still involved, massless charm quark limit. We have presented for the first time the full purely virtual corrections to the four-quark operator at the NNLO including all bosonic contributions in the limit of vanishing charm quark mass. On its own, this result is infrared divergent and has to be complemented with the corresponding real radiation. Therefore, we have evaluated parts of the interference of the four quark operators with the magnetic dipole operator and provide a framework

to complete this work in the near future. The new results constitute two- and three-particle final state contributions to the aforementioned interference, which contain the most complicated multi-loop structures. The remaining not yet available parts, which are four- and five-particle states involve more complicated phase-space integrations but can in principle be determined with the approach here presented. Once all contributions to the interference in the massless charm quark limit are available, the endpoint of the extrapolation used in the branching ratio estimate can be fixed and the remaining uncertainty can be largely reduced.

From the technical point of view, we have presented an automatized method for the high precision numerical determination of two-scale multi-loop integrals for arbitrary kinematics, providing also a continuation to the threshold. As a byproduct, asymptotic expansions to high orders in the small quantity can be evaluated. In principle, this technique can be used in different interesting high precision problems in quantum field theory, like the four-loop QCD corrections to the photon propagator as discussed in the appendix or, with some modifications, NNLO corrections to the $t\bar{t}$ production at hadron colliders [131].

Part IV.

Appendices

A. Double-fermionic corrections to the photon propagator at $\mathcal{O}(\alpha_s^3)$

Correlators of two currents, basic objects in Quantum Field Theory, provide important information for both theoretical and phenomenological applications. Depending on the Lorentz structure of the current under consideration, different interesting observables are directly related to these quantities, like the hadronic cross section in electron-positron annihilation, $R(s)$, and decay rates of Z- and Higgs-bosons.
On this account current correlators are investigated thoroughly in perturbation theory, where even high order calculations are possible. Some applications, like the determination of the charm and bottom quark masses through sum-rules carried out to four loops in [132, 133], corrections to the ρ parameter [134, 135] or the recent evaluation of α_s from low energy data at the same level of precision [136], require asymptotic expansions of heavy quark correlators in the low and/or high energy limits. Other studies, however, necessitate the knowledge of the full external momentum dependence p^2, for instance the determination of the fine structure constant at the Z-boson mass scale, $\alpha_{\rm em}(M_Z)$ [137].
Up to the three-loop level, all physically relevant correlators have been computed including the full quark mass dependence in [138, 139, 140] by deriving Padé approximants from asymptotic expansions. At four-loop accuracy, in the case of the vector current including one heavy quark, the first two terms in the low energy series are currently known [132, 141] and were obtained by direct Taylor expansion of all propagator-type integrals and subsequent reduction of tadpole diagrams. In the high energy limit, besides the leading massless contribution [142, 143, 144, 145, 146, 147] , the first two mass correction terms of the absorptive part of the scalar, vector and axial-vector current correlators are also available [148, 149], partially even to five loops [150, 151].
Unfortunately, the techniques used to achieve these results are, due to their huge computational complexity, not suitable for the computation of higher order terms in the expansions. However, reconstructing the full momentum dependence at $\mathcal{O}(\alpha_s^3)$ is possible with the here developed method of differential equations combined with asymptotic expansions. Using parts of this technique, we were already able to compute the first 30 terms in the low energy expanded polarization function at $\mathcal{O}(\alpha_s^2)$ in [152]. Recently, these results were confirmed in [153] utilizing the same approach.
The purpose of this chapter is to use the newly developed technique to another interesting physics problem of a comparative complexity as the $\overline{B} \to X_s\gamma$ decay evaluation. We compute the vacuum polarization for low and high energies as expansions up to $(p^2)^{30}$ and $(p^2)^{-15}$, respectively, and moreover the full momentum dependence in numerical form in the Euclidean and Minkowskian region. As new results, we extend the available information in the high energy domain at $\mathcal{O}(\alpha_s^2)$ and provide the double fermionic

contributions to the vector current correlator at $\mathcal{O}(\alpha_s^3)$.

A.1. Definitions

Given the vector current $j^\mu(x) = \overline{q}_h(x)\gamma^\mu q_h(x)$ composed of the heavy quark field $q_h(x)$ with mass m, the two point correlator is defined by

$$\Pi^{\mu\nu}(p^2) = i \int dx e^{ixp} \langle 0|T j^\mu(x) j^\nu(0)|0\rangle \tag{A.1}$$

where p^μ is the external momentum. A convenient representation of the tensor $\Pi^{\mu\nu}(p^2)$ through the scalar vacuum polarization function $\Pi(p^2)$ is given by

$$\Pi^{\mu\nu}(p^2) = (-p^2 g^{\mu\nu} + p^\mu p^\nu)\Pi(p^2) + p^\mu p^\nu \Pi_L(p^2). \tag{A.2}$$

Transversality of the vector current correlator requires $\Pi_L(p^2) = 0$. Through the optical theorem the aforementioned hadronic ratio $R(s)$ is related to the current correlator

$$R(s) = \frac{\sigma(e^+e^- \to \text{hadrons})}{\sigma(e^+e^- \to \mu^+\mu^-)} = 12\pi \text{Im}\Pi(p^2 = s + i\epsilon). \tag{A.3}$$

In the framework of perturbation theory, the polarization function can be expanded in the strong coupling as

$$\Pi(p^2) = Q_h^2 \frac{3}{16\pi^2} \sum_{k\geq 0} \left(\frac{\alpha_s(\mu)}{\pi}\right)^k \Pi^{(k)}(p^2). \tag{A.4}$$

Since in this work the focus is set on double fermionic contributions at $\mathcal{O}(\alpha_s^3)$ stemming form diagrams sketched in fig. A.1, it is convenient to decompose $\Pi^{(3)}(p^2)$ into bosonic and fermionic contributions,

$$\begin{aligned} \Pi^{(3)}(p^2) \;=\; & C_F^3\, \Pi_{\text{A}}^{(3)}(p^2) + C_F^2\, C_A\, \Pi_{\text{NA},1}^{(3)}(p^2) + C_F\, C_A^2\, \Pi_{\text{NA},2}^{(3)}(p^2) \\ & + C_F^2\, T_F\, \Pi_{\text{sf,A}}^{(3)}(p^2) + C_F\, C_A\, T_F\, \Pi_{\text{sf,NA}}^{(3)}(p^2) \\ & + C_F\, T_F^2\, \Pi_{\text{df}}^{(3)}(p^2), \end{aligned} \tag{A.5}$$

where $\Pi_{\text{sf}}^{(3)}(p^2)$ and $\Pi_{\text{df}}^{(3)}(p^2)$ denote terms proportional to n_f and n_f^2, respectively, with n_f being the number of active flavours. C_F refers to the Casimir operator and T_F to the trace of the fundamental representation of $SU(N)$. Because of the mass hierarchy in the quark sector only the heavy quark is considered massive whereas all lighter ($n_l = n_f - 1$) quarks are treated as massless.

Using the fact that the double fermionic contribution contains no massless cuts, $\Pi_{\text{df}}^{(3)}(p^2)$ can be expanded in a simple power series in the low energy limit $p^2 \to 0$. In the large energy limit $p^2 \to -\infty$, however, non-integer powers of p^2 arise and lead to additional

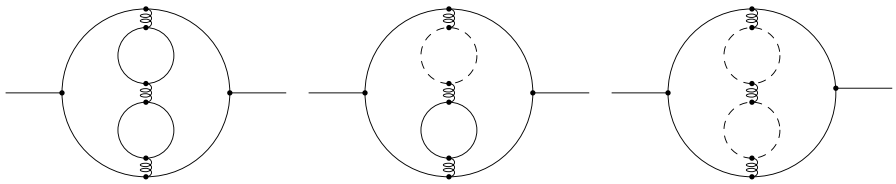

Figure A.1.: Diagrams contributing to $\Pi^{(3)}_{\rm df}(p^2)$. Solid (dashed) lines refer to massive (massless) propagators.

logarithms of the form $\log(-p^2/m(\mu)^2)$. Thus, defining $z = p^2/4m(\mu)^2$, we end up with the expansions

$$z \to 0: \qquad \Pi^{(3)}_{\rm df}(z) = \sum_{n>0} C^0_n(\mu)\, z^n, \tag{A.6}$$

$$z \to -\infty: \qquad \Pi^{(3)}_{\rm df}(z) = \sum_{n,m} C^\infty_{nm}(\mu)\, z^{-n}\, \log^m(-z). \tag{A.7}$$

A.2. Calculation

The basic idea for computing the full p^2-dependence of the vacuum polarization function is to deal with massive propagator-type integrals. Although the number of integrals is moderate (approx. 10^4 for the whole four-loop contribution) they pose a challenge as far as the reduction to a small set of master integrals is concerned, since two variables, z and $d = 4 - 2\epsilon$, the dimension of space-time, are involved. For the determination of these master integrals, however, an efficient method through differential equations exists and allows for asymptotic expansions to high orders in the external momentum and high precision numerics.

In a first step all Feynman diagrams contributing to the double fermionic corrections have been projected onto scalar integrals, which were subsequently reduced to a set of 46 master integrals with the help of integration-by-parts (IBP) identities [56] and the Laporta algorithm [55] implemented in `IdSolver` [128].
In the low- ($z \to 0$) and high-energy ($y \to 0$) limits, the system was solved by ansätze similar to eqns. (A.6, A.7) for each master integral and coefficients of the series were determined recursively up to high powers in z and y, respectively.
Boundary conditions in the low energy limit are given by massive tadpole diagrams up to the four-loop level. In the opposite limit, all boundary conditions were determined from automatized diagrammatic large momentum expansions which lead to products of at most three loop massive tadpoles with massless propagators. All needed integrals are depicted and explicitely given in appendix B.
Furthermore, the Mellin-Barnes (MB) method has been used at a few points to check the obtained values from direct integration. For this purpose, MB representations have

been automatically generated with the package `MBrepresentation` [129], analytically continued in ϵ and numerically integrated with help of the `MB` package [124]. We observed that the high-energy expansion works very well above at least $z > 5$ and therefore the numerical integration was undertaken up to $z = 10$. This fact is also used as a cross-check of the high-energy expansion against the numerically computed polarization function.
In a last step, we performed the renormalization of the mass $m(\mu)$, the strong coupling $\alpha_s(\mu)$ and the external current in the $\overline{\text{MS}}$-scheme.

A.3. Results

All analytical results for the coefficients in the small- and high-energy series in the $\overline{\text{MS}}$-scheme were obtained up to the 30th and 15th term, respectively. Apart from the new expressions at the four-loop level, we also provide so far unknown terms needed for renormalization in the large-energy expansion at the three-loop level. The Taylor series for $z \to 0$ is already known to sufficient depth [152, 153].
For the sake of clarity, here we give only the first five terms of both series at $\mathcal{O}(\alpha_s^3)$. The first coefficients in the limit $z \to 0$ are given by

$$
\begin{aligned}
C_1^0 &= \frac{163868}{98415} - \frac{3287}{2430}\,\zeta_3 + \frac{203}{324}\,l_m\zeta_3 - \frac{14483}{21870}\,l_m + \frac{236}{3645}\,l_m^2 + \frac{8}{135}\,l_m^3 + n_l\left(\frac{262877}{262440}\right.\\
&\quad - \frac{116}{81}\,a_4 - \frac{29}{486}\,l_2^4 + \frac{29}{486}\,l_2^2\pi^2 + \frac{1421}{58320}\pi^4 - \frac{38909}{19440}\,\zeta_3 + \frac{203}{324}\,l_m\,\zeta_3 - \frac{3779}{21870}\,l_m\\
&\quad \left. + \frac{472}{3645}\,l_m^2 + \frac{16}{135}\,l_m^3\right) + n_l^2\left(\frac{42173}{32805} - \frac{112}{135}\,\zeta_3 + \frac{1784}{3645}\,l_m + \frac{236}{3645}\,l_m^2 + \frac{8}{135}\,l_m^3\right)\\
C_2^0 &= \frac{1842464707}{646652160} - \frac{2744471}{1064448}\,\zeta_3 + \frac{14203}{27648}\,l_m\,\zeta_3 - \frac{676663}{870912}\,l_m - \frac{1468}{42525}\,l_m^2 + \frac{16}{315}\,l_m^3\\
&\quad + n_l\left(\frac{95040709}{62705664} - \frac{2029}{1728}\,a_4 + \frac{2029}{41472}\,l_2^2\pi^2 - \frac{2029}{41472}\,l_2^4 + \frac{99421}{4976640}\pi^4 - \frac{12159109}{4644864}\,\zeta_3\right.\\
&\quad + \frac{14203}{27648}\,l_m\,\zeta_3 - \frac{153560977}{326592000}\,l_m - \frac{2936}{42525}\,l_m^2 + \frac{32}{315}\,l_m^3\Big) + n_l^2\left(\frac{15441973}{19136250} - \frac{32}{45}\,\zeta_3\right.\\
&\quad \left. + \frac{195679}{637875}\,l_m - \frac{1468}{42525}\,l_m^2 + \frac{16}{315}\,l_m^3\right) \qquad \text{(A.8)}\\
C_3^0 &= \frac{56877138427}{12609717120} - \frac{6184964549}{1556755200}\,\zeta_3 + \frac{12355}{20736}\,l_m\,\zeta_3 - \frac{224445289}{244944000}\,l_m - \frac{310736}{4465125}\,l_m^2\\
&\quad + \frac{128}{2835}\,l_m^3 + n_l\left(\frac{60361465477}{29393280000} - \frac{1765}{1296}\,a_4 - \frac{1765}{31104}\,l_2^4 + \frac{1765}{31104}\,l_2^2\pi^2 + \frac{17297}{746496}\pi^4\right.\\
&\quad - \frac{57669161}{17418240}\,\zeta_3 + \frac{12355}{20736}\,l_m\,\zeta_3 - \frac{37155186557}{60011280000}\,l_m - \frac{621472}{4465125}\,l_m^2 + \frac{256}{2835}\,l_m^3\Big)\\
&\quad + n_l^2\left(\frac{31556642272}{49228003125} - \frac{256}{405}\,\zeta_3 + \frac{15480824}{52093125}\,l_m - \frac{310736}{4465125}\,l_m^2 + \frac{128}{2835}\,l_m^3\right) \qquad \text{(A.9)}\\
C_4^0 &= \frac{270605350139987}{40351094784000} - \frac{692437613459}{119558799360}\,\zeta_3 + \frac{2522821}{3538944}\,l_m\,\zeta_3 - \frac{4400766606253}{4138573824000}\,l_m\\
&\quad - \frac{1082216}{12629925}\,l_m^2 + \frac{256}{6237}\,l_m^3 + n_l\left(\frac{432564184014463}{165542952960000} - \frac{360403}{221184}\,a_4 - \frac{360403}{5308416}\,l_2^4\right.\\
&\quad + \frac{360403}{5308416}\,l_2^2\pi^2 + \frac{17659747}{637009920}\pi^4 - \frac{44387709491}{10899947520}\,\zeta_3 + \frac{2522821}{3538944}\,l_m\,\zeta_3 - \frac{143778598477}{189621927936}\,l_m
\end{aligned}
$$

$$
\begin{aligned}
&-\frac{2164432}{12629925}\,l_m^2+\frac{512}{6237}\,l_m^3\Big)+n_l^2\left(\frac{667234795424}{1253204308125}-\frac{512}{891}\,\zeta_3\right.\\
&\left.+\frac{1213878224}{3978426375}\,l_m-\frac{1082216}{12629925}\,l_m^2+\frac{256}{6237}\,l_m^3\right)\\
C_5^0 \;=\;& \frac{1089264797862809}{114328101888000}-\frac{13766684598973}{1693749657600}\,\zeta_3+\frac{1239683}{1474560}\,l_m\,\zeta_3-\frac{9879141778777}{8136640512000}\,l_m\\
&-\frac{1064635136}{11345882625}\,l_m^2+\frac{1024}{27027}\,l_m^3+n_l\left(\frac{2680576384798219}{838813667328000}-\frac{1239683}{645120}\,a_4-\frac{1239683}{15482880}\,l_2^4\right.\\
&+\frac{1239683}{15482880}\,l_2^2\pi^2+\frac{8677781}{265420800}\pi^4-\frac{1942577613953}{398529331200}\,\zeta_3+\frac{1239683}{1474560}\,l_m\,\zeta_3\\
&\left.-\frac{580030100117579693}{644112110315520000}\,l_m-\frac{2129270272}{11345882625}\,l_m^2+\frac{2048}{27027}\,l_m^3\right)\\
&+n_l^2\left(\frac{61443753281463008}{136221219619340625}-\frac{2048}{3861}\,\zeta_3+\frac{160295587080064}{511075282843125}\,l_m-\frac{1064635136}{11345882625}\,l_m^2\right.\\
&\left.+\frac{1024}{27027}\,l_m^3\right) \qquad \text{(A.10)}
\end{aligned}
$$

where $l_m = \log(m(\mu)^2/\mu^2)$, $l_2 = \log(2)$, $a_i = \mathrm{Li}_i(1/2)$ with $\mathrm{Li}_i(x)$ the polylogarithm function and ζ_i the Riemann zeta numbers.

In the limit $z \to -\infty$ we obtain

$$
\begin{aligned}
C_0^\infty \;=\;& \frac{783389}{102060}-\frac{24349}{5670}\,\zeta_3-\frac{20}{9}\,\zeta_5+\frac{7}{24}\,\zeta_3\,l_{xm}-\frac{113}{324}\,l_{xm}-\frac{1}{27}\,l_{xm}^2+\frac{1}{27}\,l_{xm}^3+\frac{545}{216}\,l_{x\mu}\,\zeta_3\\
&-\frac{365}{108}\,l_{x\mu}-\frac{4}{9}\,l_{x\mu}^2\,\zeta_3+\frac{31}{54}\,l_{x\mu}^2-\frac{2}{27}\,l_{x\mu}^3-\frac{1}{9}\,l_{x\mu}\,l_{xm}^2+\frac{2}{27}\,l_{x\mu}\,l_{xm}+\frac{1}{9}\,l_{x\mu}^2\,l_{xm}\\
&+n_l\left(\frac{94735}{5832}-\frac{2855}{324}\,\zeta_3-\frac{49}{4320}\pi^4-\frac{40}{9}\,\zeta_5+\frac{2}{3}\,a_4+\frac{1}{36}\,l_2^4-\frac{1}{36}\pi^2\,l_2^2+\frac{7}{24}\,l_{xm}\,\zeta_3\right.\\
&-\frac{37}{324}\,l_{xm}-\frac{2}{27}\,l_{xm}^2+\frac{2}{27}\,l_{xm}^3+\frac{1153}{216}\,l_{x\mu}\,\zeta_3-\frac{793}{108}\,l_{x\mu}-\frac{8}{9}\,l_{x\mu}^2\,\zeta_3+\frac{31}{27}\,l_{x\mu}^2-\frac{4}{27}\,l_{x\mu}^3\\
&\left.-\frac{2}{9}\,l_{xm}^2\,l_{x\mu}+\frac{4}{27}\,l_{xm}\,l_{x\mu}+\frac{2}{9}\,l_{xm}\,l_{x\mu}^2\right)+n_l^2\left(\frac{22327}{2916}-\frac{358}{81}\,\zeta_3-\frac{20}{9}\,\zeta_5+\frac{19}{81}\,l_{xm}\right.\\
&-\frac{1}{27}\,l_{xm}^2+\frac{1}{27}\,l_{xm}^3+\frac{76}{27}\,l_{x\mu}\,\zeta_3-\frac{107}{27}\,l_{x\mu}-\frac{4}{9}\,l_{x\mu}^2\,\zeta_3+\frac{31}{54}\,l_{x\mu}^2-\frac{2}{27}\,l_{x\mu}^3-\frac{1}{9}\,l_{x\mu}\,l_{xm}^2\\
&\left.+\frac{2}{27}\,l_{x\mu}\,l_{xm}+\frac{1}{9}\,l_{x\mu}^2\,l_{xm}\right) \qquad \text{(A.11)}\\
C_1^\infty \;=\;& \frac{16681}{1944}-\frac{38}{9}\,\zeta_3+\frac{8}{3}\,\zeta_3\,l_{x\mu}-\frac{317}{54}\,l_{x\mu}+\frac{13}{18}\,l_{x\mu}^2-\frac{1}{9}\,l_{x\mu}^3+n_l\left(\frac{10921}{972}-4\,\zeta_3+\frac{8}{3}\,\zeta_3\,l_{x\mu}\right.\\
&\left.-\frac{221}{27}\,l_{x\mu}+\frac{13}{9}\,l_{x\mu}^2-\frac{2}{9}\,l_{x\mu}^3\right)+n_l^2\left(\frac{5161}{1944}+\frac{2}{9}\,\zeta_3-\frac{125}{54}\,l_{x\mu}+\frac{13}{18}\,l_{x\mu}^2-\frac{1}{9}\,l_{x\mu}^3\right) \qquad \text{(A.12)}\\
C_2^\infty \;=\;& -\frac{7633}{9720}-\frac{571}{1620}\,\zeta_3+\frac{20}{9}\,\zeta_5-\frac{23}{18}\,\zeta_3\,l_{xm}+\frac{6373}{3888}\,l_{xm}+\frac{355}{432}\,l_{xm}^2+\frac{23}{216}\,l_{xm}^3+\frac{1}{72}\,l_{xm}^4\\
&+\frac{44}{27}\,\zeta_3\,l_{x\mu}-\frac{1505}{1296}\,l_{x\mu}+\frac{1}{9}\,\zeta_3\,l_{x\mu}^2+\frac{1}{216}\,l_{x\mu}^2-\frac{23}{72}\,l_{x\mu}\,l_{xm}^2+\frac{1}{3}\,\zeta_3\,l_{x\mu}\,l_{xm}-\frac{101}{54}\,l_{x\mu}\,l_{xm}\\
&+\frac{7}{24}\,l_{x\mu}^2\,l_{xm}-\frac{1}{18}\,l_{x\mu}\,l_{xm}^3+\frac{1}{12}\,l_{x\mu}^2\,l_{xm}^2-\frac{1}{18}\,l_{x\mu}^3\,l_{xm}+n_l\left(-\frac{12733}{7776}+\frac{29}{324}\,\zeta_3+\frac{1}{45}\pi^4\right.\\
&+\frac{25}{9}\,\zeta_5-\frac{1}{2}\,\zeta_3\,l_{xm}+\frac{6113}{3888}\,l_{xm}+\frac{455}{432}\,l_{xm}^2+\frac{43}{216}\,l_{xm}^3+\frac{1}{36}\,l_{xm}^4+\frac{16}{27}\,\zeta_3\,l_{x\mu}-\frac{397}{324}\,l_{x\mu}\\
&\left.+\frac{2}{9}\,\zeta_3\,l_{x\mu}^2+\frac{1}{108}\,l_{x\mu}^2-\frac{43}{72}\,l_{x\mu}\,l_{xm}^2+\frac{1}{3}\,\zeta_3\,l_{x\mu}\,l_{xm}-\frac{257}{108}\,l_{x\mu}\,l_{xm}+\frac{7}{12}\,l_{x\mu}^2\,l_{xm}-\frac{1}{9}\,l_{x\mu}\,l_{xm}^3\right. \qquad \text{(A.13)}
\end{aligned}
$$

$$
\begin{aligned}
&+\frac{1}{6}\,l_{x\mu}^2\,l_{xm}^2-\frac{1}{9}\,l_{x\mu}^3\,l_{xm}\Big)+n_l^2\left(-\frac{233}{7776}+\frac{239}{162}\,\zeta_3-\frac{1}{90}\pi^4+\frac{5}{9}\,\zeta_5+\frac{7}{9}\,\zeta_3\,l_{xm}+\frac{89}{486}\,l_{xm}\right.\\
&+\frac{25}{108}\,l_{xm}^2+\frac{5}{54}\,l_{xm}^3+\frac{1}{72}\,l_{xm}^4-\frac{28}{27}\,\zeta_3\,l_{x\mu}-\frac{83}{1296}\,l_{x\mu}+\frac{1}{9}\,\zeta_3\,l_{x\mu}^2+\frac{1}{216}\,l_{x\mu}^2-\frac{5}{18}\,l_{x\mu}\,l_{xm}^2\\
&\left.-\frac{55}{108}\,l_{x\mu}\,l_{xm}+\frac{7}{24}\,l_{x\mu}^2\,l_{xm}-\frac{1}{18}\,l_{x\mu}\,l_{xm}^3+\frac{1}{12}\,l_{x\mu}^2\,l_{xm}^2-\frac{1}{18}\,l_{x\mu}^3\,l_{xm}\right) \qquad \text{(A.14)}
\end{aligned}
$$

$$
\begin{aligned}
C_3^\infty \;=\;& -\frac{205123}{1049760}-\frac{593}{2430}\,\zeta_3-\frac{5}{54}\,\zeta_3\,l_{xm}+\frac{15017}{23328}\,l_{xm}+\frac{325}{3888}\,l_{xm}^2-\frac{47}{5832}\,l_{xm}^3+\frac{1}{324}\,l_{xm}^4\\
&+\frac{35}{81}\,\zeta_3\,l_{x\mu}+\frac{7963}{8748}\,l_{x\mu}-\frac{227}{1944}\,l_{x\mu}^2+\frac{1}{36}\,l_{x\mu}^3-\frac{7}{486}\,l_{x\mu}\,l_{xm}^3+\frac{25}{648}\,l_{x\mu}^2\,l_{xm}^2-\frac{1}{36}\,l_{x\mu}^3\,l_{xm}\\
&-\frac{109}{1944}\,l_{x\mu}\,l_{xm}^2-\frac{1355}{1944}\,l_{x\mu}\,l_{xm}+\frac{283}{1944}\,l_{x\mu}^2\,l_{xm}+n_l\left(\frac{49255}{104976}-\frac{167}{162}\,\zeta_3+\frac{7}{1215}\pi^4\right.\\
&+\frac{16}{81}\,\zeta_3\,l_{xm}+\frac{4987}{3888}\,l_{xm}+\frac{3149}{11664}\,l_{xm}^2+\frac{175}{5832}\,l_{xm}^3+\frac{7}{972}\,l_{xm}^4+\frac{23}{81}\,l_{x\mu}\,\zeta_3+\frac{29663}{34992}\,l_{x\mu}\\
&-\frac{227}{972}\,l_{x\mu}^2+\frac{1}{18}\,l_{x\mu}^3-\frac{5}{162}\,l_{x\mu}\,l_{xm}^3+\frac{25}{324}\,l_{x\mu}^2\,l_{xm}^2-\frac{1}{18}\,l_{x\mu}^3\,l_{xm}-\frac{367}{1944}\,l_{x\mu}\,l_{xm}^2\\
&\left.-\frac{1597}{1458}\,l_{x\mu}\,l_{xm}+\frac{283}{972}\,l_{x\mu}^2\,l_{xm}\right)\\
&+n_l^2\left(\frac{9157}{209952}+\frac{53}{243}\,\zeta_3-\frac{4}{1215}\pi^4+\frac{59}{162}\,\zeta_3\,l_{xm}+\frac{5905}{23328}\,l_{xm}+\frac{709}{5832}\,l_{xm}^2+\frac{7}{243}\,l_{xm}^3\right.\\
&+\frac{1}{243}\,l_{xm}^4-\frac{4}{27}\,\zeta_3\,l_{x\mu}-\frac{2189}{34992}\,l_{x\mu}-\frac{227}{1944}\,l_{x\mu}^2+\frac{1}{36}\,l_{x\mu}^3-\frac{4}{243}\,l_{x\mu}\,l_{xm}^3+\frac{25}{648}\,l_{x\mu}^2\,l_{xm}^2\\
&\left.-\frac{1}{36}\,l_{x\mu}^3\,l_{xm}-\frac{43}{324}\,l_{x\mu}\,l_{xm}^2-\frac{2323}{5832}\,l_{x\mu}\,l_{xm}+\frac{283}{1944}\,l_{x\mu}^2\,l_{xm}\right) \qquad \text{(A.15)}
\end{aligned}
$$

$$
\begin{aligned}
C_4^\infty \;=\;& -\frac{35389447}{44789760}-\frac{227}{103680}\,\zeta_3-\frac{895}{1728}\,\zeta_3\,l_{xm}+\frac{2812987}{2985984}\,l_{xm}+\frac{125203}{248832}\,l_{xm}^2+\frac{4603}{62208}\,l_{xm}^3\\
&+\frac{487}{41472}\,l_{xm}^4+\frac{31}{64}\,\zeta_3\,l_{x\mu}+\frac{164053}{165888}\,l_{x\mu}-\frac{70553}{497664}\,l_{x\mu}^2+\frac{7}{288}\,l_{x\mu}^3-\frac{185}{5184}\,l_{x\mu}\,l_{xm}^3\\
&+\frac{229}{6912}\,l_{x\mu}^2\,l_{xm}^2-\frac{1}{48}\,l_{x\mu}^3\,l_{xm}-\frac{8501}{41472}\,l_{x\mu}\,l_{xm}^2-\frac{80177}{124416}\,l_{x\mu}\,l_{xm}+\frac{2279}{20736}\,l_{x\mu}^2\,l_{xm}\\
&+n_l\left(-\frac{19473727}{35831808}-\frac{27725}{20736}\,\zeta_3+\frac{43}{6480}\pi^4+\frac{271}{1728}\,\zeta_3\,l_{xm}+\frac{3637091}{2985984}\,l_{xm}+\frac{226123}{497664}\,l_{xm}^2\right.\\
&+\frac{11407}{124416}\,l_{xm}^3+\frac{19}{1296}\,l_{xm}^4+\frac{89}{192}\,l_{x\mu}\,\zeta_3+\frac{47029}{41472}\,l_{x\mu}-\frac{70553}{248832}\,l_{x\mu}^2+\frac{7}{144}\,l_{x\mu}^3\\
&-\frac{497}{10368}\,l_{x\mu}\,l_{xm}^3+\frac{229}{3456}\,l_{x\mu}^2\,l_{xm}^2-\frac{1}{24}\,l_{x\mu}^3\,l_{xm}-\frac{1673}{5184}\,l_{x\mu}\,l_{xm}^2-\frac{57629}{62208}\,l_{x\mu}\,l_{xm}\\
&\left.+\frac{2279}{10368}\,l_{x\mu}^2\,l_{xm}\right)+n_l^2\left(-\frac{3462161}{35831808}-\frac{745}{5184}\,\zeta_3-\frac{127}{51840}\pi^4+\frac{265}{864}\,\zeta_3\,l_{xm}+\frac{1097}{5832}\,l_{xm}\right.\\
&+\frac{51077}{497664}\,l_{xm}^2+\frac{2411}{124416}\,l_{xm}^3+\frac{127}{41472}\,l_{xm}^4-\frac{1}{48}\,\zeta_3\,l_{x\mu}+\frac{8021}{55296}\,l_{x\mu}-\frac{70553}{497664}\,l_{x\mu}^2\\
&+\frac{7}{288}\,l_{x\mu}^3-\frac{127}{10368}\,l_{x\mu}\,l_{xm}^3+\frac{229}{6912}\,l_{x\mu}^2\,l_{xm}^2-\frac{1}{48}\,l_{x\mu}^3\,l_{xm}-\frac{4883}{41472}\,l_{x\mu}\,l_{xm}^2\\
&\left.-\frac{35081}{124416}\,l_{x\mu}\,l_{xm}+\frac{2279}{20736}\,l_{x\mu}^2\,l_{xm}\right) \qquad \text{(A.16)}
\end{aligned}
$$

with $l_{x\mu} = \log(-p^2/\mu^2)$ and $l_{xm} = \log(-p^2/m(\mu)^2)$. Above, all occuring powers of logarithms are included and therefore the second index as given in eq. (A.7) is ommited. In fig. A.2-A.3 the exact result obtained from numerical integration is compared against the asymptotic behaviours of different expansion depths for Minkowskian momenta with

$m = \mu$. In both regimes, we find that already a moderate number of terms reproduces the exact curve very well, for the case of massless corrections ($\mathcal{O}(n_l^2)$) even close to threshold.

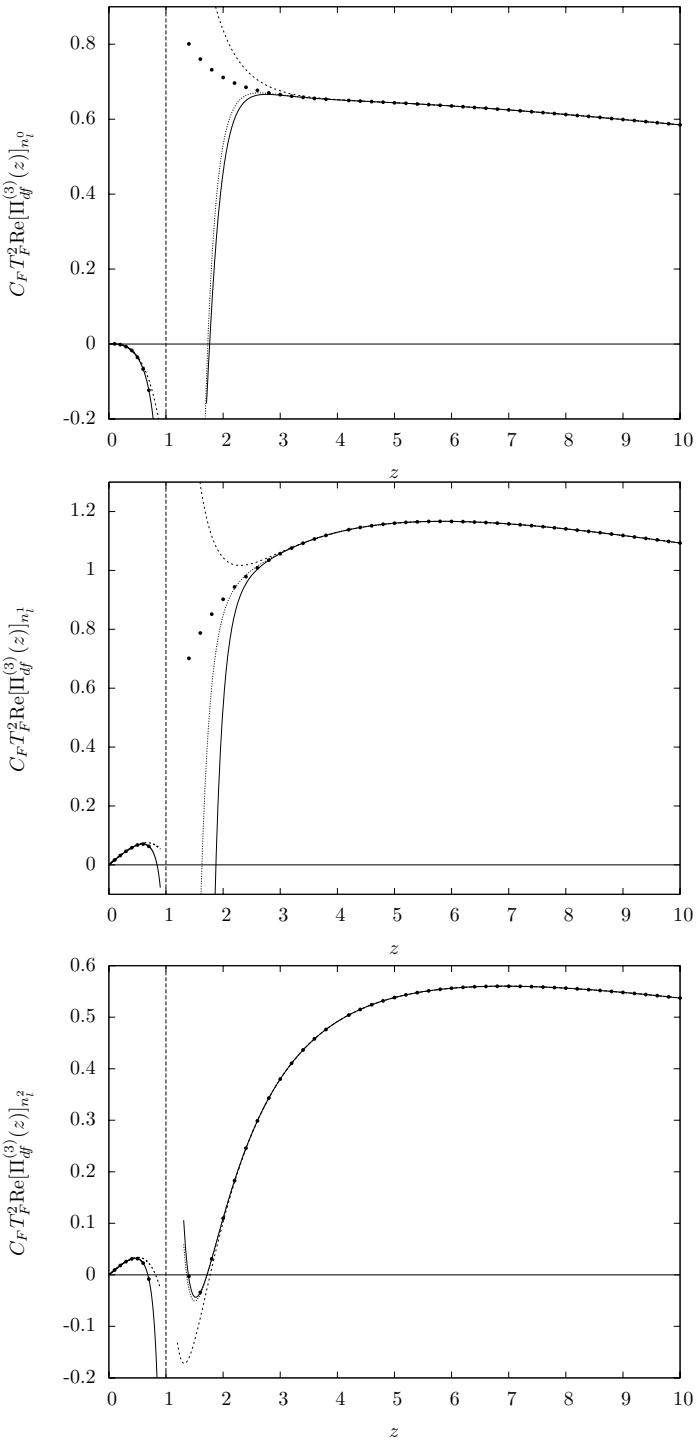

Figure A.2.: Comparison between numerics (dotted curve) and expansions of the real part of $C_F T^2 \Pi_{\mathrm{df}}^{(3)}(z)$ for each coefficient of n_l separately. Below threshold (represented by the vertical line in $z = 1$), the dashed (solid) curves correspond to low-energy expansions including the first 5 (30) terms. Above threshold the dashed, dash-dotted and solid lines denote the high-energy expansions including the first 5, 10 and 15 terms, respectively.

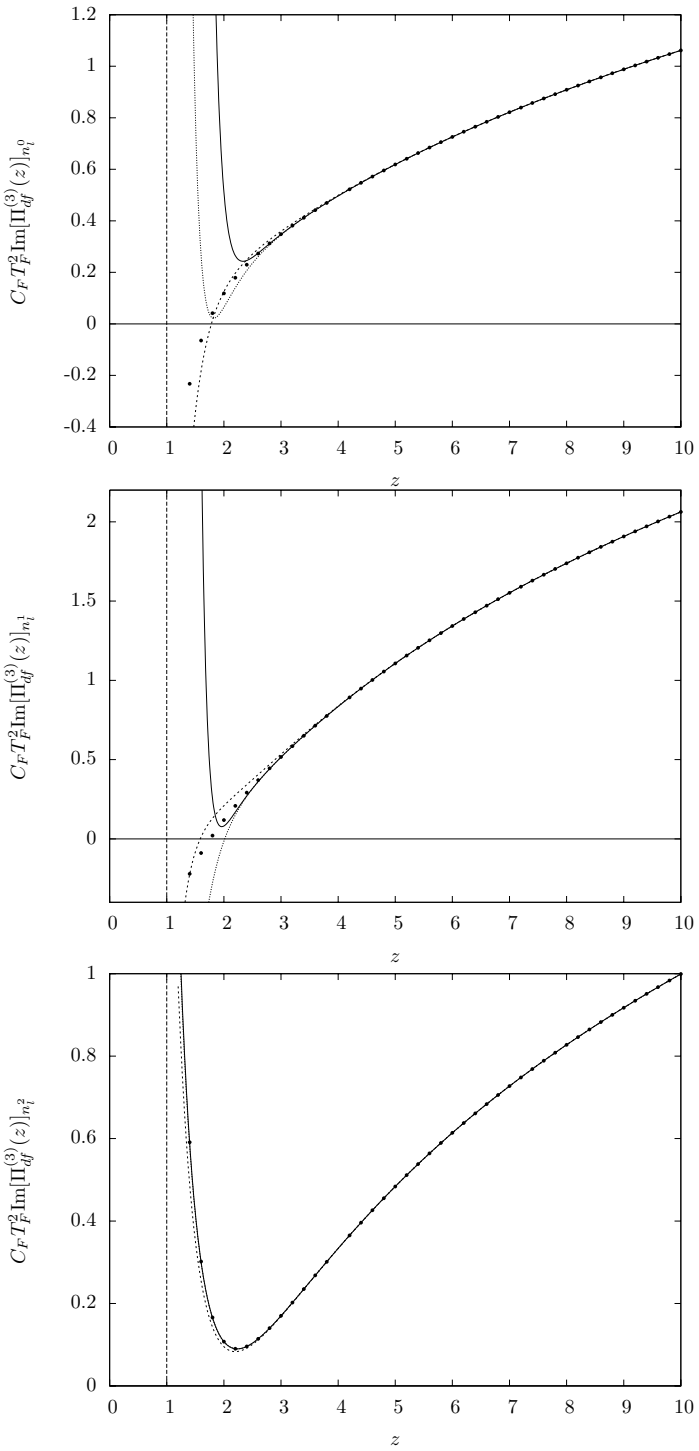

Figure A.3.: Comparison between numerics (dotted curve) and expansions of the imaginary part of $C_F T^2 \Pi_{\mathrm{df}}^{(3)}(z)$ for each coefficient of n_l separately. The dashed, dash-dotted and solid lines denote the high-energy expansions including the first 5, 10 and 15 terms, respectively.

B. List of input boundary integrals

In this appendix, explicit results for the boundary integrals are given, that are needed as input in the computations of this work. More specifically, the following results are required for diagrammatic asymptotic expansions and are either well known in the literature and were independently verified during this work or are computed from scratch. All expressions are given to the maximal needed power in ϵ, although not all powers may be required for every computation.

Vacuum integrals

All massive vacuum integrals appearing in the large-mass expansions in the $\overline{B} \to X_s\gamma$ calculations are shown in fig. B.1. The determination of the photon vacuum polarization requires additional 3- and 4-loop vacuum integrals depicted in fig. B.2. The normalization per loop is chosen as

$$\mathcal{N} = i\pi^{2-\epsilon}e^{-\gamma_E\epsilon} \tag{B.1}$$

We also set the renormalization scale to be equal to the internal mass, $\mu^2 = m^2$, since the μ dependence can easily be obtained with dimensional analysis.

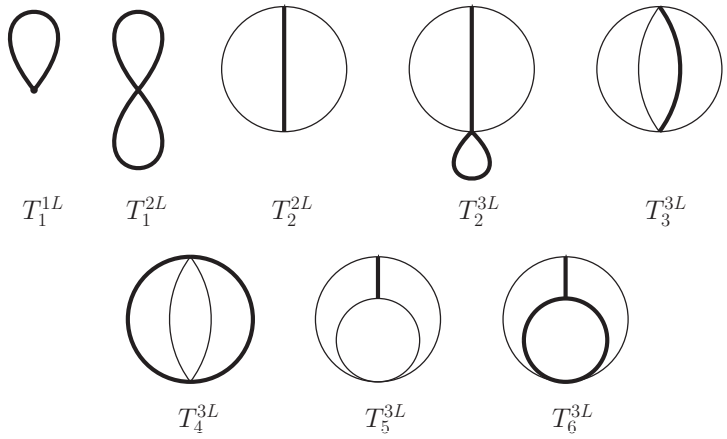

Figure B.1.: Vacuum diagrams appearing in the large mass expansions preformed in this work.

The one-loop tadpole result of T_1^1 is well known in literature to arbitrary powers in ϵ and reads

$$\frac{T_1^{1L}}{\mathcal{N}} = -\Gamma(1-\epsilon) \tag{B.2}$$

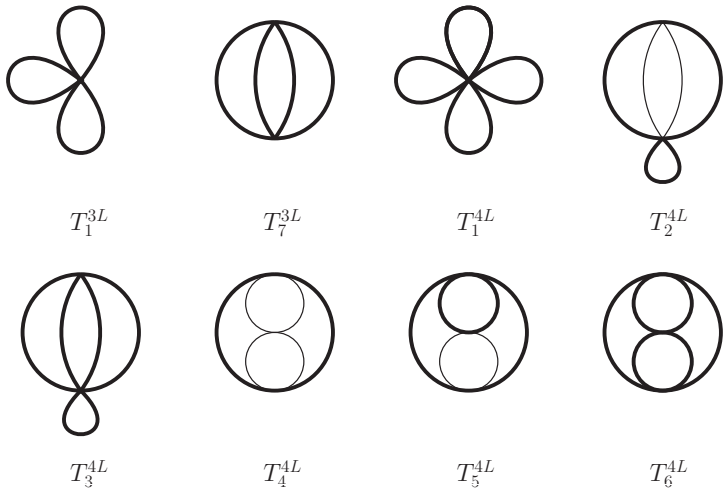

Figure B.2.: Vacuum integrals needed for the large-mass and large-momentum expansions of the photon vacuum polarization.

Therefore, diagrams T_1^{2L}, T_1^{3L} and T_1^{4L} are trivial to all powers in ϵ:

$$T_1^{2L} = (T_1^{1L})^2, \quad T_1^{3L} = (T_1^{1L})^3 \quad \text{and} \quad T_1^{4L} = (T_1^{1L})^4. \tag{B.3}$$

The remaining 1- to 3-loop integrals can be found in [154, 155], while the 4-loop diagrams were obtained in [130]. Explicitly, they are

$$\begin{aligned}
\frac{T_2^{2L}}{\mathcal{N}^2} &= \frac{1}{2\epsilon^2} + \frac{3}{2\epsilon} + \frac{7}{2} + \frac{3}{2}\,\zeta_2 + \epsilon\left(\frac{15}{2} + \frac{9}{2}\,\zeta_2 - \frac{4}{3}\,\zeta_3\right) + \epsilon^2\left(\frac{31}{2} + \frac{21}{2}\zeta_2 + \frac{63}{20}\zeta_2^2 - 4\zeta_3\right) \\
&\quad + \epsilon^3\left(\frac{63}{2} + \frac{45}{2}\,\zeta_2 - \frac{28}{3}\zeta_3 + \frac{189}{8}\zeta_4 - \frac{16}{5}\zeta_5 - 4\zeta_2\zeta_3\right) + \epsilon^4\left(\frac{127}{2} + \frac{93}{2}\,\zeta_2 - 20\zeta_3\right. \\
&\quad \left. + \frac{16}{9}\zeta_3^2 + \frac{441}{8}\zeta_4 - \frac{48}{5}\zeta_5 + \frac{869}{32}\zeta_6 - 12\zeta_2\zeta_3\right) + \mathcal{O}(\epsilon^5) \qquad \text{(B.4)} \\
\frac{T_2^{3L}}{\mathcal{N}^3} &= \frac{1}{2\epsilon^3} + \frac{2}{\epsilon^2} + \frac{1}{\epsilon}\left(\frac{11}{2} + \frac{7}{4}\,\zeta_2\right) + 13 + 7\,\zeta_2 - \frac{3}{2}\,\zeta_3 + \epsilon\left(\frac{57}{2} + \frac{77}{4}\,\zeta_2 - 6\,\zeta_3 + \frac{321}{32}\,\zeta_4\right) \\
&\quad + \epsilon^2\left(60 + \frac{91}{2}\,\zeta_2 - \frac{21}{4}\,\zeta_3\,\zeta_2 - \frac{33}{2}\,\zeta_3 + \frac{321}{8}\,\zeta_4 - \frac{33}{10}\,\zeta_5\right) + \epsilon^3\left(\frac{247}{2} + \frac{399}{4}\,\zeta_2\right. \\
&\quad \left. - 39\,\zeta_3 + \frac{9}{4}\,\zeta_3^2 - 21\,\zeta_2\,\zeta_3 + \frac{3531}{32}\,\zeta_4 - \frac{66}{5}\,\zeta_5 + \frac{9155}{256}\,\zeta_6\right) \qquad \text{(B.5)} \\
\frac{T_3^{3L}}{\mathcal{N}^3} &= -\frac{1}{12\epsilon^2} - \frac{5}{8\epsilon} - \frac{145}{48} - \frac{5}{8}\,\zeta_2 + \epsilon\left(-\frac{385}{32} - \frac{75}{16}\,\zeta_2 + \frac{11}{12}\,\zeta_3\right) + \epsilon^2\left(-\frac{8281}{192} - \frac{725}{32}\,\zeta_2\right. \\
&\quad \left. + \frac{55}{8}\,\zeta_3 - \frac{507}{64}\,\zeta_4\right) + \epsilon^3\left(-\frac{18585}{128} - \frac{5775}{64}\,\zeta_2 + \frac{1595}{48}\,\zeta_3 + \frac{55}{8}\,\zeta_3\,\zeta_2\right. \\
&\quad \left. - \frac{7605}{128}\,\zeta_4 + \frac{91}{20}\,\zeta_5\right) \qquad \text{(B.6)} \\
& \qquad \text{(B.7)}
\end{aligned}$$

$$\frac{T_4^{3L}}{\mathcal{N}^3} = \frac{1}{3\epsilon^3}+\frac{7}{6\epsilon^2}+\frac{1}{\epsilon}\left(\frac{25}{12}+\frac{1}{2}\,\zeta_2\right)+\frac{1}{24}(-5+42\,\zeta_2+56\,\zeta_3)+\epsilon\left(-\frac{959}{48}+\frac{25}{8}\,\zeta_2+\frac{49}{6}\,\zeta_3 -\frac{173}{16}\,\zeta_4\right)+\epsilon^2\left(-\frac{10493}{96}-\frac{5}{16}\,\zeta_2+\frac{25}{12}\,\zeta_3-\frac{1211}{32}\,\zeta_4+\frac{239}{5}\,\zeta_5+\frac{7}{2}\,\zeta_2\zeta_3\right) +\epsilon^3\left(-\frac{85175}{192}-\frac{959}{32}\,\zeta_2-\frac{35}{24}\,\zeta_3-\frac{4325}{64}\,\zeta_4-\frac{80585}{384}\,\zeta_6+\frac{1673}{10}\,\zeta_5+\frac{49}{6}\,\zeta_3^2 +\frac{49}{4}\,\zeta_3\,\zeta_2\right)+\mathcal{O}(\epsilon^4) \tag{B.8}$$

$$\frac{T_5^{3L}}{\mathcal{N}^3} = \frac{1}{3\epsilon^3}+\frac{5}{3\epsilon^2}+\frac{1}{\epsilon}\left(\frac{17}{3}+\frac{5}{2}\,\zeta_2\right)+\frac{49}{3}+\frac{25}{2}\,\zeta_2-\frac{5}{3}\,\zeta_3+\epsilon\left(43+\frac{85}{2}\,\zeta_2-\frac{25}{3}\,\zeta_3 +\frac{555}{16}\,\zeta_4\right)+\epsilon^2\left(107+\frac{245}{2}\,\zeta_2-\frac{85}{3}\,\zeta_3-\frac{25}{2}\,\zeta_3\,\zeta_2+\frac{2775}{16}\,\zeta_4-\frac{21}{5}\,\zeta_5\right) +\epsilon^3\left(\frac{769}{3}+\frac{645}{2}\,\zeta_2-\frac{245}{3}\,\zeta_3+\frac{25}{6}\,\zeta_3^2-\frac{125}{2}\,\zeta_2\,\zeta_3+\frac{9435}{16}\,\zeta_4-21\,\zeta_5+\frac{124555}{384}\,\zeta_6\right) \tag{B.9}$$

$$\frac{T_7^{3L}}{\mathcal{N}^3} = \frac{2}{\epsilon^3}+\frac{23}{3\epsilon^2}+\frac{1}{\epsilon}\left(\frac{35}{2}+3\,\zeta_2\right)+\frac{23}{2}\,\zeta_2+\frac{275}{12}-2\,\zeta_3+\epsilon\left(-\frac{189}{8}+\frac{105}{4}\,\zeta_2+\frac{89}{3}\,\zeta_3 +\frac{57}{8}\,\zeta_4\right)+\epsilon^2\left(-\frac{14917}{48}+256\,a_4+\frac{32}{4}\,L_2^4+\frac{275}{8}\,\zeta_2-64\,L_2^2\,\zeta_2+\frac{525}{2}\,\zeta_3-3\,\zeta_2\,\zeta_3 -\frac{3915}{16}\,\zeta_4-\frac{6}{5}\,\zeta_5\right)+\epsilon^3\left(-\frac{48005}{32}+1920\,a_4+1536\,a_5+80\,L_2^4-\frac{64}{5}\,L_2^5-\frac{567}{16}\,\zeta_2 -480\,L_2^2\,\zeta_2+128\,L_2^3\,\zeta_2+\frac{1}{4}\zeta_2^3+\frac{15965}{12}\,\zeta_3+\frac{89}{2}\,\zeta_2\,\zeta_3+\zeta_3^2-\frac{63285}{32}\,\zeta_4+1632\,L_2\,\zeta_4 +\frac{27}{8}\,\zeta_2\,\zeta_4-\frac{6223}{5}\,\zeta_5+\frac{183}{64}\,\zeta_6\right) +\mathcal{O}(\epsilon^4) \tag{B.10}$$

$$\frac{T_2^{4L}}{\mathcal{N}^4} = \frac{1}{\epsilon\epsilon^4}+\frac{3}{2\epsilon^3}+\frac{1}{\epsilon^2}\left(\frac{43}{12}+\frac{2}{3}\,\zeta_2\right)+\frac{1}{\epsilon^2}\left(\frac{27}{8}+3\,\zeta_2+\frac{20}{9}\,\zeta_3\right)-\frac{797}{48}+\frac{43}{6}\zeta_2+10\,\zeta_3 -10\,\zeta_4+\epsilon\left(-\frac{4029}{32}+\frac{27}{4}\,\zeta_2+\frac{215}{9}\,\zeta_3+\frac{40}{9}\,\zeta_2\zeta_3-45\,\zeta_4+\frac{716}{16}\,\zeta_5\right)+\epsilon^2\left(-\frac{109349}{192} -\frac{797}{24}\,\zeta_2+\frac{45}{2}\,\zeta_3+\frac{200}{27}\,\zeta_3^2+20\,\zeta_2\,\zeta_3-\frac{1787}{24}\,\zeta_2\,\zeta_4-\frac{215}{2}\,\zeta_4+\frac{1074}{5}\,\zeta_5-\frac{8483}{96}\,\zeta_6\right) \tag{B.11}$$

$$\frac{T_3^{4L}}{\mathcal{N}^4} = \frac{2}{\epsilon^4}+\frac{29}{3\epsilon^3}+\frac{1}{\epsilon^2}\left(\frac{163}{6}+4\,\zeta_2\right)+\frac{1}{\epsilon}\left(+\frac{601}{12}+\frac{58}{3}\,\zeta_2-\frac{8}{3}\zeta_3\right)+\frac{635}{24}+\frac{163}{3}\zeta_2+\frac{220}{9}\,\zeta_3 +12\,\zeta_4+\epsilon\left(-\frac{4549}{16}+\frac{32}{3}\,L_2^4+256\,a_4+\frac{601}{6}\zeta_2-64\zeta_2L_2^2+\frac{2530}{9}\zeta_3-\frac{16}{3}\zeta_2\zeta_3 -214\zeta_4-\frac{8\zeta_5}{5}\right)\epsilon^2\left(-\frac{57103}{32}+2176\,a_4+1536\,a_5+\frac{272}{3}\,L_2^4-\frac{64}{5}\,L_2^5+\frac{635}{12}\,\zeta_2 -544\zeta_2L_2^2+128\zeta_2L_2^3+\frac{14435}{9}\,\zeta_3+\frac{16}{9}\,\zeta_3^2-2149\zeta_4+1632\zeta_4L_2+\frac{440}{9}\zeta_2\zeta_3+\frac{27}{4}\zeta_2\zeta_4 -\frac{18716}{15}\,\zeta_5+\frac{131}{16}\,\zeta_6\right) \tag{B.12}$$

$$\frac{T_4^{4L}}{\mathcal{N}^4} = \frac{1}{6\epsilon^4}+\frac{5}{6\epsilon^3}+\frac{1}{\epsilon^2}\left(\frac{3}{2}+\frac{\zeta_2}{3}\right)+\frac{1}{\epsilon}\left(-\frac{13}{2}+\frac{5}{3}\,\zeta_2+\frac{55}{9}\,\zeta_3\right)-\frac{157}{2}+3\,\zeta_2+\frac{275}{9}\,\zeta_3 -\frac{67}{2}\,\zeta_4\epsilon\left(-\frac{989}{2}-13\,\zeta_2+55\,\zeta_3-\frac{335}{2}\,\zeta_4+\frac{3223}{15}\,\zeta_5+\frac{110}{9}\,\zeta_2\,\zeta_3\right) \tag{B.13}$$

$$\frac{T_5^{4L}}{\mathcal{N}^4} = \frac{2}{3\epsilon^4} + \frac{4}{\epsilon^3} + \frac{1}{\epsilon^2}\left(\frac{38}{3} + \frac{4}{3}\zeta_2\right) + \frac{1}{\epsilon}\left(\frac{44}{3} + 8\,\zeta_2 + \frac{40}{9}\zeta_3\right) + \left(-118 + \frac{76}{3}\,\zeta_2 + \frac{248}{3}\,\zeta_3 - 20\,\zeta_4\right) + N_1\epsilon + N_2\epsilon^2 \tag{B.14}$$

$$\frac{T_6^{4L}}{\mathcal{N}^4} = \frac{3}{2\epsilon^4} + \frac{19}{2\epsilon^3} + \frac{1}{\epsilon^2}\left(\frac{67}{2} + 3\zeta_2\right) + \frac{1}{\epsilon}\left(\frac{127}{2} + 19\,\zeta_2 - 5\,\zeta_3\right) - \frac{237}{2} + 67\,\zeta_2 + \frac{253}{3}\,\zeta_3 + \frac{9}{2}\,\zeta_4\epsilon\left(-\frac{3969}{2} + 768a_4 + 32L_2^4 + 127\,\zeta_2 - 192\,\zeta_2 L_2^2 + \frac{3649}{3}\,\zeta_3 - 10\,\zeta_2\,\zeta_3 - \frac{1563}{2}\,\zeta_4 + \frac{939}{5}\,\zeta_5\right) \tag{B.15}$$

with $L_2 = \log 2$, $L_3 = \log 3$, the Riemann zeta numbers ζ_i, $a_i = \mathrm{Li}_i(1/2)$ with $\mathrm{Li}_i(x)$ the polylogarithm function. The constants N_1 and N_2 are given by

$$N_1 = -764.0948373358558, \tag{B.16}$$

$$N_2 = -4647.352454831194. \tag{B.17}$$

One of the 3-loop vacuum integrals, T_6^{3L}, is known only numerically from one dimensional Mellin-Barnes representations, that can be evaluated to very high precision

$$\begin{aligned}\frac{T_6^{3L}}{\mathcal{N}^3} = {} & 0.66666666666666666666666666666666666667\,\frac{1}{\epsilon^3} \\ & +3.66666666666666666666666666666666666667\,\frac{1}{\epsilon^2} \\ & +13.77400727566226453704248689998363 48\,\frac{1}{\epsilon} \\ & +55.65962246120633017136139508642412 20 \\ & +151.93523620176745531459840301896170 8\,\epsilon \\ & +574.65405761296725286615112197885868 3\,\epsilon^2 \\ & +1417.68304294980808648159033431755539\,\epsilon^3\end{aligned} \tag{B.18}$$

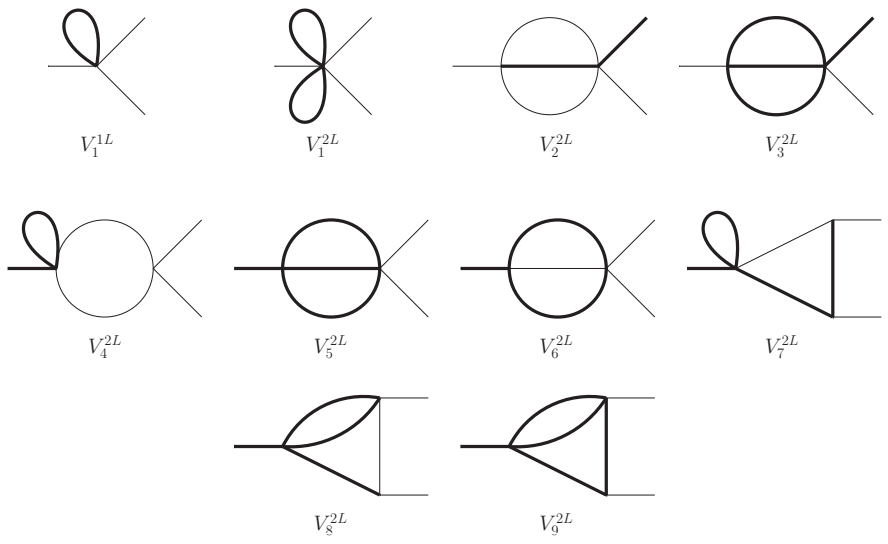

Figure B.3.: Vertex integrals needed for the large-mass expansion of chapter 3. Thin internal lines represent propagators of light mass, thick lines depict heavy particles.

Vertex Integrals

The large-mass expansion of chapter 3 requires vertex diagrams with both massive and massless internal and external lines. Fig. B.3 shows all needed diagrams. V_1^{1L} and V^{2L} are again trivial and are directly computed from T_1^{1L}. Moreover, all diagrams containing a vertex connected to a massive and a massless external simultaneously, V_2^{2L} and V_3^{2L}, are effectively vacuum integrals and can be identified with those in fig. B.1.
The results for diagrams that are known analytically read

$$V_1^{1L} = T_1^{1L} \tag{B.19}$$

$$V_1^{2L} = T_1^{2L} = (T_1^{1L})^2 \tag{B.20}$$

$$V_2^{2L} = T_2^{2L} \tag{B.21}$$

$$\frac{V_3^{2L}}{\mathcal{N}^2} = \frac{3}{2\epsilon^2} + \frac{17}{4\epsilon} + \frac{59}{8} + \frac{3}{2}\,\zeta_2 + \epsilon\left(\frac{65}{16} + \frac{49}{4}\,\zeta_2 - \zeta_3\right) + \epsilon^2\left(-\frac{1117}{32} + \frac{475}{8}\,\zeta_2 - 48L_2\,\zeta_2 + \frac{151}{6}\,\zeta_3 + \frac{21}{8}\,\zeta_4\right) \tag{B.22}$$

$$\frac{V_4^{2L}}{\mathcal{N}^2} = \frac{1}{\epsilon^2} + \frac{1}{\epsilon}\,(3 + i\pi) - 3\,\zeta_2 + 3i\pi + 7 + \epsilon\left(15 + 7i\pi - \frac{1}{6}i\pi^3 - 9\,\zeta_2 - \frac{8}{3}\,\zeta_3\right) + \epsilon^2\left(31 + 15i\pi - \frac{1}{2}i\pi^3 - 21\,\zeta_2 - 8\,\zeta_3 - \frac{8}{3}i\pi\,\zeta_3 + \frac{3}{4}\,\zeta_4\right) \tag{B.23}$$

*

$$\begin{aligned}\frac{V_6^{2L}}{\mathcal{N}^2} &= \frac{1}{\epsilon^2}+\frac{11}{4\epsilon}++\frac{35}{8}+\frac{1}{2}\pi s_3+\zeta_2+\epsilon\left(\frac{5}{16}+3P_1 s_3-\frac{3}{2}\pi L_3 s_3+\frac{13}{4}\pi s_3\right.\\ &\left.+\frac{11}{4}\,\zeta_2-\frac{2}{3}\,\zeta_3\right)+\epsilon^2\left(-\frac{1033}{32}+\frac{115}{8}\pi s_3-\frac{13}{30}\pi^3 s_3-\frac{39}{4}\pi s_3 L_3+\frac{9}{5}\pi s_3 L_3^2\right.\\ &\left.+\frac{39}{2}P_1 s_3+\frac{108}{5}P_2 s_3+\frac{35}{8}\,\zeta_2+\frac{1}{2}\pi s_3\,\zeta_2-\frac{11}{6}\,\zeta_3+\frac{7}{4}\,\zeta_4\right) \qquad \text{(B.24)}\\ \frac{V_7^{2L}}{\mathcal{N}^2} &= -\frac{1}{\epsilon}\,\zeta_2-\,\zeta_2-3\,\zeta_3+\epsilon\left(-\,\zeta_2-3\,\zeta_3-\frac{19}{2}\,\zeta_4\right)\epsilon^2\left(-\,\zeta_2-3\,\zeta_3-\frac{7}{3}\,\zeta_2\,\zeta_3\right.\\ &\left.-\frac{19}{2}\,\zeta_4-15\,\zeta_5\right) \qquad \text{(B.25)}\end{aligned}$$

Here, $s_3=\sqrt{3}$, $P_1=\mathrm{Im}\,\mathrm{Li}_2[\exp(i\pi/3)]$ and $P_2=\mathrm{Im}\,\mathrm{Li}_3[i/\sqrt{3})]$.
The remaining integrals could only be obtained numerically with sufficient high precision and are given by

$$\begin{aligned}\frac{V_5^{2L}}{\mathcal{N}^2} &= 1.50000000000000000000000000000000000\,\frac{1}{\epsilon^2}\\ &+4.50000000000000000000000000000000000\,\frac{1}{\epsilon}\\ &+9.45154024223815131880627931666062218\\ &+24.20892802120359267872133821957094 89\,\frac{1}{\epsilon}\\ &+38.71759974491583887231661364177794 37\,\frac{1}{\epsilon^2} \qquad \text{(B.26)}\\ \frac{V_8^{2L}}{\mathcal{N}^2} &= 0.500000000000000\,\frac{1}{\epsilon^2}+1.50000000000000\,\frac{1}{\epsilon}\\ &+0.918353227104925+4.96170897120704\,\epsilon\\ &-2.82314724393821\,\epsilon^2 \qquad \text{(B.27)}\\ \frac{V_9^{2L}}{\mathcal{N}^2} &= 0.5000000000000000000\,\frac{1}{\epsilon^2}+0.5000000000000000000\,\frac{1}{\epsilon}\\ &+0.2355853539121758403+1.634395369496368519\,\epsilon \qquad \text{(B.28)}\end{aligned}$$

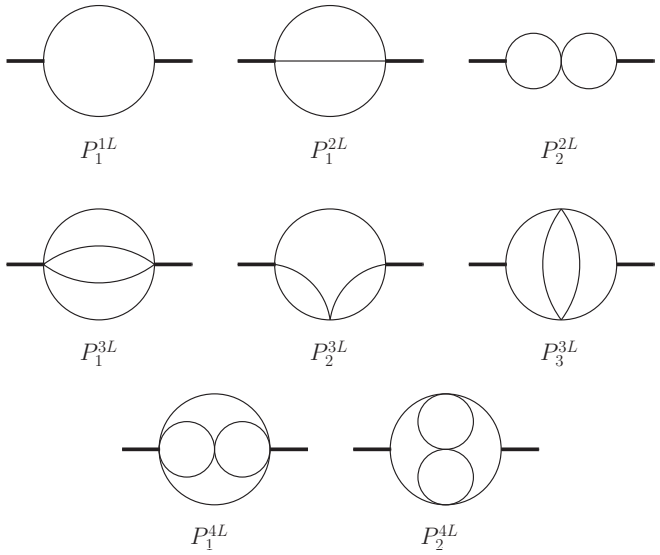

Figure B.4.: Massless propagator-type integrals required for the computation of the photon vacuum polarization.

Massless Propagators

In the computation of the large-momentum expansion of the vacuum polarisation, the massless propagators of fig. B are needed. While P_1^{1L} to P_3^{3L} are all known, the last two diagrams have been evaluated with both the help of Mellin Barnes representations and successive integration of massless subloops. In the second approach, one is left with the most complicated 2-loop propagator that has been extensively studied in the literature. The one-loop diagram P_1^{1L} can be found in literature to all orders in ϵ and is given by

$$\frac{P_1^{1L}}{\mathcal{N}} = \frac{\Gamma(1-\epsilon)^2\Gamma(\epsilon)}{\Gamma(2-2\epsilon)} \tag{B.29}$$

and therefore, P_2^{2L} is also known to all orders

$$P_2^{2L} = (P_1^{1L})^2. \tag{B.30}$$

Here, the renormalization scale is set to be equal to the kinematical invariant, $\mu^2 = p^2$. The remaining diagrams read

$$\frac{P_1^{2L}}{\mathcal{N}^2} = \frac{1}{4\epsilon} + \frac{13}{8} + \epsilon\left(\frac{115}{16} - \frac{1}{4}\,\zeta_2\right) + \epsilon^2\left(\frac{865}{32} - \frac{13}{8}\zeta_2 - \frac{8}{3}\,\zeta_3\right)\epsilon^3\left(\frac{5971}{64} - \frac{115}{16}\,\zeta_2\right.$$

$$-\frac{52}{3}\,\zeta_3-\frac{57}{16}\zeta_4\Big)+\epsilon^4\left(\frac{39193}{128}-\frac{865}{32}\,\zeta_2-\frac{230}{3}\,\zeta_3+\frac{8}{3}\,\zeta_3\,\zeta_2-\frac{741}{32}\,\zeta_4\right.$$
$$\left.-\frac{68}{5}\,\zeta_5\right)+\epsilon^5\left(\frac{249355}{256}-\frac{5971}{64}\,\zeta_2-\frac{865}{3}\,\zeta_3+\frac{128}{9}\,\zeta_3^2+\frac{52}{3}\,\zeta_2\,\zeta_3-\frac{6555}{64}\,\zeta_4\right.$$
$$\left.-\frac{442}{5}\,\zeta_5-\frac{57749}{4032}\,\zeta_6\right) \tag{B.31}$$

$$\frac{P_1^{3L}}{\mathcal{N}^3} = \frac{1}{36\epsilon}+\frac{71}{216}+\epsilon\left(\frac{3115}{1296}-\frac{1}{24}\,\zeta_2\right)+\epsilon^2\left(\frac{109403}{7776}-\frac{71}{144}\,\zeta_2-\frac{29}{36}\,\zeta_3\right)$$
$$\epsilon^3\left(\frac{3386467}{46656}--\frac{3115}{864}\,\zeta_2-\frac{2059}{216}\,\zeta_3-\frac{71}{64}\,\zeta_4\right)+\epsilon^4\left(\frac{96885467}{279936}-\frac{109403}{5184}\,\zeta_2\right.$$
$$\left.-\frac{90335}{1296}\,\zeta_3+\frac{29}{24}\,\zeta_3\,\zeta_2-\frac{5041}{384}\,\zeta_4-\frac{421}{60}\,\zeta_5\right) \tag{B.32}$$

$$\frac{P_2^{3L}}{\mathcal{N}^3} = \frac{1}{3\epsilon^2}+\frac{10}{3\epsilon}+\frac{64}{3}-\frac{1}{2}\,\zeta_2+\epsilon\left(112-5\,\zeta_2-\frac{23}{3}\,\zeta_3\right)+\epsilon^2\left(528-32\,\zeta_2-\frac{230}{3}\,\zeta_3\right.$$
$$\left.-\frac{165}{16}\,\zeta_4\right)+\epsilon^3\left(2336-168\,\zeta_2-\frac{1472}{3}\,\zeta_3+\frac{23}{2}\,\zeta_3\,\zeta_2-\frac{825}{8}\,\zeta_4-\frac{351}{5}\,\zeta_5\right)$$
$$+\epsilon^4\left(\frac{29824}{3}-792\,\zeta_2-2576\,\zeta_3+\frac{529}{6}\,\zeta_3^2+115\,\zeta_2\,\zeta_3-660\,\zeta_4-702\,\zeta_5\right.$$
$$\left.-\frac{2115557}{24192}\,\zeta_6\right) \tag{B.33}$$

$$\frac{P_3^{3L}}{\mathcal{N}^3} = \frac{1}{3\epsilon^3}+\frac{7}{3\epsilon^2}+\frac{1}{\epsilon}\left(\frac{31}{3}-\frac{1}{2}\,\zeta_2\right)+\frac{103}{3}-\frac{7}{2}\,\zeta_2+\frac{7}{3}\,\zeta_3+\epsilon\left(\frac{235}{3}-\frac{31}{2}\,\zeta_2\right.$$
$$\left.+\frac{49}{3}\,\zeta_3+\frac{75}{16}\,\zeta_4\right)+\epsilon^2\left(\frac{19}{3}-\frac{103}{2}\,\zeta_2+\frac{289}{3}\,\zeta_3-\frac{7}{2}\,\zeta_3\,\zeta_2+\frac{525}{16}\,\zeta_4\right.$$
$$\left.+\frac{599}{5}\,\zeta_5\right)\epsilon^3\left(-\frac{3953}{3}-\frac{235}{2}\,\zeta_2+\frac{1729}{3}\,\zeta_3-\frac{599}{6}\,\zeta_3^2-\frac{49}{2}\,\zeta_2\,\zeta_3\right.$$
$$\left.+\frac{2901}{16}\,\zeta_4+\frac{4193}{5}\,\zeta_5+\frac{4664683}{24192}\,\zeta_6\right) \tag{B.34}$$

$$\frac{P_1^{4L}}{\mathcal{N}^4} = \frac{1}{6\epsilon^4}+\frac{5}{3\epsilon^3}+\frac{1}{\epsilon^2}\left(\frac{29}{3}-\frac{1}{3}\zeta_2\right)+\frac{1}{\epsilon}\left(37-\frac{10}{3}\zeta_2+\frac{79}{9}\zeta_3\right)$$
$$+49-\frac{58}{3}\zeta_2+\frac{790}{9}\zeta_3+\frac{85}{6}\zeta_4 \tag{B.35}$$

$$\frac{P_2^{4L}}{\mathcal{N}^4} = \frac{1}{24\epsilon^2}+\frac{97}{144\epsilon}+\frac{5659}{864}-\frac{1}{12}\,\zeta_2+\epsilon\left(\frac{259549}{5184}-\frac{97}{72}\,\zeta_2-\frac{83}{36}\,\zeta_3\right)$$
$$+\epsilon^2\left(\frac{10365091}{31104}-\frac{5659}{432}\,\zeta_2-\frac{8051}{216}\,\zeta_3-\frac{77}{24}\,\zeta_4\right) \tag{B.36}$$

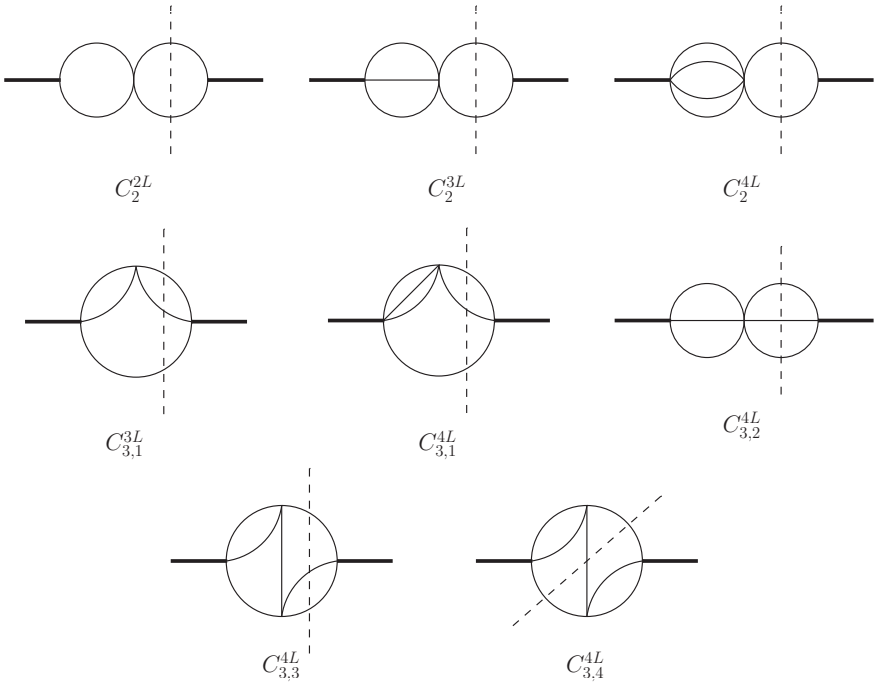

Figure B.5.: Massless cut propagator-type integrals needed in the large-mass expansion of chapter 3.2.

Massless Cut Propagators

The large mass expansion of chapter 3.2 requires the knowledge of eight massless cut propagators, given by the diagrams in fig. B.5. The integrals containing two particles in the final state can easily be obtained from the results of eqn. (B.31) - (B.36) by multiplication with the massless 2-particle phase space of equation (5.9) and are given by

$$C_2^{2L} = \Pi_2 \, P_1^{1L}, \tag{B.37}$$
$$C_2^{3L} = \Pi_2 \, P_1^{2L}, \tag{B.38}$$
$$C_2^{4L} = \Pi_2 \, P_1^{3L}. \tag{B.39}$$

The diagrams with three particles in the cut can be obtained by integrating out the massless loops and performing the phase-space integration analytically. The differential massless three particle phase-space in d dimensions,

$$\begin{aligned} d\Pi_3 &= \frac{1}{32}(2\pi)^{3-2d} 2^{4-d} \left(\frac{p^2}{\mu^2}\right)^{d-3} d\Omega_{d-2} \, d\Omega_{d-3} \, d\rho \\ d\rho &= (y_1 \, y_2 \, y_3)^{d/2-2} dy_1 \, dy_2 \, dy_3 \Theta(y_1) \, \Theta(y_2) \, \Theta(y_3) \, \delta(1 - y_1 - y_2 - y_3), \end{aligned} \tag{B.40}$$

where $y_1 = 2p_1p_2/p^2$, $y_2 = 2p_2p_3/p^2$, $y_3 = 2p_1p_3/p^2$ and $d\Omega_n$ is the n-dimensional differential surface element.

The results for $C^j_{3,i}$ are explicitely given by

$$\begin{aligned}
\frac{C^{3L}_{3,1}}{\mathcal{N}^3\Pi_3} &= \frac{1}{\epsilon}+\frac{7}{2}-i\pi+\left(-\frac{11}{2}\zeta_2-\frac{7}{2}i\pi+\frac{25}{2}\right)\epsilon+\left(46-\frac{77}{4}\zeta_2-\frac{37}{3}\zeta_3+\frac{7}{12}i\pi^3\right.\\
&\left.-\frac{25}{2}i\pi\right)\epsilon^2+\left(174-\frac{275}{4}\zeta_2+\frac{37}{3}i\pi\zeta_3-\frac{259}{6}\zeta_3-\frac{207}{16}\zeta_4+\frac{49}{24}i\pi^3\right.\\
&\left.-46i\pi\right)\epsilon^3+\left(\frac{407}{6}\zeta_3\zeta_2-253\zeta_2+\frac{259}{6}i\pi\zeta_3-\frac{925}{6}\zeta_3-\frac{1449}{32}\zeta_4-\frac{781}{5}\zeta_5+\right.\\
&\left.\frac{91}{288}i\pi^5+\frac{175}{24}i\pi^3-174i\pi+672\right)\epsilon^4 \qquad \text{(B.41)}\\
\frac{C^{4L}_{3,1}}{\mathcal{N}^4\Pi_3} &= -\frac{1}{12\epsilon}-\frac{1}{6}i\pi-\frac{49}{72}+\left(\frac{17}{12}\zeta_2-\frac{49}{36}i\pi-\frac{1723}{432}\right)\epsilon+\left(\frac{833}{72}\zeta_2+\frac{26}{9}\zeta_3+\frac{1}{4}i\pi^3\right.\\
&\left.-\frac{1723}{216}i\pi-\frac{54301}{2592}\right)\epsilon^2+\left(\frac{29291}{432}\zeta_2+\frac{52}{9}i\pi\zeta_3+\frac{637}{27}\zeta_3-\frac{439}{48}\zeta_4+\frac{49}{24}i\pi^3\right.\\
&\left.-\frac{54301}{1296}i\pi-\frac{1645987}{15552}\right)\epsilon^3+\left(-\frac{442}{9}\zeta_3\zeta_2+\frac{923117}{2592}\zeta_2+\frac{1274}{27}i\pi\zeta_3\right.\\
&\left.+\frac{22399}{162}\zeta_3-\frac{21511}{288}\zeta_4+\frac{728}{15}\zeta_5+\frac{17}{240}i\pi^5+\frac{1723}{144}i\pi^3-\frac{1645987}{7776}i\pi\right.\\
&\left.-\frac{49287469}{93312}\right)\epsilon^4 \qquad \text{(B.42)}\\
\frac{C^{4L}_{3,2}}{\mathcal{N}^4\Pi_3} &= -\frac{1}{4\epsilon}-\frac{1}{2}i\pi-\frac{13}{8}+\left(\frac{13}{4}\zeta_2-\frac{13}{4}i\pi-\frac{115}{16}\right)\epsilon+\left(\frac{169}{8}\zeta_2+\frac{8}{3}\zeta_3+\frac{5}{12}i\pi^3\right.\\
&\left.-\frac{115}{8}i\pi-\frac{865}{32}\right)\epsilon^2+\left(\frac{1495}{16}\zeta_2+\frac{16}{3}i\pi\zeta_3+\frac{52}{3}\zeta_3-\frac{303}{16}\zeta_4+\frac{65}{24}i\pi^3\right.\\
&\left.-\frac{865}{16}i\pi-\frac{5971}{64}\right)\epsilon^3+\left(-\frac{104}{3}\zeta_3\zeta_2+\frac{11245}{32}\zeta_2+\frac{104}{3}i\pi\zeta_3+\frac{230}{3}\zeta_3\right.\\
&\left.-\frac{3939}{32}\zeta_4+\frac{68}{5}\zeta_5-\frac{31}{720}i\pi^5+\frac{575}{48}i\pi^3-\frac{5971}{32}i\pi-\frac{39193}{128}\right)\epsilon^4 \qquad \text{(B.43)}\\
\frac{C^{4L}_{3,3}}{\mathcal{N}^4\Pi_3} &= 0.50000000000000000000000000\,\frac{1}{\epsilon^2}\\
&+4.00000000000000000000000000\,\frac{1}{\epsilon}\\
&+17.49273076603120747234655\\
&+57.91599534069470480792749\,\epsilon\\
&+161.5789101294171582566616\,\epsilon^2\\
&+410.0079838980296333685483\,\epsilon^3\\
&+977.9567977676448636824944\,\epsilon^4 \qquad \text{(B.44)}
\end{aligned}$$

$$\frac{C_{4,3}^{4L}}{\mathcal{N}^4\Pi_3} = \frac{1}{\epsilon^2}+\frac{7}{\epsilon}-6\zeta_2+\frac{77}{2}+\left(-42\zeta_2-\frac{98}{3}\zeta_3+\frac{789}{4}\right)\epsilon\left(-231\zeta_2-\frac{686}{3}\zeta_3-90\zeta_4 + \frac{7905}{8}\right)\epsilon^2+\left(196\zeta_3\zeta_2-\frac{2367}{2}\zeta_2-\frac{3773}{3}\zeta_3-630\zeta_4-\frac{2882}{5}\zeta_5+\frac{78741}{16}\right)\epsilon^3 + \left(\frac{4802}{9}\zeta_3^2+1372\zeta_2\zeta_3-\frac{12887}{2}\zeta_3-\frac{23715}{4}\zeta_2-3465\zeta_4-\frac{20174}{5}\zeta_5 -1222\zeta_6+\frac{784073}{32}\right)\epsilon^4 \tag{B.45}$$

The integral $C_{3,3}^{4L}$ requires the evaluation of a two-dimensional Mellin Barnes integration and was obtained numerically to a high precision with the package `quadprec` [156].

Bibliography

[1] S. L. Glashow. Partial Symmetries of Weak Interactions. *Nucl. Phys.*, 22:579–588, 1961.

[2] Steven Weinberg. A Model of Leptons. *Phys. Rev. Lett.*, 19:1264–1266, 1967.

[3] Murray Gell-Mann. A Schematic Model of Baryons and Mesons. *Phys. Lett.*, 8:214–215, 1964.

[4] H. Fritzsch, Murray Gell-Mann, and H. Leutwyler. Advantages of the Color Octet Gluon Picture. *Phys. Lett.*, B47:365–368, 1973.

[5] D. J. Gross and Frank Wilczek. Ultraviolet behavior of non-abelian gauge theories. *Phys. Rev. Lett.*, 30:1343–1346, 1973.

[6] H. David Politzer. Reliable perturbative results for strong interactions? *Phys. Rev. Lett.*, 30:1346–1349, 1973.

[7] Peter W. Higgs. Broken symmetries and the masses of gauge bosons. *Phys. Rev. Lett.*, 13:508–509, 1964.

[8] G. S. Guralnik, C. R. Hagen, and T. W. B. Kibble. Global conservation laws and massless particles. *Phys. Rev. Lett.*, 13:585–587, 1964.

[9] F. Englert and R. Brout. Broken symmetry and the mass of gauge vector mesons. *Phys. Rev. Lett.*, 13:321–322, 1964.

[10] Peter W. Higgs. Spontaneous Symmetry Breakdown without Massless Bosons. *Phys. Rev.*, 145:1156–1163, 1966.

[11] T. W. B. Kibble. Symmetry breaking in non-Abelian gauge theories. *Phys. Rev.*, 155:1554–1561, 1967.

[12] Gerard 't Hooft. Renormalization of Massless Yang-Mills Fields. *Nucl. Phys.*, B33:173–199, 1971.

[13] Gerard 't Hooft. Renormalizable lagrangians for massive yang-mills fields. *Nucl. Phys.*, B35:167–188, 1971.

[14] F. J. Hasert et al. Search for elastic muon neutrino electron scattering. *Phys. Lett.*, B46:121–124, 1973.

[15] F. J. Hasert et al. Observation of neutrino-like interactions without muon or electron in the Gargamelle neutrino experiment. *Phys. Lett.*, B46:138–140, 1973.

[16] T. Eichten et al. Measurement of the neutrino - nucleon anti-neutrino - nucleon total cross-sections. *Phys. Lett.*, B46:274–280, 1973.

[17] G. Arnison et al. Experimental observation of isolated large transverse energy electrons with associated missing energy at s**(1/2) = 540-GeV. *Phys. Lett.*, B122:103–116, 1983.

[18] G. Arnison et al. Experimental observation of lepton pairs of invariant mass around 95-GeV/c**2 at the CERN SPS collider. *Phys. Lett.*, B126:398–410, 1983.

[19] M. Banner et al. Observation of single isolated electrons of high transverse momentum in events with missing transverse energy at the CERN anti-p p collider. *Phys. Lett.*, B122:476–485, 1983.

[20] P. Bagnaia et al. Evidence for Z0 → e+ e- at the CERN anti-p p collider. *Phys. Lett.*, B129:130–140, 1983.

[21] The LEP Collaborations (ALEPH DELPHI L3 OPAL), LEP Electroweak Working Group, and SLD Heavy Flavour Group. A combination of preliminary Electroweak measurements and constraints on the Standard Model. *http://lepewwg.web.cern.ch/LEPEWWG.*

[22] Partice Data Group. .

[23] J. van der Bij and M. J. G. Veltman. Two Loop Large Higgs Mass Correction to the rho Parameter. *Nucl. Phys.*, B231:205, 1984.

[24] J. J. van der Bij, K. G. Chetyrkin, M. Faisst, G. Jikia, and T. Seidensticker. Three-loop leading top mass contributions to the rho parameter. *Phys. Lett.*, B498:156–162, 2001.

[25] Giuseppe Degrassi and Paolo Gambino. Two-loop heavy top corrections to the Z0 boson partial widths. *Nucl. Phys.*, B567:3–31, 2000.

[26] M. Faisst, Johann H. Kuhn, T. Seidensticker, and O. Veretin. Three loop top quark contributions to the rho parameter. *Nucl. Phys.*, B665:649–662, 2003.

[27] R. Boughezal, J. B. Tausk, and J. J. van der Bij. Three-loop electroweak correction to the rho parameter in the large Higgs mass limit. *Nucl. Phys.*, B713:278–290, 2005.

[28] M. Awramik, M. Czakon, A. Freitas, and G. Weiglein. Complete two-loop electroweak fermionic corrections to $\sin^2\theta^{\rm lept}_{\rm eff}$ and indirect determination of the Higgs boson mass. *Phys. Rev. Lett.*, 93:201805, 2004.

[29] A. Czarnecki. Muon g-2: A theoretical review. *Nucl. Phys. Proc. Suppl.*, 144:201–205, 2005.

[30] F. Abe et al. Observation of top quark production in $\bar{p}p$ collisions. *Phys. Rev. Lett.*, 74:2626–2631, 1995.

[31] S. Abachi et al. Observation of the top quark. *Phys. Rev. Lett.*, 74:2632–2637, 1995.

[32] M. J. G. Veltman. The Infrared - Ultraviolet Connection. *Acta Phys. Polon.*, B12:437, 1981.

[33] Steven Weinberg. Gauge Hierarchies. *Phys. Lett.*, B82:387, 1979.

[34] F. Zwicky. On the Masses of Nebulae and of Clusters of Nebulae. *Astrophys. J.*, 86:217–246, 1937.

[35] D. N. Spergel et al. First Year Wilkinson Microwave Anisotropy Probe (WMAP) Observations: Determination of Cosmological Parameters. *Astrophys. J. Suppl.*, 148:175–194, 2003.

[36] B. Aubert et al. The BaBar detector. *Nucl. Instrum. Meth.*, A479:1–116, 2002.

[37] The Belle detector. *Nucl. Instrum. Meth.*, A479:117–232, 2002.

[38] Makoto Kobayashi and Toshihide Maskawa. CP Violation in the Renormalizable Theory of Weak Interaction. *Prog. Theor. Phys.*, 49:652–657, 1973.

[39] R. Ammar et al. Evidence for penguins: First observation of B $\rightarrow$ K* (892) gamma. *Phys. Rev. Lett.*, 71:674–678, 1993.

[40] E. Barberio et al. Averages of $b-$hadron and $c-$hadron Properties at the End of 2007. 2008.

[41] S. Chen et al. Branching fraction and photon energy spectrum for b $\rightarrow$ s gamma. *Phys. Rev. Lett.*, 87:251807, 2001.

[42] K. Abe et al. A measurement of the branching fraction for the inclusive B $\rightarrow$ X/s gamma decays with Belle. *Phys. Lett.*, B511:151–158, 2001.

[43] B. Aubert et al. Measurements of the $B \rightarrow X_s\gamma$ branching fraction and photon spectrum from a sum of exclusive final states. *Phys. Rev.*, D72:052004, 2005.

[44] B. Aubert et al. Measurement of the branching fraction and photon energy moments of $B \rightarrow X_s\gamma$ and $B \rightarrow$ X(s+d) γ. *Phys. Rev. Lett.*, 97:171803, 2006.

[45] B. Aubert et al. Measurement of the $B \rightarrow X_s$ gamma Branching Fraction and Photon Energy Spectrum using the Recoil Method. *Phys. Rev.*, D77:051103, 2008.

[46] M. Bona et al. SuperB: A High-Luminosity Asymmetric e^+e^- Super Flavor Factory. Conceptual Design Report. 2007.

[47] S. Heinemeyer, W. Hollik, and G. Weiglein. FeynHiggs: a program for the calculation of the masses of the neutral CP-even Higgs bosons in the MSSM. *Comput. Phys. Commun.*, 124:76–89, 2000.

[48] Andre H. Hoang and Aneesh V. Manohar. Charm Quark Mass from Inclusive Semileptonic B Decays. *Phys. Lett.*, B633:526–532, 2006.

[49] Paolo Ciafaloni, Andrea Romanino, and Alessandro Strumia. Two-loop QCD corrections to charged-Higgs-mediated b → s gamma decay. *Nucl. Phys.*, B524:361–376, 1998.

[50] Marco Ciuchini, G. Degrassi, P. Gambino, and G. F. Giudice. Next-to-leading QCD corrections to B → X/s gamma: Standard model and two-Higgs doublet model. *Nucl. Phys.*, B527:21–43, 1998.

[51] Francesca Borzumati and Christoph Greub. 2HDMs predictions for anti-B → X/s gamma in NLO QCD. *Phys. Rev.*, D58:074004, 1998.

[52] Francesca Borzumati and Christoph Greub. Two Higgs doublet model predictions for anti-B → X/s gamma in NLO QCD. (Addendum). *Phys. Rev.*, D59:057501, 1999.

[53] Ulrich Haisch. $\bar{B} \to X_s\gamma$: Standard Model and Beyond. 2008.

[54] Gerard 't Hooft and M. J. G. Veltman. Regularization and Renormalization of Gauge Fields. *Nucl. Phys.*, B44:189–213, 1972.

[55] S. Laporta. High-precision calculation of multi-loop Feynman integrals by difference equations. *Int. J. Mod. Phys.*, A15:5087–5159, 2000.

[56] K. G. Chetyrkin and F. V. Tkachov. Integration by Parts: The Algorithm to Calculate beta Functions in 4 Loops. *Nucl. Phys.*, B192:159–204, 1981.

[57] K. G. Chetyrkin, A. L. Kataev, and F. V. Tkachov. New Approach to Evaluation of Multiloop Feynman Integrals: The Gegenbauer Polynomial x Space Technique. *Nucl. Phys.*, B174:345–377, 1980.

[58] Vladimir A. Smirnov and O. L. Veretin. Analytical results for dimensionally regularized massless on-shell double boxes with arbitrary indices and numerators. *Nucl. Phys.*, B566:469–485, 2000.

[59] J. B. Tausk. Non-planar massless two-loop Feynman diagrams with four on-shell legs. *Phys. Lett.*, B469:225–234, 1999.

[60] T. Binoth and G. Heinrich. Numerical evaluation of multi-loop integrals by sector decomposition. *Nucl. Phys.*, B680:375–388, 2004.

[61] Vladimir A. Smirnov. Asymptotic expansions in limits of large momenta and masses. *Commun. Math. Phys.*, 134:109–137, 1990.

[62] Vladimir A. Smirnov. Asymptotic expansions in momenta and masses and calculation of Feynman diagrams. *Mod. Phys. Lett.*, A10:1485–1500, 1995.

[63] Michele Caffo, H. Czyz, S. Laporta, and E. Remiddi. The master differential equations for the 2-loop sunrise selfmass amplitudes. *Nuovo Cim.*, A111:365–389, 1998.

[64] Michele Caffo, H. Czyz, and E. Remiddi. Numerical evaluation of the general massive 2-loop sunrise self-mass master integrals from differential equations. *Nucl. Phys.*, B634:309–325, 2002.

[65] M. K. Gaillard and Benjamin W. Lee. Rare Decay Modes of the K-Mesons in Gauge Theories. *Phys. Rev.*, D10:897, 1974.

[66] Mikhail A. Shifman, A. I. Vainshtein, and Valentin I. Zakharov. Nonleptonic Decays of K Mesons and Hyperons. *Sov. Phys. JETP*, 45:670, 1977.

[67] Francesca Di Lodovico. A Review of the Magnitudes of the CKM Matrix Elements. *Int. J. Mod. Phys.*, A23:4945–4958, 2008.

[68] Konstantin G. Chetyrkin, Mikolaj Misiak, and Manfred Munz. Weak radiative B-meson decay beyond leading logarithms. *Phys. Lett.*, B400:206–219, 1997.

[69] Michael S. Chanowitz, M. Furman, and I. Hinchliffe. The Axial Current in Dimensional Regularization. *Nucl. Phys.*, B159:225, 1979.

[70] Paolo Gambino, Martin Gorbahn, and Ulrich Haisch. Anomalous Dimension Matrix for Radiative and Rare Semileptonic B Decays up to Three Loops. *Nucl. Phys.*, B673:238–262, 2003.

[71] Martin Gorbahn and Ulrich Haisch. Effective Hamiltonian for non-leptonic —Delta(F)— = 1 decays at NNLO in QCD. *Nucl. Phys.*, B713:291–332, 2005.

[72] Martin Gorbahn, Ulrich Haisch, and Mikolaj Misiak. Three-loop mixing of dipole operators. *Phys. Rev. Lett.*, 95:102004, 2005.

[73] Michal Czakon, Ulrich Haisch, and Mikolaj Misiak. Four-loop anomalous dimensions for radiative flavour- changing decays. *JHEP*, 03:008, 2007.

[74] Stefan Herrlich and Ulrich Nierste. Evanescent operators, scheme dependences and double insertions. *Nucl. Phys.*, B455:39–58, 1995.

[75] Pietro Antonio Grassi. Renormalization of non-semisimple gauge models with the background field method. *Nucl. Phys.*, B560:499–550, 1999.

[76] Christoph Bobeth, Mikolaj Misiak, and Jorg Urban. Photonic penguins at two loops and m(t)-dependence of BR(B → X(s) l+ l-). *Nucl. Phys.*, B574:291–330, 2000.

[77] C. S. Lim and T. Inami. Lepton flavor nonconservation and the mass generation mechanism for neutrinos. *Prog. Theor. Phys.*, 67:1569, 1982.

[78] K. Adel and York-Peng Yao. Exact alpha-s calculation of b → s + gamma b → s + g. *Phys. Rev.*, D49:4945–4948, 1994.

[79] Christoph Greub and Tobias Hurth. Two-loop matching of the dipole operators for b → s gamma and b → s g. *Phys. Rev.*, D56:2934–2949, 1997.

[80] Mikolaj Misiak and Matthias Steinhauser. Three-loop matching of the dipole operators for b → s gamma and b → s g. *Nucl. Phys.*, B683:277–305, 2004.

[81] Marco Ciuchini, E. Franco, G. Martinelli, L. Reina, and L. Silvestrini. Scheme independence of the effective Hamiltonian for b → s gamma and b → s g decays. *Phys. Lett.*, B316:127–136, 1993.

[82] Marco Ciuchini, E. Franco, L. Reina, and L. Silvestrini. Leading order QCD corrections to b → s gamma and b → s g decays in three regularization schemes. *Nucl. Phys.*, B421:41–64, 1994.

[83] Christian W. Bauer, Zoltan Ligeti, Michael Luke, Aneesh V. Manohar, and Michael Trott. Global analysis of inclusive B decays. *Phys. Rev.*, D70:094017, 2004.

[84] Paolo Gambino and Paolo Giordano. Normalizing inclusive rare B decays. *Phys. Lett.*, B669:69–73, 2008.

[85] Andrzej Czarnecki and William J. Marciano. Electroweak radiative corrections to b → s gamma. *Phys. Rev. Lett.*, 81:277–280, 1998.

[86] Paolo Gambino and Ulrich Haisch. Electroweak effects in radiative B decays. *JHEP*, 09:001, 2000.

[87] Paolo Gambino and Ulrich Haisch. Complete electroweak matching for radiative B decays. *JHEP*, 10:020, 2001.

[88] Andrzej J. Buras, Andrzej Czarnecki, Mikolaj Misiak, and Jorg Urban. Completing the NLO QCD calculation of anti-B → X/s gamma. *Nucl. Phys.*, B631:219–238, 2002.

[89] Paolo Gambino and Mikolaj Misiak. Quark mass effects in B -¿ Xs gamma. *Nucl. Phys.*, B611:338–366, 2001.

[90] Andre H. Hoang, Zoltan Ligeti, and Aneesh V. Manohar. B decays in the Upsilon expansion. *Phys. Rev.*, D59:074017, 1999.

[91] M. Misiak et al. The first estimate of B(anti-B $\to$ X/s gamma) at O(alpha(s)**2). *Phys. Rev. Lett.*, 98:022002, 2007.

[92] A. J. Buras, M. Misiak, M. Munz, and S. Pokorski. Theoretical uncertainties and phenomenological aspects of B $\to$ X(s) gamma decay. *Nucl. Phys.*, B424:374–398, 1994.

[93] Andrzej J. Buras and Mikolaj Misiak. Anti-B $\to$ X/s gamma after completion of the NLO QCD calculations. *Acta Phys. Polon.*, B33:2597–2612, 2002.

[94] Kirill Melnikov and Alexander Mitov. The photon energy spectrum in B $\to$ X/s + gamma in perturbative QCD through O(alpha(s)**2). *Phys. Lett.*, B620:69–79, 2005.

[95] Ian Richard Blokland, A. Czarnecki, M. Misiak, M. Slusarczyk, and F. Tkachov. The electromagnetic dipole operator effect on anti-B $\to$ X/s gamma at $\mathcal{O}(alpha(s)^2)$. *Phys. Rev.*, D72:033014, 2005.

[96] H. M. Asatrian et al. NNLL QCD contribution of the electromagnetic dipole operator to Gamma(anti-B $\to$ X/s gamma). *Nucl. Phys.*, B749:325–337, 2006.

[97] H. M. Asatrian, T. Ewerth, H. Gabrielyan, and C. Greub. Charm quark mass dependence of the electromagnetic dipole operator contribution to anti-B $\to$ X/s gamma at $\mathcal{O}(alpha(s)^2)$. *Phys. Lett.*, B647:173–178, 2007.

[98] Kay Bieri, Christoph Greub, and Matthias Steinhauser. Fermionic NNLL corrections to b $\to$ s gamma. *Phys. Rev.*, D67:114019, 2003.

[99] M. Beneke and Vladimir M. Braun. Naive nonAbelianization and resummation of fermion bubble chains. *Phys. Lett.*, B348:513–520, 1995.

[100] Stanley J. Brodsky, G. Peter Lepage, and Paul B. Mackenzie. On the Elimination of Scale Ambiguities in Perturbative Quantum Chromodynamics. *Phys. Rev.*, D28:228, 1983.

[101] Michael E. Luke, Martin J. Savage, and Mark B. Wise. Charm mass dependence of the $\mathcal{O}(alpha - s^2 n(f))$ correction to inclusive B $\to$ X(c) e anti-electron- neutrino decay. *Phys. Lett.*, B345:301–306, 1995.

[102] Andrzej Czarnecki and Kirill Melnikov. Two-loop QCD corrections to semileptonic b decays at an intermediate recoil. *Phys. Rev.*, D59:014036, 1999.

[103] Mikolaj Misiak and Matthias Steinhauser. NNLO QCD corrections to the $B \to X_s$ gamma matrix elements using interpolation in m_c. *Nucl. Phys.*, B764:62–82, 2007.

[104] Mikolaj Misiak. QCD Calculations of Radiative B Decays. 2008.

[105] H.M. Asatrian, T. Ewerth, A. Ferroglia, C. Greub, and G. Ossola. in preparation.

[106] Oliver Buchmuller and Henning Flacher. Fits to moment measurements from B → X/c l nu and B → X/s gamma decays using heavy quark expansions in the kinetic scheme. *Phys. Rev.*, D73:073008, 2006.

[107] Zoltan Ligeti, Iain W. Stewart, and Frank J. Tackmann. Treating the b quark distribution function with reliable uncertainties. *Phys. Rev.*, D78:114014, 2008.

[108] Ahmed Ali and C. Greub. Inclusive photon energy spectrum in rare B decays. *Z. Phys.*, C49:431–438, 1991.

[109] Thomas Becher and Matthias Neubert. Toward a NNLO calculation of the anti-B → X/s+ gamma decay rate with a cut on photon energy. II: Two-loop result for the jet function. *Phys. Lett.*, B637:251–259, 2006.

[110] Thomas Becher and Matthias Neubert. Toward a NNLO calculation of the anti-B → X/s gamma decay rate with a cut on photon energy. I: Two-loop result for the soft function. *Phys. Lett.*, B633:739–747, 2006.

[111] Thomas Becher and Matthias Neubert. Analysis of Br(B → X/s gamma) at NNLO with a cut on photon energy. *Phys. Rev. Lett.*, 98:022003, 2007.

[112] Adam F. Falk, Michael E. Luke, and Martin J. Savage. Nonperturbative contributions to the inclusive rare decays B → X(s) gamma and B → X(s) lepton+ lepton-. *Phys. Rev.*, D49:3367–3378, 1994.

[113] Ikaros I. Y. Bigi, B. Blok, Mikhail A. Shifman, N. G. Uraltsev, and Arkady I. Vainshtein. A QCD 'manifesto' on inclusive decays of beauty and charm. 1992.

[114] Matthias Neubert. Renormalization-group improved calculation of the B → X/s+ gamma branching ratio. *Eur. Phys. J.*, C40:165–186, 2005.

[115] Zoltan Ligeti, Lisa Randall, and Mark B. Wise. Comment on nonperturbative effects in anti-B → X/s gamma. *Phys. Lett.*, B402:178–182, 1997.

[116] G. Buchalla, G. Isidori, and S. J. Rey. Corrections of order $\Lambda(QCD)^2/m(c)^2$ to inclusive rare B decays. *Nucl. Phys.*, B511:594–610, 1998.

[117] Aaron K. Grant, A. G. Morgan, S. Nussinov, and R. D. Peccei. Comment on nonperturbative $\mathcal{O}(1/m(c)^2)$ corrections to Gamma(anti-B → X/s gamma). *Phys. Rev.*, D56:3151–3154, 1997.

[118] M. B. Voloshin. Large $\mathcal{O}(m(c)^{-2})$ nonperturbative correction to the inclusive rate of the decay B → X/s gamma. *Phys. Lett.*, B397:275–278, 1997.

[119] A. Khodjamirian, R. Ruckl, G. Stoll, and D. Wyler. QCD estimate of the long-distance effect in $B \to K^*$ gamma. *Phys. Lett.*, B402:167–177, 1997.

[120] Mikolaj Misiak. B -¿ Xs gamma - Current Status. 2009.

[121] Seung J. Lee, Matthias Neubert, and Gil Paz. Enhanced non-local power corrections to the B → X/s+ gamma decay rate. *Phys. Rev.*, D75:114005, 2007.

[122] R. Boughezal, M. Czakon, and T. Schutzmeier. NNLO fermionic corrections to the charm quark mass dependent matrix elements in $B \to X_s\gamma$. *JHEP*, 09:072, 2007.

[123] M. Czakon. Diagen diagram generator, unpublished.

[124] M. Czakon. Automatized analytic continuation of Mellin-Barnes integrals. *Comput. Phys. Commun.*, 175:559–571, 2006.

[125] S. Moch and P. Uwer. XSummer: Transcendental functions and symbolic summation in Form. *Comput. Phys. Commun.*, 174:759–770, 2006.

[126] K. G. Chetyrkin, Johann H. Kuhn, and M. Steinhauser. RunDec: A Mathematica package for running and decoupling of the strong coupling and quark masses. *Comput. Phys. Commun.*, 133:43–65, 2000.

[127] R. E. Cutkosky. Singularities and discontinuities of Feynman amplitudes. *J. Math. Phys.*, 1:429–433, 1960.

[128] M. Czakon. Idsolver, unpublished.

[129] G. Chachamis and M. Czakon. Mbrepresentation, unpublished.

[130] K. G. Chetyrkin, M. Faisst, Christian Sturm, and M. Tentyukov. e-finite basis of master integrals for the integration-by- parts method. *Nucl. Phys.*, B742:208–229, 2006.

[131] M. Czakon. Tops from Light Quarks: Full Mass Dependence at Two-Loops in QCD. *Phys. Lett.*, B664:307–314, 2008.

[132] R. Boughezal, M. Czakon, and T. Schutzmeier. Charm and bottom quark masses from perturbative QCD. *Phys. Rev.*, D74:074006, 2006.

[133] Johann H. Kuhn, Matthias Steinhauser, and Christian Sturm. Heavy quark masses from sum rules in four-loop approximation. *Nucl. Phys.*, B778:192–215, 2007.

[134] R. Boughezal and M. Czakon. Single scale tadpoles and $\mathcal{O}(G(F)m(t)^2 alpha(s)^3)$ corrections to the rho parameter. *Nucl. Phys.*, B755:221–238, 2006.

[135] K. G. Chetyrkin, M. Faisst, Johann H. Kuhn, P. Maierhofer, and Christian Sturm. Four-loop QCD corrections to the rho parameter. *Phys. Rev. Lett.*, 97:102003, 2006.

[136] Johann H. Kuhn, Matthias Steinhauser, and Thomas Teubner. Determination of the strong coupling constant from the CLEO measurement of the total hadronic cross section in e^+e^- annihilation below 10.56 GeV. *Phys. Rev.*, D76:074003, 2007.

[137] F. Jegerlehner. Precision measurements of sigma(hadronic) for alpha(eff)(E) at ILC energies and (g-2)(mu). *Nucl. Phys. Proc. Suppl.*, 162:22–32, 2006.

[138] K. G. Chetyrkin, Johann H. Kuhn, and M. Steinhauser. Three-loop polarization function and $\mathcal{O}(alpha(s)^2)$ corrections to the production of heavy quarks. *Nucl. Phys.*, B482:213–240, 1996.

[139] K. G. Chetyrkin, Johann H. Kuhn, and M. Steinhauser. Heavy quark current correlators to $\mathcal{O}(alpha(s)^2)$. *Nucl. Phys.*, B505:40–64, 1997.

[140] K. G. Chetyrkin, R. Harlander, and M. Steinhauser. Singlet polarization functions at $\mathcal{O}(alpha(s)^2)$. *Phys. Rev.*, D58:014012, 1998.

[141] K. G. Chetyrkin, Johann H. Kuhn, and Christian Sturm. Four-loop moments of the heavy quark vacuum polarization function in perturbative QCD. *Eur. Phys. J.*, C48:107–110, 2006.

[142] K. G. Chetyrkin, A. L. Kataev, and F. V. Tkachov. Higher Order Corrections to Sigma-t (e+ e- $\rightarrow$ Hadrons) in Quantum Chromodynamics. *Phys. Lett.*, B85:277, 1979.

[143] William Celmaster and Richard J. Gonsalves. Fourth Order QCD Contributions to the e+ e- Annihilation Cross-Section. *Phys. Rev.*, D21:3112, 1980.

[144] Michael Dine and J. R. Sapirstein. Higher Order QCD Corrections in e+ e- Annihilation. *Phys. Rev. Lett.*, 43:668, 1979.

[145] S. G. Gorishnii, A. L. Kataev, and S. A. Larin. The O (alpha-s**3) corrections to sigma-tot (e+ e- $\rightarrow$ hadrons) and Gamma (tau- $\rightarrow$ tau-neutrino + hadrons) in QCD. *Phys. Lett.*, B259:144–150, 1991.

[146] Levan R. Surguladze and Mark A. Samuel. Total hadronic cross-section in e+ e- annihilation at the four loop level of perturbative QCD. *Phys. Rev. Lett.*, 66:560–563, 1991.

[147] K. G. Chetyrkin. Corrections of order $\alpha(s)^3$ to R(had) in pQCD with light gluinos. *Phys. Lett.*, B391:402–412, 1997.

[148] K. G. Chetyrkin and Johann H. Kuhn. Quadratic mass corrections of order $\mathcal{O}(alpha(s)^3 m(q)^2)$ to the decay rate of Z and W bosons. *Phys. Lett.*, B406:102–109, 1997.

[149] K. G. Chetyrkin, R. V. Harlander, and Johann H. Kuhn. Quartic mass corrections to R(had) at $\mathcal{O}(alpha(s)^3)$. *Nucl. Phys.*, B586:56–72, 2000.

[150] P. A. Baikov, K. G. Chetyrkin, and Johann H. Kuhn. The cross section of e+ e- annihilation into hadrons of order $alpha(s)^4 n(f)^2$ in perturbative QCD. *Phys. Rev. Lett.*, 88:012001, 2002.

[151] P. A. Baikov, K. G. Chetyrkin, and Johann H. Kuhn. Five-loop vacuum polarization in pQCD: $O_(m(q)^2 alpha(s)^4 n(f)^2)$ contribution. *Phys. Lett.*, B559:245–251, 2003.

[152] R. Boughezal, M. Czakon, and T. Schutzmeier. Four-loop tadpoles: Applications in QCD. *Nucl. Phys. Proc. Suppl.*, 160:160–164, 2006.

[153] A. Maier, P. Maierhofer, and P. Marquard. Higher Moments of Heavy Quark Correlators in the Low Energy Limit at $\mathcal{O}(alpha_s^2)$. *Nucl. Phys.*, B797:218–242, 2008.

[154] Y. Schroder and M. Steinhauser. Four-loop decoupling relations for the strong coupling. *JHEP*, 01:051, 2006.

[155] K. G. Chetyrkin, J. H. Kuhn, P. Mastrolia, and C. Sturm. Heavy-quark vacuum polarization: First two moments of the $O(\alpha_s^3 n_f^2)$ contribution. *Eur. Phys. J.*, C40:361–366, 2005.

[156] M. Czakon. `quadprec`, unpublished.

Dank

An dieser Stelle möchte ich allen danken, die mich in den letzten Jahren unterstützt und so zum Gelingen dieser Arbeit beigetragen haben. Insbesondere gilt mein Dank:

- Prof. Michal Czakon für die Betreuung, die Bereitschaft, Fragen und Probleme jederzeit zu diskutieren, interessante Gespräche auch über die Physik hinaus und insbesondere die mir entgegengebrachte Förderung.
- Prof. Rückl, zum Einen für die Möglichkeit dieses herausforderende Thema an seinem Lehrstuhl zu bearbeiten, zum Anderen für die Unterstützung in meiner Zeit als Doktorand.
- allen Diplomanden, Doktoranden und Postdocs am Lehrstuhl TP2, die mir neue Einblicke in die Physik eröffnet und zudem zu einer angenehmen Atmosphäre im Arbeitskreis und darüber hinaus beigetragen haben, insbesondere: Grigorios Chachamis, Lisa Edelhäuser, Dolores Eiras, Alexander Knochel und Christian Speckner
- Brigitte Wehner für die große Hilfe bei organisatorischen und Verwaltungsangelegenheiten und die entscheidende Rettung in letzter Minute
- meinen Eltern für die uneingeschränkte Unterstützung in allen Lebenslagen
- und insbesondere Karoline, für zahlreiche Korrekturen, Vorschläge und Verbesserungen, aber vor Allem für ihren großen Rückhalt in der Endphase dieser Arbeit.